Paleostress analysis using deformation microstructures of the Late Cretaceous granitoids in Chubu region, Southwest Japan

西南日本中部地方に分布する後期白亜紀花崗岩類に発達する変形微細構造を利用した古応力解析

February, 2017

Waseda University
Graduate School of Creative Science and Engineering
Department of Earth Sciences, Resources and Environmental Engineering,
Research on Structural Petrology

Takuto KANAI
金井 拓人

Contents

Abstract

In this study, paleostress and deformation conditions of the Late Cretaceous granitoids in Chubu region were estimated using deformation microstructures. Paleostress analysis of Cretaceous granitoids is important to discuss the geological structure.

Chapters 1 and 2 are introduction and geological background, respectively.

In Chapter 3, paleostress orientation was estimated using healed microcracks (HC) developed in quartz grains in granitoids. Since HC preferentially forms perpendicular to the minimum principal stress (σ_3) axis whereas difficult perpendicular to the maximum principal stress (σ_1) axis, paleostress directions can be estimated on the basis of the orientation distribution of HCs. In previous studies, only the orientation of the σ_3 axis could be estimated. Recently, a new method that represents orientation distribution of crack poles by probability density function had been proposed. This method allows to quantify the full paleostress (σ_1, σ_3, and intermediate principal stress: σ_2) orientations and stress ratio. Moreover, it allows to decompose overprinted crack distribution into multiple probability density distributions. Therefore, even if microcracks have recorded different paleostress fields during several tectonic stages, the new methods can separate each paleostress stage. In this study, adjustment parameters in order to apply the new method for HC analysis is proposed, which allow to and developed a method to estimate the orientation distribution of HCs in quartz grains more accurately than in previous studies. Thereafter, the HC formation conditions and paleostress of granitoids were determined for the samples collected from 1) the transect parallel to the MTL from Shinshiro Tonalite and Tenryukyo Granodiorite; and 2) the transect normal to the MTL from Shinshiro Tonalite, via. Busetsu Granite, Mitsuhashi Granodiorite, Inagawa Granodiorite to Toki Granite. Based on the microthermometric analysis of fluid inclusions constituting the HC, the formation temperatures of HCs were estimated to be 300–450°C on average. Therefore, the formation age of the HCs approximates the cooling age, 75–64 Ma, of analyzed granitoids. As a result of the paleostress analysis, the σ_3 axis shows orthogonal to the MTL strike in vicinity of the MTL, while it tends to rotate counterclockwise away from the MTL and roughly parallel to the MTL strike in the Toki Granite at about 60 km away from the MTL. The σ_1 and σ_2 orientations show no correlation with the distance from the MTL, however, regardless of the difference of rock bodies, they yield similar orientations within the domain of about 10 km diameter.

In Chapter 4, paleostress orientation and the stress conditions of the ductile-to-brittle regime have been assessed along the Asuke Shear Zone (ASZ) transected in the Inagawa Granodiorite. Along the ASZ, pseudotachylyte and mylonitized pseudotachylyte are locally

developed together with cataclasite. Mylonitized pseudotachylytes in the ASZ was considered the products of deformation in the ductile-to-brittle transition regime (300–400°C). Since the deformation temperature overlaps, the ASZ can be considered to be activated at the same time of the formation of the HC described above. The paleostress orientation can be estimated separately by two methods different from that of the HCs. One is from the fault kinematics of the Asuke shear zone, and the other is from a distribution of the glide direction on the *e*-twin plane of the twinned calcite in amygdules formed in the pseudotachylyte. Moreover, deformation temperature and differential stress were determined using recrystallized quartz grains in the mylonitized pseudotachylyte. The distribution of the glide direction on the *e*-twin plane of the twinned calcite suggest that the trend and plunge of σ_1 and of σ_3 axes are 228°/55° and 320°/1°, respectively. The twinning ratio and *e*-twin morphology indicate differential stresses of 40–80 MPa at 150–200°C. The simultaneous operation of dislocation creep and grain-size-sensitive creep, as indicated by the coexistence of the Z-maximum and relatively random *c*-axis lattice preferred orientations as well as the sizes of dynamically recrystallized quartz grains (6.40–7.79 μm) in the mylonitized pseudotachylyte, suggest differential stresses of 110–130 MPa at ~300°C. Based on kinematic indicators in the fault rocks, the stress conditions estimated from calcite twins, and the cooling history of the granitic protolith, the ASZ is inferred to have been activated under a stress state that caused sinistral normal movements before and after pseudotachylyte formation at 70–50 Ma.

In Chapter 5, the regional paleostress field in the Cretaceous granitoids during their cooling stage was discussed based on the results of above paleostress analyses. The timing of HC formation (75–65 Ma) and activity of the ASZ (70–50 Ma) are nearly overlapped, and the orientation of σ_3 axes estimated from HCs around the ASZ the deformation structures in the ASZ indicate similar orientation. Since the orientation of σ_3 axis estimated from the shear zone and HC are harmonious, it is considered that the paleostress recorded in HC reflects the regional stress field rather than the local stress as the sample scale. Therefore, it is considered that the orientation of the σ_3 axis estimated from HC has recorded the regional stress field at 75–65 Ma. The activity of the MTL at the Ichinokawa phase (63–58 Ma) has been considered to be extensional fault movement which caused juxtaposition of the Ryoke complex against the Sanbagawa metamorphic rocks. The dominant σ_3 axis (NW–SE) normal to the MTL in the vicinity of the MTL is considered to be related to the extensional faulting of the MTL in Ichinokawa Phase. On the other hand, the dominant σ_3 axis (NE–SW) parallel to the MTL at a distance from the MTL suggests the influence of plate convergence direction (NW) at about 75–64 Ma rather than the influence of MTL-normal extension. The rotation of the orientation of the σ_3 axis with respect to the distance from the MTL can be explained by relative strength

of the effects of tensile stress field that had developed around the MTL and of overall plate convergence in Chub region. This study clarified the paleostress from the Cretaceous granitoids that causes the normal fault movement of the MTL at the Ichinokawa phase.

Acknowledgements

I am deeply grateful to Prof. Hideo Takagi of Waseda University for his guidance, support and encouragement during this study. I would like to express my gratitude to Prof. Atsushi Yamaji of Kyoto University for his critical advice and undertaking the part of the paleostress analysis of HCs. I would like to express my gratitude to Dr. Tohru Ohta of Waseda University for his constructive comments. I wish to thank Dr. Hiroyoshi Arai of Waseda University Honjo High School for his advice on research direction and statistical processing of the directional data. I wish to thank Emer. Prof. Mamoru Enjoji of Waseda University for his technical advice on microthermometric analysis of fluid inclusions. I wish to thank Dr. Katsushi Sato of Kyoto University for his advice about an observation bias of the directional data. I wish to thank Dr. Ichiro Iwasaki, Mr. Shoichi Rikita, Ms. Rie Tajiri, Dr. Hideki Mukoyoshi and Mr. Masahiko Hayashi of Waseda University for their advice on the method of thin-section preparation. I wish to thank Mr. Kojiro Moriyama and Mr. Shunsuke Watanuki for his advice and discussion on the SEM-EBSD analysis. I also thank Mr. Shinsuke Aizawa and Hideaki Sakamaki for providing some of the analyzed samples and the original outcrop maps. Thanks to the member of Takagi Laboratory for their discussion and helpful support. Finally, I greatly wish to thank my family for their assistance and encouragement.

Chapter 1: Introduction

The Cretaceous granitoids are exposed throughout SW Japan from Kyushu to Kanto Region, extending for nearly 1000 km in length and width of 30–50 km. These granitoids were formed in the eastern part of the East Asia continent in the Middle–Late Cretaceous (e.g., Okudaira et al., 2009). In addition, several left-lateral strike-slip faults such as Median Tectonic Line (MTL) are considered to be active during this period (e.g. Yamakita and Otoh, 2000). Therefore, the record of igneous activity (Uyeda and Miyashiro, 1974; Kinoshita, 1995; Suzuki and Adachi, 1998; Okudaira et al., 2001; Sakashima et al., 2003) and deformation (Takagi, 1984, 1985, 1986; Michibayashi et al., 1997; Jefferies et al., 2006; Adachi and Wallis, 2008) of the Cretaceous granitoids are important to discuss the tectonics of the plate convergence zone. The Cretaceous granitoids are widely distributed in Chubu region, and many studies such as radiogenic dating (e.g. Suzuki and Adachi, 1998), correlation of chemical compositions (Ishihara and Chappell, 2007), deformation analysis of mylonite around the MTL (Takagi, 1984, 1985), structural analysis of macroscopic fracture (Ishise et al., 2006) have been conducted. Although the Chubu region rotated due to opening of Sea of Japan (Otofuji et al., 1985, 1999; Hoshi et al., 2015) and following collision of the Izu-Ogasawara arc (Itoh, 1988; Takahashi and Saito, 1997; Otofuji et al., 1999) against the Honshu arc on the basis of the paleomagnetic studies, it is possible to analyze the Cretaceous paleostress by using the strike of the MTL as a marker of rotation (Shimada et al., 1998; Aizawa and Takagi, 2008). Paleostress analysis has been carried out using microcracks developed in the Cretaceous granitoids in Chubu region (Aizawa and Takagi, 2008; Takagi et al., 2008, 2012). In this study, the new analysical method (Yamaji et al., 2010; Yamaji and Sato, 2011) was used to estimate the paleostress analysis of healed microcracks (HCs) from samples collected over a wide area in Chubu region. Furthermore, the deformation conditions and paleostress were estimated along the Asuke Shear Zone (ASZ) extended in Toyota city, Aichi Prefecture. These paleostresses from different methods were compared, and the paleostress field during the cooling of the Late Cretaceous granitoids in the plate convergence continental margin were discussed.

Chapter 2: Geotectonic framework in Chubu region

2.1. Basement geology of the Japanese Island

The basement rocks of the crustal surface layer of the Japanese Island are composed of past accretionary complex and their high-pressure metamorphic terrains, and volcanic arc granites that intruded into them (Fig. 2.1; Isozaki et al., 2010; Taira et al., 2016). The Japanese Island can be divided into NE Japan and SW Japan arcs, which are separated by the *Fossa Magna*. The SW Japan is divided into the Inner Zone on the north side and the Outer Zone on the south side by the MTL. The Ryoke Belt, the southernmost belt of the Inner Zone

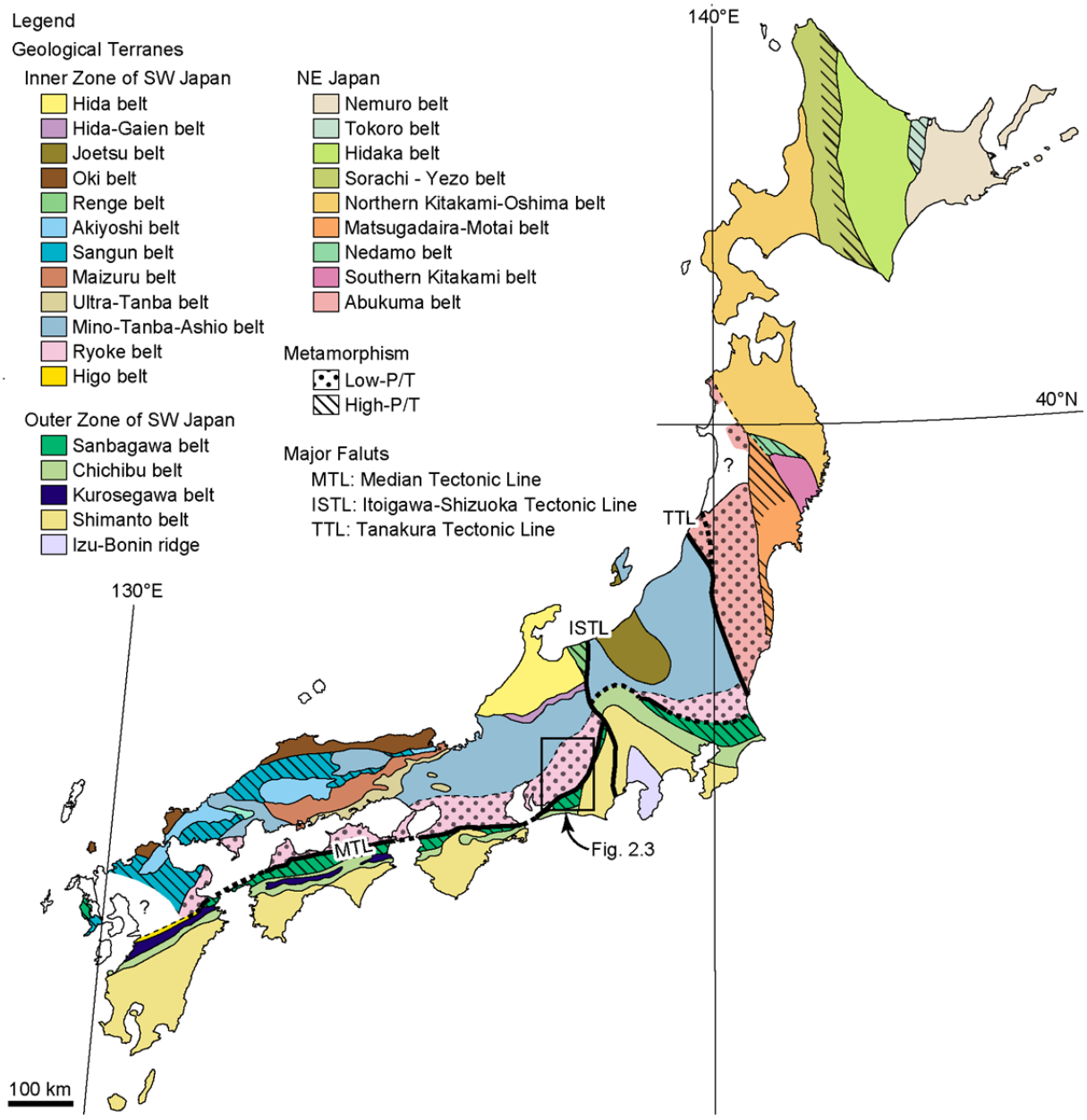

Fig. 2.1. Major tectonic units of Japan, modified after Isozaki et al. (2010) and Taira et al. (2016).

and the Sanbagawa Belt, the northernmost belt of the Outer Zone contact longitudinally by the MTL. In the Inner Zone, granitods intruded during the Cretaceous to the Paleogene are widely distributed (Kinoshita, 1995; Isozaki et al., 2010).

2.2. Geological settings and petrography of Ryoke–Sanyo granitoids

2.2.1 Cretaceous–Early Paleogene granitic province

The Cretaceous–Early Paleogene granitic province in the SW Japan is the largest in the Japanese Islands (Fig. 2.2). It extends from central Japan to Kyushu Island on the northern side of the MTL, and the eastern margin of China, the Korean Peninsula, the Sikhote-Alin and Okhotsk–Chukotka region of Russia (Ishihara, 1977; Kinoshita, 1995; Wakita, 2013;

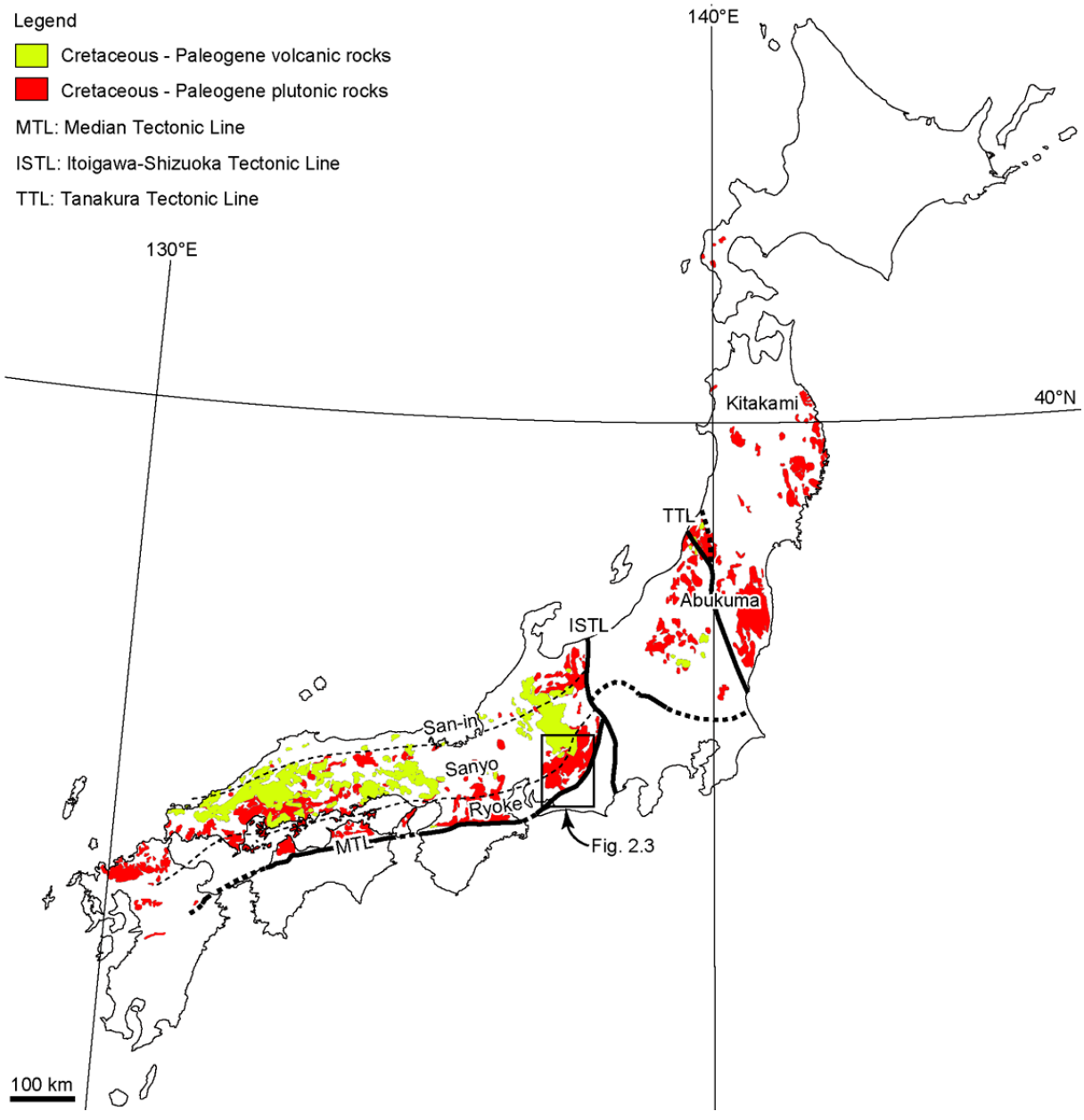

Fig. 2.2. Distribution of Late Cretaceous to Paleogene plutonic rocks and volcanic rocks in Japan, modified after Kinoshita (1995) and Wakita (2013).

Nakajima et al., 2016; Fig. 2.2).The province is divided into three arc-parallel zones which, from forearc to back-arc position, are called Ryoke, Sanyo and San-in belts (Nakajima, 1996; Okudaira and Suda, 2011). The Sanyo and San-in belts are composed of volcano–plutonic complex, while the Ryoke belt is a plutono–metamorphic belt accompanying migmatites (Nakajima et al., 2016). Granitic rocks in both Ryoke and Sanyo belts are entirely Cretaceous (115–65 Ma), while those in the San-in belt are of Middle Cretaceous–Early Paleogene age (110–55 Ma) (Suzuki et al., 1994b, 1996; Suzuki and Adachi, 1998; Kawakami and Suzuki, 2011; Miyake et al., 2016).

In Chubu region of the SW Japan, Sanyo and Ryoke granitoids are widely distributed (Fig. 2.3; Table 2.1). Ryoke Research Group (1972) classified the granitoids intrusion into nine stages based on intrusion relationship at outcrop. Harayama et al. (1985) classified the magmatic activities in the Cretaceous to Paleogene in Chubu region into five stages, in which the activities of Ryoke–Sanyo granitoids were classified as stage I and II. The stage I (120–

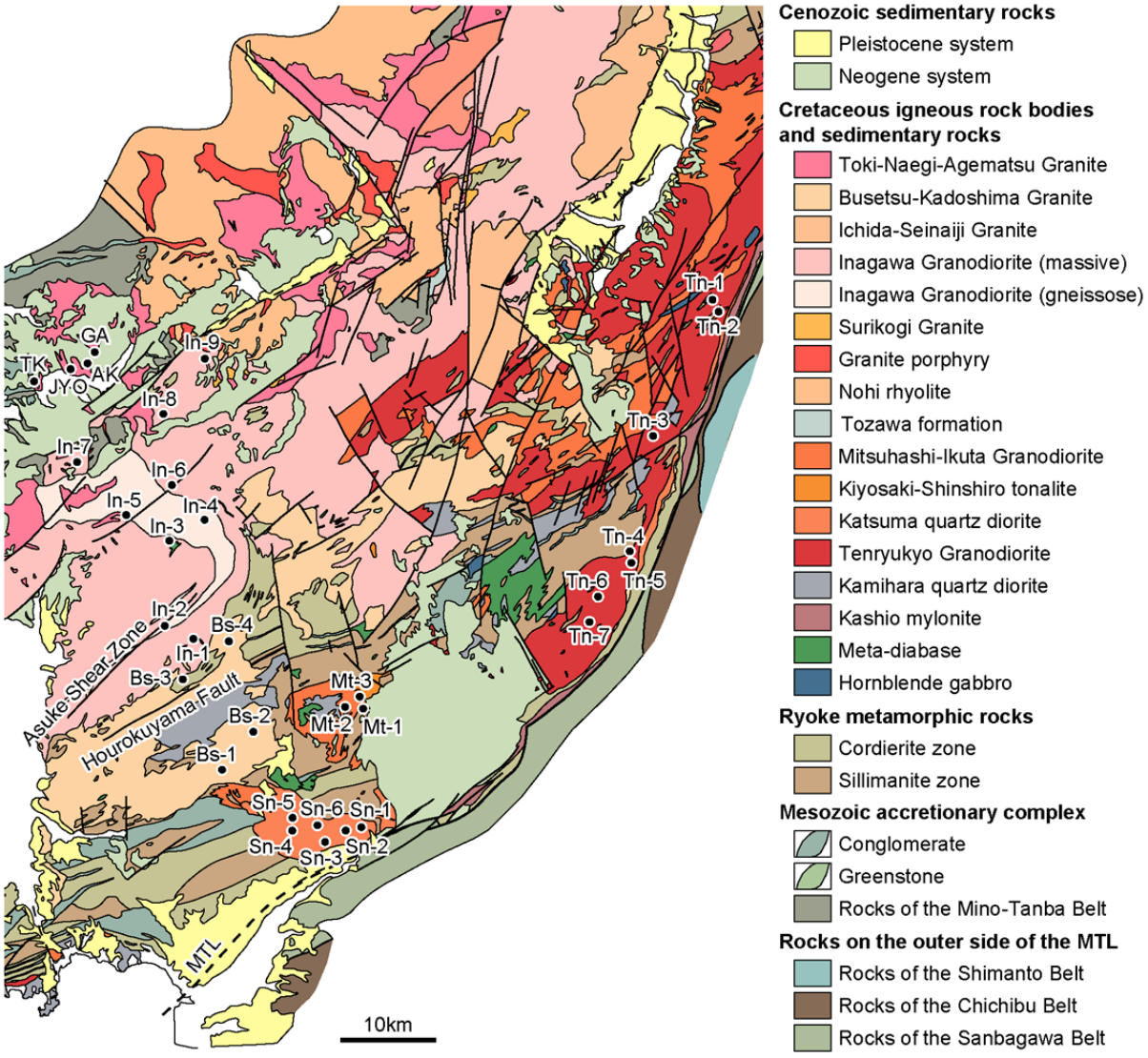

Fig. 2.3. Geological map of the Ryoke–Sanyo granitoids in Chubu region and sampling locations, partly modified after Yamada et al. (1974).

90 Ma) is the activity of plutonic rocks that caused Ryoke metamorphism (Harayama et al., 1985). These granitoidss are developed as the sheet-like bodies that having a gneissose structure in harmony with Ryoke metamorphic rocks (Harayama et al., 1985; Okudaira and Suda, 2011). The stage II (90–65 Ma) is the activity of the plutonic rocks (Harayama et al., 1985). These plutonic rocks and Sanyo granitoids were intruded as relatively small stock-like bodies cross-cutting the general structure of the weakly metamorphosed host rocks (Okudaira and Suda, 2011). Ryoke granitoids intruded in stages I and II are called Ryoke older and younger rocks, respectively. Monazite CHIME age of Ryoke older and younger granitoids have been reported 95–90 Ma and 90–70 Ma, respectively as an intrusive age of them (Suzuki et al., 1994a, 1994b; Morishita and Suzuki, 1995; Suzuki et al., 1995; Nakai and Suzuki, 1996; Suzuki and Adachi, 1998). On the other hand, biotite K–Ar ages agree with the values of 75–65 Ma for both Ryoke older and younger granite (Shibata et al., 1979; Shibata and Takagi, 1988; Uchiumi et al., 1990; Yamada et al., 1992; Yuhara, 2011; Yuguchi et al., 2011; Yamasaki, 2013).

Tenryukyo Granodiorite, Shinshiro Tonalite, Mitsuhashi Granodiorite, Inagawa Granodiorite, Busetsu Granite and Toki Granite are used for paleostress analysis. Inagawa Granodiorite has a wide range of distribution and several studies on the classification of rock facies have been proposed (Nakai, 1976; Yamasaki and Ozaki, 2012; Miyake et al., 2016).

Table 2.1. Intrusion stages, classification and radiometric ages of Ryoke–Sanyo granitioids.

Granitoids	Intrusion stage (R.R.G.*, 1974)	Intrusion stage (Harayama, 1985)	Classification	Monazite CHIME age	Biotite K-Ar age
Kamihara Tonalite	Stage-1	Stage-I	older Ryoke	94.9 - 94.5 (1)	71.0 - 70.4 (7)
Hiji Tonalite	Stage-1	Stage-I	older Ryoke	-	65.2 (8)
Tenryukyo Granodiorite	Stage-2	Stage-I	older Ryoke	92.2 - 89.7 (1,2)	64.4 - 63.9 (9)
Kiyosaki Granite	Stage-3	Stage-II	younger Ryoke	82.6 - 81.9 (2)	-
Katsuma quartz diorite	Stage-3	Stage-II	younger Ryoke	-	62.8 (8)
Shinshiro Tonalite	Stage-3	Stage-II	younger Ryoke	86.0 - 85.2 (3)	68.0 (10)
Mitsuhashi Granite	Stage-4	Stage-II	younger Ryoke	84.1 - 83.8 (4,5)	71.4 - 70.7 (7)
Ikuta Granite	Stage-4	Stage-II	younger Ryoke	-	-
Inagawa Granodiorite	Stage-5	Stage-II	younger Ryoke	82.6 - 81.9 (2)	70.7 - 66.4 (7)
Ichida Granite	Stage-6	Stage-II	younger Ryoke	79.4 (6)	-
Busetsu Granite	Stage-7	Stage-II	younger Ryoke	78.9 - 75.0 (5)	71.4 - 70.8 (7)
Otagiri Granite	Stage-7	Stage-II	younger Ryoke	77.4 - 76.3 (6)	-
Takato Granite	Stage-8	Stage-II	younger Ryoke	-	65 (11)
Kisokoma Granite	Stage-8	Stage-II	younger Ryoke	-	-
Toki Granite	Stage-9	Stage-II	Sanyo	68.3 (2)	78.5 - 59.7 (12)
Naegi Granite	Stage-9	Stage-II	Sanyo	67.2 (5)	66.1 - 64.3 (13)
Agematsu Granite	Stage-9	Stage-II	Sanyo	-	66.1 - 64.6 (13)

*: Ryoke Research Group. References cited are: 1 (Nakai and Suzuki, 1996), 2 (Suzuki and Adachi, 1998), 3 (Morishita and Suzuki, 1995), 4 (Suzuki et al., 1994a), 5 (Suzuki et al., 1994b), 6 (Suzuki et al., 1995), 7 (Yamasaki, 2013), 8 (Shibata and Takagi, 1988), 9 (Shibata et al., 1979), 10 (Uchiumi et al., 1980), 11 (Yuhara, 2011), 12 (Yuguchi et al., 2011), 13 (Yamada et al., 1992).

In this study, the rock facies of the Inagawa Granodiorite were divided into massive facies and gneissose facies, following Miyake et al. (2016). Emplacement and cooling ages of each Ryoke–Sanyo granitoids determined by several methods of radiogenic dating are shown in Fig. 2.4.

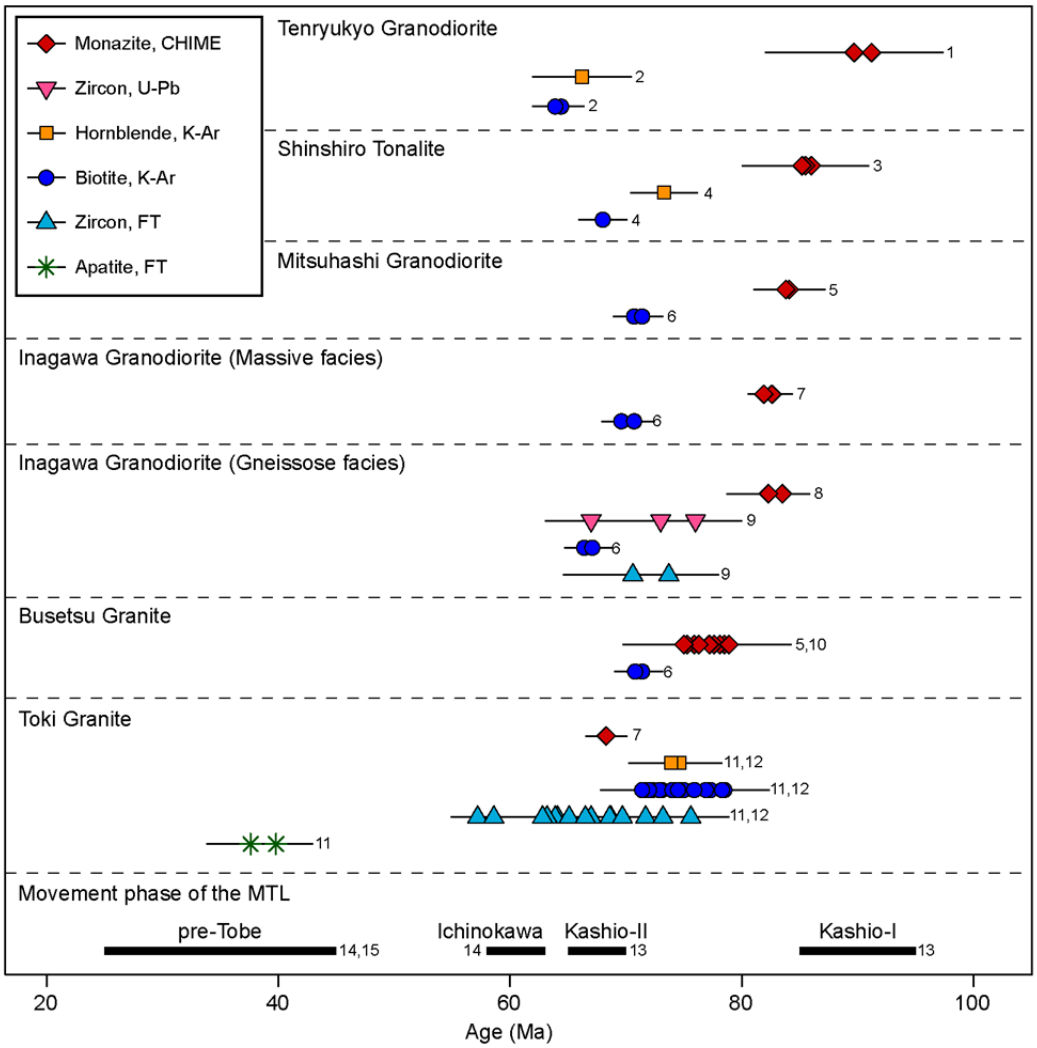

Fig. 2.4. Radiometric ages with 1σ error bars of the Ryoke–Sanyo granitoids and age of major activity phases of the MTL. References cited are: 1 (Nakai and Suzuki, 1996), 2 (Shibata et al., 1979), 3 (Morishita and Suzuki, 1995), 4 (Uchiumi et al., 1990), 5 (Suzuki et al., 1994), 6 (Yamasaki, 2013), 7 (Suzuki and Adachi, 1998), 8 (Miyake et al., 2016), 9 (Murakami et al., 2006), 10 (Nakai and Suzuki, 2003), 11 (Yamasaki and Umeda, 2012), 12 (Yuguchi et al., 2011), 13 (Takagi, 1997), 14 (Takagi and Shibata, 1992), 15 (Takagi et al., 1992).

2.2.2 Petrography of sample

(1) Tenryukyo Granodiorite (Fig. 2.5a): Medium–coarse-grained biotite hornblende Granodiorite which has gneissose texture defined by the preferred orientation of mafic minerals. It is mainly composed of quartz, plagioclase, biotite, hornblende, and K-feldspar, with accessories of apatite, zircon and opaque minerals. Quartz (0.2–4.6 mm long) occurs as anhedral grains and shows undulose extinction. Quartz grain boundaries are often sutured. Plagioclase (0.2–10.9 mm long) occurs as subhedral–euhedral grains with weak zoning.

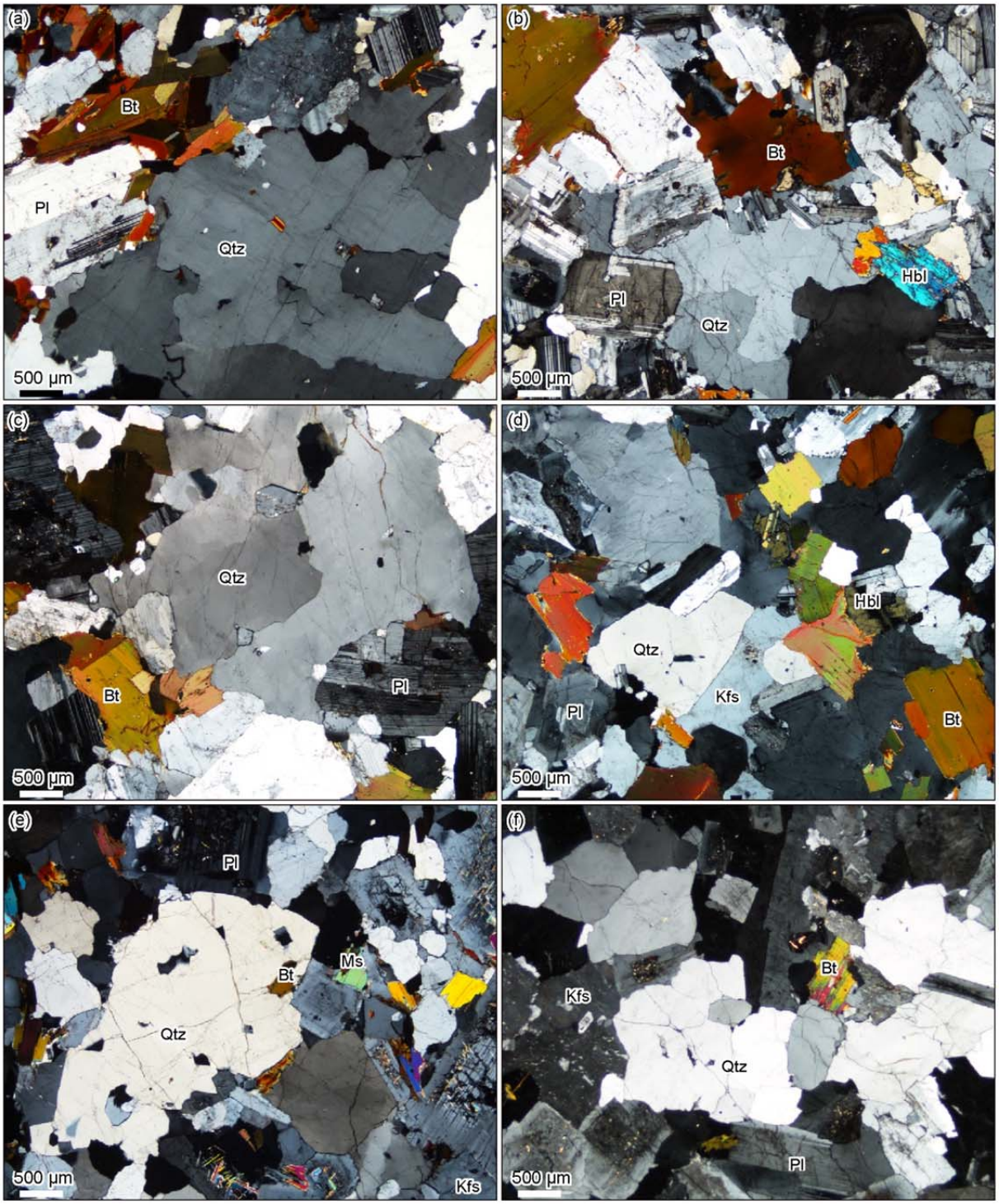

Fig. 2.5. Photomicrographs of the Late Cretaceous granitoids (XPL; crossed polarizers). (a) Tenryukyo granodiorite (sample Tn-6). (b) Shinshiro tonalite (sample Sn-3). (c) Mitsuhashi granodiorite (sample Mt-1). (d) Inagawa granodiorite (sample In-2). (e) Busetsu Granite (sample Bs-2). (f) Toki Granite (sample AK).

Biotite (0.2–2.2 mm long) occurs as subhedral grains and some of them form glomeroporphyritic texture. Hornblende (0.4–5.9 mm long) occurs as subhedral–euhedral grains. K-feldspar occurs as anhedral grains.

(2) Shinshiro Tonalite (Fig. 2.5b): Medium-grained biotite hornblende tonalite with equigranular texture and rarely porphyritic texture. It is mainly composed of plagioclase,

quartz, biotite, hornblende and rarely K-feldspar with accessories of apatite, opaque minerals, zircon and titanite. Plagioclase (0.3–3.5 mm long) occurs as subhedral–euhedral grains. Quartz (0.2–3.3 mm long) occurs as anhedral grains and shows undulose extinction. Biotite (0.3–5.6 mm long) occurs as subhedral grains and some of them show glomeroporphyritic texture. Hornblende (0.4–5.9 mm long) occurs as subhedral–euhedral shape. Hornblende phenocrysts as large as 1.2 cm in length were observed. K-feldspar occurs as anhedral grains.

(3) Mitsuhashi Granodiorite (Fig. 2.5c): Medium-grained biotite hornblende granodiorite with weak gneissose texture defined by the preferred orientation of biotite and plagioclase. It is mainly composed of plagioclase, quartz, biotite, hornblende and K-feldspar with accessories of apatite, zircon, titanite and opaque minerals. Plagioclase (0.2–6.4 mm long) occurs as subhedral–euhedral grains with weak zoning. Quartz (0.2–6.0 mm long) occurs as anhedral grains and shows undulose extinction. Biotite (0.2–4.0 mm long) occurs as subhedral grains and some of them show glomeroporphyritic texture. Hornblende (0.4–0.7 mm long) occurs as subhedral–euhedral grains. K-feldspar occurs as anhedral grains.

(4) Inagawa Granodiorite (gneissose facies; Fig. 2.5d): Medium-grained porphyritic biotite hornblende granodiorite. Samples In-1, In-2 and In-4 correspond to this facies. It has gneissose texture defined by the preferred orientation of mafic minerals. It is mainly composed of plagioclase, quartz, biotite, K-feldspar and hornblende, with accessories of apatite, zircon, titanite and opaque minerals. Plagioclase (0.2–5.1 mm long) occurs as subhedral–euhedral shape with weak zoning. Quartz (0.2–4.5 mm long) occurs as anhedral grains and shows undulose extinction. Biotite (0.2–2.4 mm long) occurs as subhedral grains and some of them show glomeroporphyritic texture. K-feldspar occurs as anhedral grains. Hornblende (0.7–6.7 mm long) occurs as subhedral–euhedral grains.

(5) Inagawa Granodiorite (massive facies): Coarse-grained biotite hornblende granodiorite. It is mainly composed of plagioclase, quartz, K-feldspar, biotite and hornblende, with accessories of apatite, zircon, titanite and opaque minerals. Plagioclase (0.4–10.2 mm long) occurs as subhedral–euhedral grains with weak zoning. Quartz (0.3–4.9 mm long) occurs as anhedral grains and shows undulose extinction. K-feldspar occurs as anhedral grains. Biotite (0.5–3.4 mm long) occurs as subhedral grains. Hornblende (0.3–3.8 mm long) occurs as subhedral–euhedral grains.

(6) Busetsu Granite (Fig. 2.5e): Fine–coarse-grained biotite muscovite granite. It is mainly composed of quartz, plagioclase, K-feldspar, biotite and muscovite, with accessories of apatite, garnet, zircon, and opaque minerals. These mineral composition and high Al contents (Ishihara and Chappell, 2007) suggest that the Busetsu Granite belongs to S-type granitoid. Plagioclase (0.2–2.4 mm long) occurs as subhedral–euhedral grains with weak zoning. Quartz

(0.2–3.0 mm long) occurs as anhedral grains. K-feldspar occurs as anhedral grains. Biotite (0.2–2.0 mm long) and muscovite (0.2–1.6 mm long) occur as subhedral grains.

(7) Toki Granite (Fig. 2.5f): Fine-grained biotite muscovite granite with an equigranular texture or rarely porphyritic texture. It is mainly composed of quartz, plagioclase, K-feldspar, biotite and muscovite, with accessories of apatite, allanite, titanite, zircon, and opaque minerals. Plagioclase (0.2–1.4 mm long) occurs as subhedral–euhedral grains with weak zoning. Plagioclase phenocrysts as large as 7.1 mm in length were observed. Quartz (0.3–2.0 mm long) occurs as anhedral grains. Quartz phenocrysts as large as 8.3 mm in length were observed. K-feldspar occurs as anhedral grains. Biotite (0.2–1.0 mm long) and muscovite (0.2–0.4 mm long) occur as subhedral grains.

2.3. Regional metamorphism of the Ryoke Belt

The Ryoke metamorphic rocks have been subdivided into a number of mineral zones, with the highest-grade zone being lower granulite facies (800°C at 600 MPa; Ikeda, 2002, 2004). The main metamorphism occurred during mid-Cretaceous times (c. 100 Ma; Suzuki and Adachi, 1998). The protolith of the metamorphic rocks is considered to be a Jurassic accretionary complex of the Mino–Tanba Terrane (Nakajima, 1994; Okudaira and Suda, 2011). The Ryoke metamorphism was caused by the intrusion of the older Ryoke granitoids (Ikeda, 1998; Okudaira et al., 2001; Miyazaki, 2010).

2.4. Deformation events of the Ryoke Belt

Three generations of ductile deformation structures are recognized within the Ryoke Belt (D_1, D_2 and D_3; Hara et al., 1991; Okudaira et al., 1993, 2001; Okudaira and Suda, 2011). D_1 is the time of schistosity-forming deformation during the intrusion of the older granitoids (Wallis and Okudaira, 2016). Many kinds of asymmetric deformation structures such as intrafolial folds with axial planes parallel to the schistosity, slightly rotated boudins of quartzo–feldspathic veins and thin layers of metachert, extensional crenulation cleavages, and rotated porphyroblasts are reported (Wallis and Okudaira, 2016). The deformation at the D_1 occurs at the time of low-pressure high-temperature type metamorphism (Okudaira and Suda, 2011) and D_1 is considered to be about 100 Ma from the monazite CHIME age of metamorphic rocks (Suzuki et al., 1994a, 1994b). D_2 is the time of localized deformation that formed granite mylonites near the MTL (Okudaira and Suda, 2011). D_2 mylonite zone, referred to as the Kashio mylonite zone or the Ryoke southern marginal shear zone, formed within the Ryoke Belt during sinistral top-to-the-west shearing along the MTL (Takagi, 1986; Sakakibara, 1996; Shimada et al., 1998). Two deformation periods (1st: 95–85 Ma and 2nd:

70–65 Ma) are known, and the deformation condition is >450°C and 450–300°C, respectively (Michibayashi and Masuda, 1993; Takagi, 1997). D_3 is the time of the series of uplifting folds with east–west-trending axes, which occurred during and/or after D_2 mylonitization (Shimada et al., 1998; Okudaira et al., 2001). The younger granitoids intruded during and after the formation of the D_3-uplift folds (Nishiwaki and Okudaira, 2007; Wallis and Okudaira, 2016).

2.5. Movement history of the MTL

About the history of the activity of the MTL, Yehara (1936) suggested that there are multiple stages in the activity of the MTL, and Kobayashi (1941) reported that there were four activity stages. After that, Ichikawa (1980) subdivided the activity stages into five: the Kashio phase, the Ichinokawa phase, the Tobe phase, the Ishizuchi phase and the Shobutani phase. A study to estimate the timing of the MTL activity was conducted after the latter half of the 1980s, K–Ar dating of authigenic mica clay mineral (e.g. illite) in fault gouge (Shibata and Takagi, 1988; Shibata et al., 1988; Takagi et al., 1989, 1991; Shibata and Uchiumi, 1992; Tanaka et al., 1992), fission-track (FT) dating of zircons in tuff (Kashima and Takechi, 1996; Narita et al., 1999) and K–Ar dating of biotite in tuff (Takeshita et al., 2000). I summarize the movement of the MTL in each activity stage following Kubota and Takeshita (2008).

The Kashio phase is the birth stage of the MTL, which formed as granite mylonite zones by sinistral shear in the southern marginal part of the Ryoke Belt (Hara et al., 1977; Takagi, 1997; Kubota and Takeshita, 2008). The mean grain size of recrystallized quartz shows a value of 50 μm or less within 500 m from the MTL (Hayashi and Takagi, 1987; Takagi, 1986; Michibayashi and Masuda, 1993).

The Ichinokawa phase (63–58 Ma; Takagi and Shibata, 1992) is the movement stage of the MTL, during the formation of the sedimentary basin of the Upper Cretaceous Izumi Group, and its subsequent juxtaposition against the Sanbagawa metamorphic rocks occurred (Kubota and Takeshita, 2008). Since this phase is in agreement with the oldest age of the MTL fault gouge (Shibata et al., 1989) and pseudotachylyte developed in the Ryoke granites (Takagi et al., 2010), it is considered that the MTL started to deform in a brittle manner in this phase. The Izumi sedimentary basin formed as a pull-apart basin, which resulted from a left-lateral strike-slip along the MTL in this phase (Miyata et al., 1980). Fault, boudinage and north-vergent folds in the Izumi Group along the MTL show normal faulting along the MTL (Kubota and Takeshita, 2008). Therefore, the MTL movement in the Ichinokawa phase is thought to include the left-lateral strike-slip and top-to-the-north normal faulting associated with the early stage of exhumation of the Sanbagawa schist (Kubota and Takeshita, 2008).

The pre-Tobe phase (45–25 Ma; Takagi and Shibata, 1992; Takagi et al., 1992) defined

by a north–south-directed shortening, which is responsible for a large-scale folding of the Izumi Group and thrusting of the Northern over the Southern Izumi Belt (Kubota and Takeshita, 2008).

The Tobe phase (16–15 Ma; Kubota and Takeshita, 2008; Takeshita, 2010) defined as the movement stage of the MTL when the Izumi Group thrust over the Lower Miocene Kuma Group (Takagi et al., 1992; Takahashi, 1992). Dragging deformation of the Kuma Group (Takahashi, 1992), cataclastic deformation of the Izumi Group (Kubota, 2015) and thrust of dolomitic schist between the Izumi Group and the Kuma Group (Takagi et al., 1992) are reported as the deformation structures due to the thrust of the MTL.

The Ishizuchi phase (14–10 Ma; Takagi and Shibata, 1992) defined as the intrusion of igneous rock of the Middle Miocene along the MTL (Shibata and Nozawa, 1968; Tazaki et al., 1990; Tatsumi et al., 2010) and Subsequent faulting that cut these (Suyari and Akojima, 1974; Takagi et al., 1992). Takagi et al. (1992) pointed out that a top-to-the-north normal faulting has overprinted in this phase in the dolomitic schist which was thrusted at the Tobe phase.

The Shobutani phase (2 Ma–present; Ichikawa, 1980; Kubota and Takeshita, 2008) defined as the phase when the MTL has been reactivated as right-lateral strike-slip active fault in southwest Japan (Okada, 1973; Sangawa, 1977; Okada, 2012).

Chapter 3: Determination of the regional paleostress field using healed microcracks

3.1. Introduction

Granitic bedrocks contain macroscopic fractures (joints, faults), mesoscopic cracks (mesocracks) and microscopic cracks (microcracks). Since the meso- to microcracks affect physical properties of bedrocks such as strength, elastic wave velocities, a thermal conductivity and permeability, many studies on the effects of meso- to microcracks have been reported (Yoshida et al., 1989; Takemura and Oda, 2002; Nara and Kaneko, 2006; Ishise et al., 2006; Takeuchi et al., 2013). If anisotropy of rocks and constituent minerals due to the existence of cleavage is negligible, the microcracks preferably form normal to the minimum principal stress (σ_3) axis (Tuttle, 1949). Therefore, after this description by Tuttle (1949), many studies have been carried out to estimate the paleostress direction based on the orientation distribution of microcracks in quartz grains (Plumb et al., 1984; Lespinasse and Pecher, 1989; Vollbrecht et al., 1991; Takeshita and Yagi, 2001; Takagi et al., 2008, 2012; Nadan and Engelder, 2009; Sato and Takagi, 2010). The microcrack has an advantage that it is possible to estimate deformation histories from a small oriented sample taken from an outcrop or from a drilling core (Kowallis et al., 1987; Takagi et al., 2008). In previous studies, only the orientation of the σ_3 axis could be estimated. However, orientations of all principal stress axes and a stress ratio can be recently estimated (Baer et al., 1994; Yamaji et al., 2010). These methods are extended further, even if microcracks recorded several tectonic stages, new methods can separate and detect the paleostress per stage (Yamaji and Sato, 2011; Yamaji, 2016). In this study, applicable conditions to use the new method for microcrack analyses were examined, and a method to estimate the orientation distribution of microcracks was developed. Furthermore, the paleostress during the Late Cretaceous granitoids in Chubu region was estimated.

3.2. Microcrack

3.2.1. Previous studies of the microcrack

A microscopic crack in rocks and minerals is called microcrack. Simmons and Richter (1976) defined the word “microcrack” as “an opening that occurs in rocks and has one or two dimensions smaller than the third. For flat microcracks, one dimension is much less than the other two and the width to length ratio, termed crack aspect ratio, must be less than 10^{-2} and is typically 10^{-3} to10^{-5}. The length…typically is of the order of 100 μm or less”. Many studies have been reported using microcracks as described below. The process of healing and sealing

of crack based on the cathode luminescence observation (Sprunt and Nur, 1979; Laubach et al., 2004; Laubach and Diaz–Tushman, 2009). Estimate the deformation conditions such as temperature, pressure, salinity and other compositional data using fluid inclusions and secondary minerals form microcracks (Hay et al., 1988; Evans, 1995; Lespinasse, 1999; Laubach, 2003; Fischer et al., 2009). Estimate the paleostress conditions using the orientation distribution of microcracks (Plumb et al., 1984; Lespinasse and Pecher, 1986; Vollbrecht et al., 1991; Takeshita and Yagi, 2001; Takagi et al., 2008; 2012; Nadan and Engelder, 2009; Sato and Takagi, 2010).

3.2.2. Classification and occurrence of microcracks

Microcracks are classified into three types (healed microcrack, sealed microcrack and open microcrack; Fig. 3.1) on the basis of origin (Padvani et al., 1982). Healed microcrack (HC) is a fracture that has been healed by the same mineral of mother crystal. HC is recognized as the fluid inclusion plane under the microscope. However, not all of fluid inclusions constitute the HC. Fluid inclusions are classified into four types (primary inclusion, secondary inclusion, pseudosecondary inclusion and exsolution inclusion; Fig. 3.2a) on the basis of the formation processes (Takenouchi, 1975; Roedder, 1983, 1984; Sander and Black, 1988). Primary inclusions are trapped during the growth of the surrounding host crystal. Primary inclusions are distributed randomly within the cores of crystal and sometimes show a distinctive shape called negative crystal. Secondary inclusions are formed after the crystal growth has completed. If a fracture has been formed after the crystal growth, some fluids may enter the fracture and become trapped as fluid inclusions. The process of splitting from the large inclusion to small inclusions called necking down (Roedder, 1962; Fig. 3.2b). Pseudosecondary inclusions have been formed by the same process as secondary inclusions, but fracturing and healing have taken place at some point or points during the growth of the crystal. Therefore, unlike the secondary inclusion, pseudosecondary inclusions are not continuous to the outside of the crystal. Exsolution inclusions form as a result of internal isochemical phenomena within the crystal (Sander and Black, 1988). Among these fluid inclusions, secondary and pseudosecondary inclusions are able to use to estimate the paleostress. However, since it is difficult to identify the types of the fluid inclusions, all of the fluid inclusion planes that can be observed under the microscope were used to analysis. Sealed microcrack (SC) is a fracture has been sealed by secondary minerals such as carbonate minerals, chlorite, K-feldspar, plagioclase, prehnite, barite, pyrite and magnetite (Hay et al., 1988; Takeshita and Yagi, 2001; Laubach, 2003). Open crack (OC) is a fracture that surface is opened.

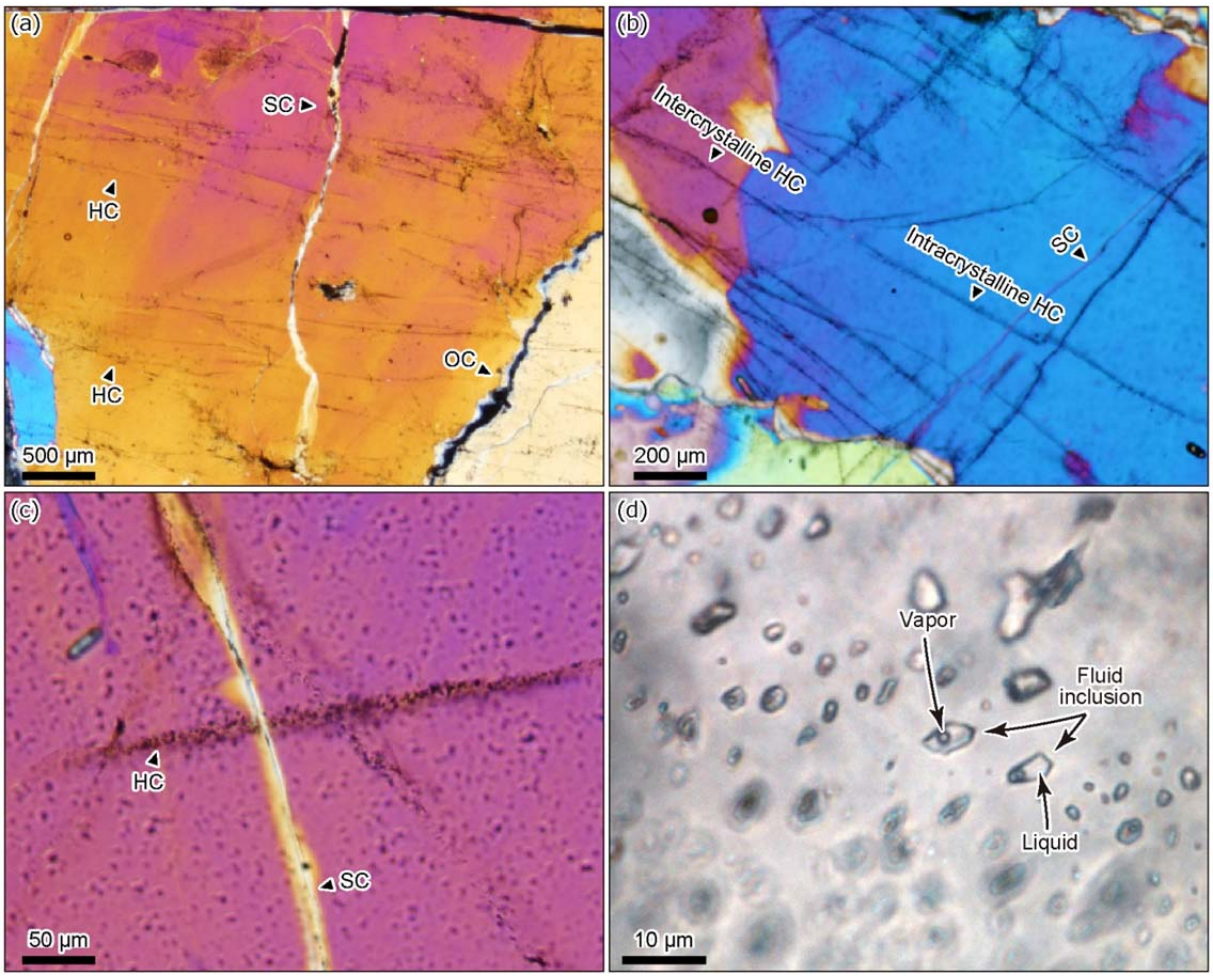

Fig. 3.1. Photomicrographs of microcracks developed in quartz grains (XPL). (a) Several kinds of microcracks (sample In-9). (b) Intercrystalline and intracrystalline HCs showing similar orientation (sample Tn-6). (c) Cross-cutting relationships between earlier HC and SC (sample Tn-6). (d) Fluid inclusions constituting HC in quartz (sample MT-1).

Microcracks are also classified into four types (grain boundary crack, intracrystalline crack, intercrystalline crack and cleavage crack; Fig. 3.2c) on the basis of the occurrence (Kranz, 1983). Grain boundary cracks are those along the grain boundary. Intracrystalline cracks are relatively small, usually less than a grain diameter in length and about 1 μm or less in width. Intercrystalline cracks are longer and often wider than the intracrystalline cracks, but are otherwise morphologically similar. Intercrystalline cracks are transgranular and are easily seen at low magnifications. Cleavage cracks are spaced and separated crakcs along cleavage planes in the mineral. They are often seen to occur in parallel sets of various lengths within one grain. The intergranular and intragranular microcracks in quartz grains were analyzed to estimate the paleostress.

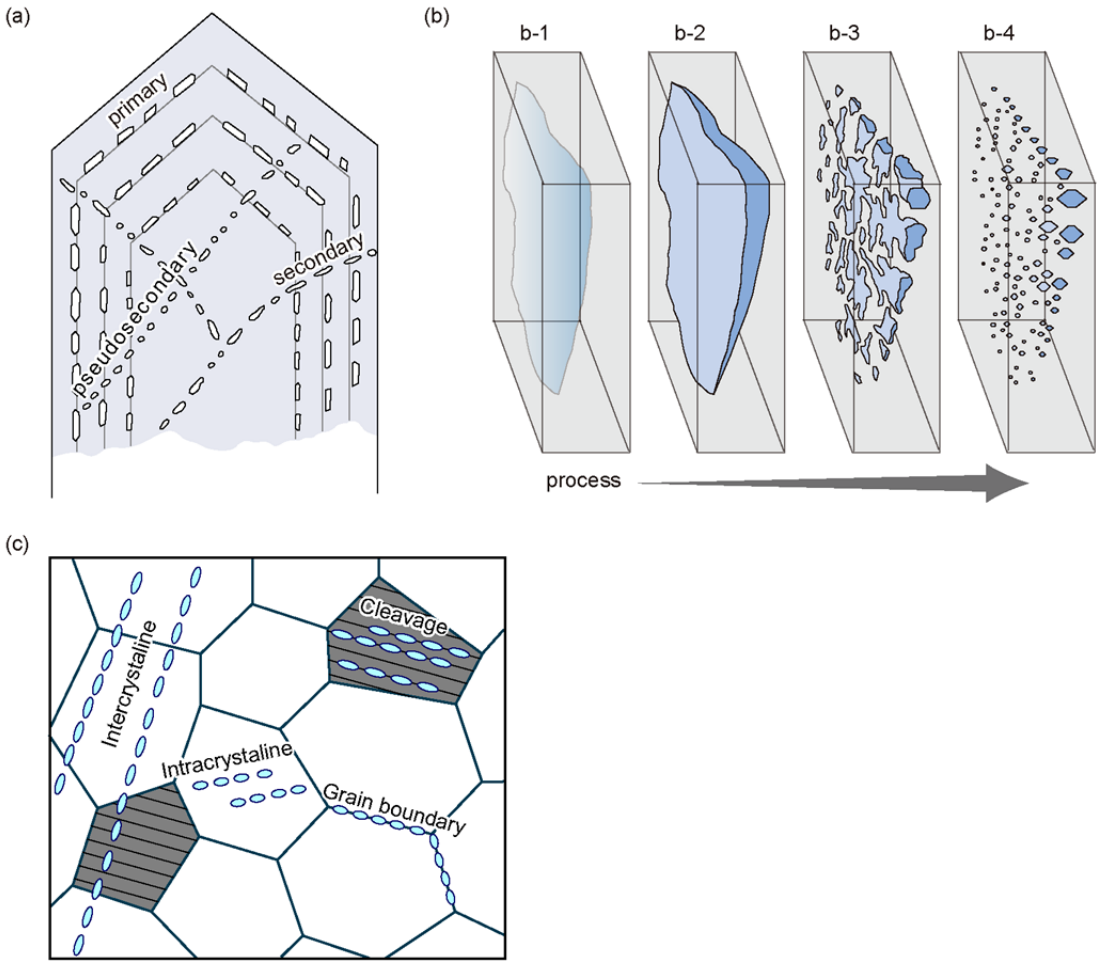

Fig. 3.2. (a) Schematic occurrence of healed crack (modified after Sawaki, 2003). (b) Formation process (modified after Roedder, 1962). (b-1) Forming a fracture, (b-2) infiltration of a liquid, (b-3) Solution and rprecipitation of material from the liquid on the fracture surface results in dendritic growths, which meet and close off small volumes of liquid, (b-4) decreasing gradually lose surface area and become rounded bubbles or hollow negative crystals. (c) Occurrence of microcracks, modified after (Randive et al., 2014).

3.2.3. Conditions of microcrack formation

Healing of microcracks is caused by diffusion of silica on the crack surface and in the fluid (Smith and Evans, 1984; Brantley et al., 1990; Sawaki, 2003). Although the healing rate is affected by the shape and the opening width of the crack surface and silica concentration of a fluid, it is expressed as an exponential function of temperature (Hickman and Evans, 1987). According to Smith and Evans (1984), a crack that heals completely in 2 days at 400°C would require several months to years at 200°C. The formation conditions of fluid inclusions constituting the HC can be estimated by fluid inclusion microthermometry (Sawaki, 2003; Takagi et al., 2008, 2012; Jang and Kang, 2011), and it is considered that the HC is formed at a temperature of above 200°C. On the other hand, a low temperature below 200°C causes the healing rate decrease and formation of the SC (Takeshita and Yagi, 2001). Sealing by secondary minerals can be faster than the growth of crystal at this temperature (Lander and

Laubach, 2014). Takagi et al. (2008, 2012) have been reported the cross-cutting relationship between earlier HC and later SC, and the same cutting relationship was observed in this study (Fig. 3.1c).

3.3. Dike method

The method to estimate paleostress based on the orientations of dilational fractures such as dikes, mineral veins and microcracks are called dike method (Anderson, 1951). Studies and progress of the dike method have been reviewed by Marinoni (2001) and Yamaji (2012). Extension fractures have been thought to be perpendicular to the regional σ_3 axis (e.g. Anderson, 1951; Nakamura, 1977). In other words, orientations of σ_3 axis can be estimated by the maximum concentration orientation of dike poles. This method is applied to microcracks and many studies have been estimated paleostress using the orientation distribution of microcracks (Plumb et al., 1984; Lespinasse and Pecher, 1986; Vollbrecht et al., 1991; Takeshita and Yagi, 2001; Takagi et al., 2008; 2012; Nadan and Engelder, 2009; Sato and Takagi, 2010).

However, earlier studies can estimate only the orientation of σ_3 axis. The method to estimate the orientation of the maximum and intermediate compressive principal stress (σ_1 and σ_2) axes has been developed by Delaney et al. (1986) and subsequent studies (e.g. Baer et al., 1994; Jolly and Sanderson, 1995, Yamaji et al., 2010). Delaney et al. (1986) formulated the criterion for re-opening of pre-existing fractures as

$$P_{\mathrm{f}} \geq \sigma_{\mathrm{N}} \tag{3.1}$$

where P_{f} is the pressure of the fluid which makes dikes or cracks, and σ_{N} is the tectonic normal stress acting on the fracture surface. Although this criterion neglects tensile strength of pre-existing fracture, the criterion will be satisfied with σ_{N} is low. In other words, dikes or cracks are easy to form perpendicular to the σ_3 axis and difficult to form perpendicular to the σ_1 axis. In this case, the variation in the orientation of dikes or cracks is determined by stress ratio defined as $\Phi = (\sigma_2 - \sigma_3)/(\sigma_1 - \sigma_3)$ and dimensionless normalized fluid pressure defined as $p = (p_{\mathrm{f}} - \sigma_3)/(\sigma_1 - \sigma_3)$ (Yamaji et al., 2010). Therefore, by assuming a frequency distribution of p, it can be expressed the orientation distribution of dikes or cracks in the distribution function. Yamaji et al. (2010) assumes an exponential distribution as a frequency distribution of p and proposed a method to determine all principal stress axes orientations and the stress ratio by fitting the Bingham distribution (Bingham, 1974; Fig. 3.3) to the orientation distribution of the dike poles. The Bingham distribution has the probability density,

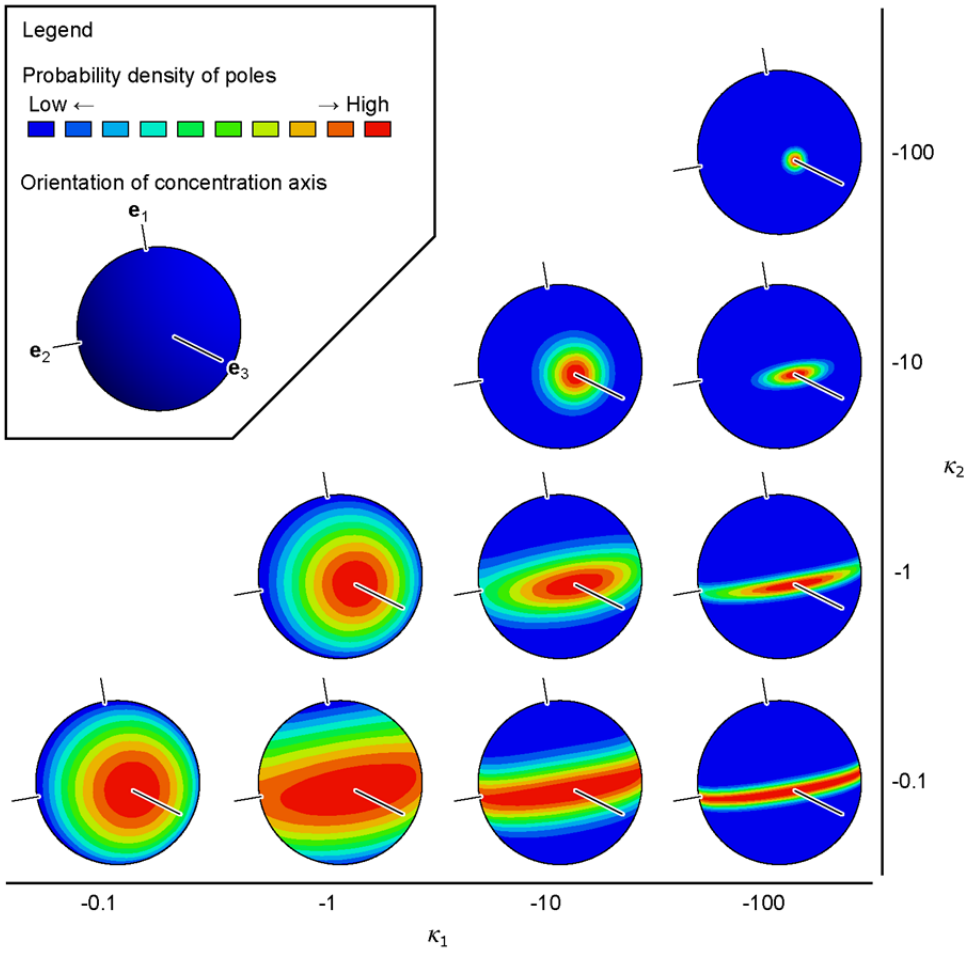

Fig. 3.3. Probability densities of the Bingham distribution with different κ_1 and κ_2 values on the sphere. The contour intervals are different on each projection: the range between the minimum and maximum densities is divided into 10 intervals

$$P_{\mathrm{B}}(\mathbf{v}|\mathbf{K},\mathbf{E}) = \frac{1}{A}\exp\left(\mathbf{v}^{\mathrm{T}}\mathbf{E}^{\mathrm{T}}\mathbf{K}\mathbf{E}\mathbf{v}\right) \tag{3.2}$$

where $\mathbf{v}$ is the unit vector representing an orientation, A is the normalization constant, T indicates matrix transpose, $\mathbf{E} = (\mathbf{e}_1, \mathbf{e}_2, \mathbf{e}_3)$ is the orthogonal matrix representing the axes of the minimum, intermediate and maximum concentrations, respectively, and $\mathbf{K} = \mathrm{diag}(\kappa_1, \kappa_2, 0)$ is the matrix characterizing the distribution (Bingham, 1974; Onstott, 1980; Yamaji et al., 2010). The parameters, κ_1 and κ_2 ($\kappa_1 \leq \kappa_2 \leq 0$) are negative in sign, and their absolute values denote concentrations. In this case, stress ratio, Φ, correspond with κ_2/κ_1, and the correspondence of the σ_1, σ_2 and σ_3 axes with the minimum, intermediate and maximum concentration axes, respectively (Yamaji et al., 2010). The development of this approach, dike method has evolved as a method can estimate the σ_1, σ_2 and σ_3 axes and stress ratio.

Incidentally, rocks commonly contain several HC clusters reflecting differences in stress orientation over geologic history (e.g. Dezayes et al., 2000; Laubach and Diaz–Tushman, 2009). In this study, several HC clusters were detected using mixed Bingham distribution model (Yamaji and Sato, 2011; Fig. 3.4). The mixed Bingham distribution has the

probability density,

$$P_{\mathrm{mB}}(\mathbf{v}|\boldsymbol{\theta},\boldsymbol{\varpi}) = \sum_{k=1}^{K} \varpi^k \, P_{\mathrm{B}}\left(\mathbf{v}\middle|\mathbf{x}^k\right) \tag{3.3}$$

where $\mathbf{x}$ is a five-dimensional vector one-to-one correspondence with ($\mathbf{K}$,$\mathbf{E}$), $P_{\mathrm{B}}(\mathbf{v}|\mathbf{x})$ is the probability density of the Bingham distribution with the parameters that are denoted by $\mathbf{x}$, K is the number of elliptical clusters or girdles, and ϖ^k is the compounding ratio or the mixing coefficient (Bishop, 2006) of the kth Bingham distribution of which parameters are represented by $\mathbf{x}^k$ (Yamaji and Sato, 2011). The coefficients satisfy $0 < \varpi^k \leq 1$ and $\varpi^1 + \varpi^2 + \cdots + \varpi^K = 1$; ϖ^k means the significance of the kth subset. The argument, $\boldsymbol{\theta}$, of the function P_{mB} in Eq. (3.3) stands for all the K vectors: $\boldsymbol{\theta} = \left\{\mathbf{x}^1, \mathbf{x}^2, \cdots, \mathbf{x}^K\right\}$, and another argument of the function is $\boldsymbol{\varpi} = \left\{\varpi^1, \varpi^2, \cdots, \varpi^K\right\}$. Yamaji and Sato (2011) introduce the Bayesian information criterion (BIC; Schwarz, 1978) to estimate the number of clusters, K. The function of the BIC described as

$$\mathrm{BIC} = -2\mathrm{L}\left(\hat{\boldsymbol{\theta}}, \hat{\boldsymbol{\varpi}}\right) + (6K - 1)\log_{\mathrm{e}} N \tag{3.4}$$

where N is the number of data. $\mathrm{L}(\boldsymbol{\theta}, \boldsymbol{\varpi})$ is the logarithmic likelihood function to evaluated the goodness of mixed Bingham distribution,

$$\mathrm{L}(\boldsymbol{\theta}, \boldsymbol{\varpi}) = \sum_{n=1}^{N} \log_{\mathrm{e}} P_{\mathrm{mB}}(\mathbf{v}_n|\boldsymbol{\theta}, \boldsymbol{\varpi}) \tag{3.5}$$

where $\mathbf{v}_n$ is the unit vector indicating the nth datum. The mixed distribution that best fits the N data is given by the optimal parameter set, $\left(\hat{\boldsymbol{\theta}}, \hat{\boldsymbol{\varpi}}\right)$, that maximizes this eq. 3.5. BICs are evaluated for various K values, and the values corresponding to the minimum BIC is chosen as the best. The mixed Bingham distribution with the best K value is thought to be the optimal mixture model for the given data (Yamaji and Sato, 2011). According to this, one of the HC that formed by any stress of the K stress, the probability of kth stress is quantitatively determined as $\varpi^k P_{\mathrm{B}}\left(\mathbf{v}\middle|\mathbf{x}^k\right)$. HC with a pole orientation $\mathbf{v}$ belong in the probability of

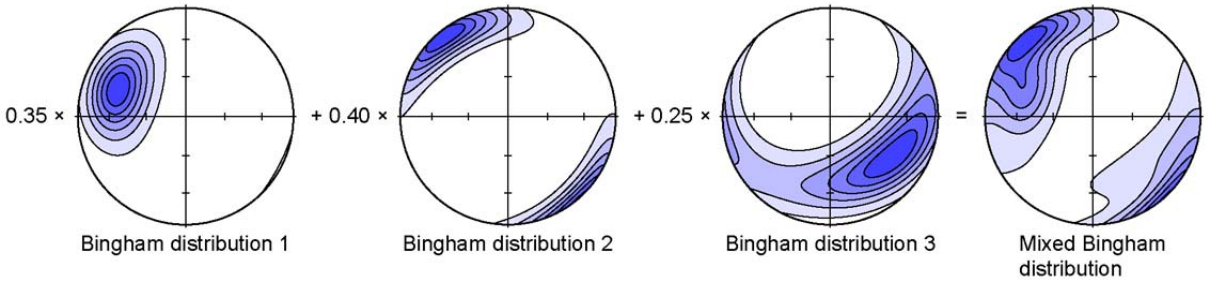

Fig. 3.4. Equal-area projections showing probability densities of the Bingham distributions 1–3, and their mixture distribution. The contour intervals are different on each projection: the range between the minimum and maximum densities is divided into 10 intervals.

$P_{\mathrm{B}}(\mathbf{v}|\mathbf{x}^1), \cdots, P_{\mathrm{B}}(\mathbf{v}|\mathbf{x}^K)$ to each K clusters. The responsibility of the kth one for the nth datum or the membership of the datum to the kth group is determined as $P_{\mathrm{B}}(\mathbf{v}|\mathbf{x}^k)/\sum_{k=1}^{K} P_{\mathrm{B}}(\mathbf{v}|\mathbf{x}^k)$. To estimate the optimal parameter set, $(\hat{\boldsymbol{\theta}}, \hat{\boldsymbol{\varpi}})$, Yamaji and Sato (2011) introduce expectation–maximization (EM) algorithm and Yamaji (2016) introduce the method that combines the genetic algorithm and EM algorithm. In this study, the parameter was estimated using the method by Yamaji and Sato (2011).

3.4. Estimates of orientation distribution of HC

Procedure to estimate the orientation distribution of HC is the following four steps: 1) Make a thin-section, 2) Measurement of the orientation of HC, 3) Correct the observation bias and estimates three-dimensional orientation distribution of HC, 4) Make a contour diagram (Fig. 3.5). The paleostress was detected from each sample by fitting the mixed Bingham distribution of the estimated orientation distribution of HC by above four processes.

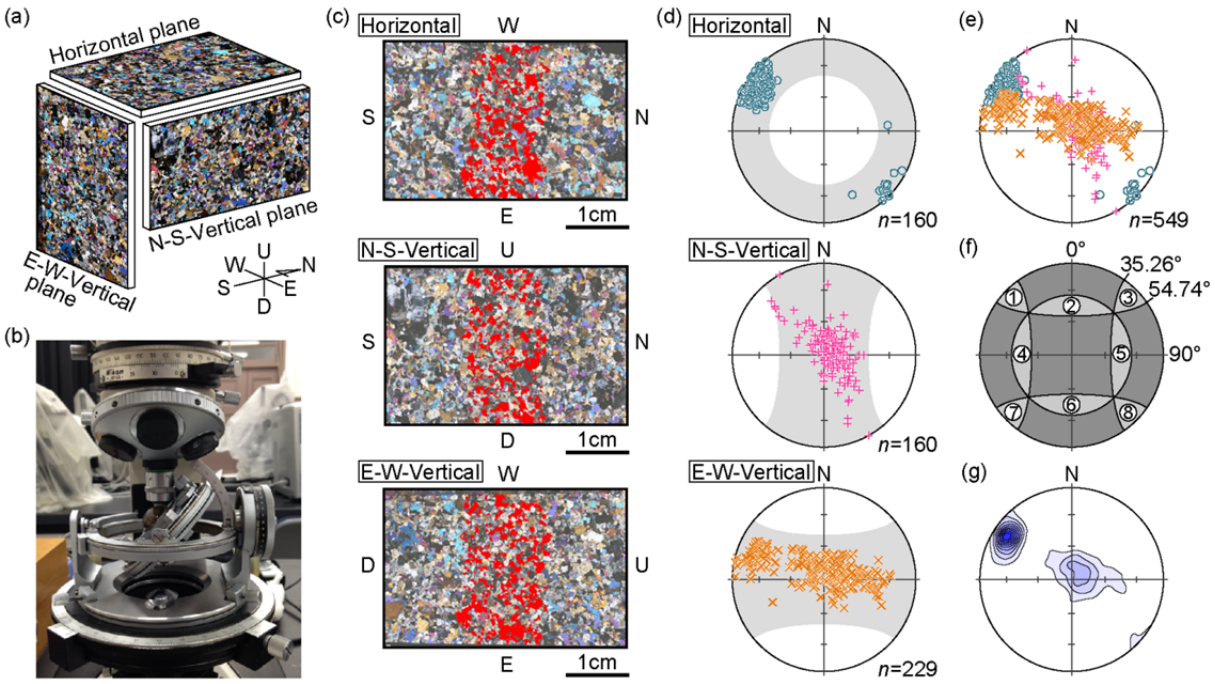

Fig. 3.5. The explanation for estimating the distribution of HCs, the example for sample Bs-3. (a) The relationship between three orthogonal observation planes (XPL). (b) Picture of universal-stage attached with microscope. (c) Overview of thin sections with quartz grains that can be observed in the universal-stage (red grains). (d) Pole figures of HCs with the direction that can be measured in the universal-stage (gray area), lower-hemisphere, equal-area projections. (e) Superposed projections of pole figures for HCs from three orthogonal observation planes. (f) Superposition of observation ranges from three orthogonal observation planes, modified after Vollbrecht et al. (1991). Pole of HCs in the numbered area can be measured in only one observation plane. (g) Gaussian contour diagram with levels are 10 % to 90 % (in 10 % increments) of the maximum density.

3.4.1. Thin-section preparations

An oriented samples were collected from outcrop and each thin-section of three orthogonal orientations (horizontal plane, N–S–vertical plane, E–W–vertical plane; Fig. 3.5a) were prepared. Since the dip of HC is measured using the information in the thickness direction of the thin-section, the thickness of thin-section was set at 0.05–0.10 mm. In this case, interference color of quartz indicates purple in the first order to blue in the second order.

3.4.2. Measurement of the orientation of HC

The orientation of HCs in each thin-section was measured using a universal-stage (Fig. 3.5b). By the mechanical constraints of the universal-stage, the range that can be observed in thin-section is limited to about one-third of the thin-section in the center (Fig. 3.5c). Previous studies have measured about 300 pieces of HCs in total by measuring the HCs of about 100 pieces from each thin-section (e.g. Takagi et al., 2008, 2012; Sato and Takagi, 2010). For Shinshiro Tonalite and Tenryukyo Granodiorite, measured the orientation of HCs about 100 pieces in each thin-section by randomly selected quartz grains following the method of the previous studies. For Busetsu Granite, Mitsuhashi Granodiorite, Inagawa Granodiorite and Toki Granite, measured the orientation of HCs from all observable quartz grains.

3.4.3. Correction of observation bias of the HC

The three-dimensional orientation distribution of HCs was estimated by integrating the orientation data measured from three orthogonal thin-sections (Fig. 3.5d, e). However, the orientation of HCs in each thin-section has an observation bias by the difference in the observable area and attitude of HC. Therefore, the method to correct the observation bias was examined, and the following three corrections have been made.

(1) Terzaghi correction (Terzaghi, 1965): Observation frequency of the planar structure such as the HC is proportional to the sine of the angle of intersection with the observation plane, θ. Therefore, the observed frequency of the HC with an intersection angle, θ, is $1/\sin\theta$.

(2) Universal-stage correction (Vollbrecht et al., 1991): By the mechanical constraints of the universal-stage, there are HCs which can be observed from two orthogonal orientations of thin-sections and only from one orientation of thin-section (Fig. 3.5f). Therefore, the observed frequency of HCs which can be observed from only one orientation of thin-section is 2-fold. Three-fold overlap was avoided by limiting the tilt angle of the universal-stage to 35°.

(3) Area correction: Since the total of the cross-sectional area of the observed quartz grains

in each thin-section is different, it is necessary to correct the observation bias of the HC depending on the abservation area. The value obtained by dividing the largest value of the observation area of the three orthogonal thin-sections by observation area of each thin-section was defined as a correction value. The observation area for Shinshiro Tonalite and Tenryukyo Granodiorite was the sum of the areas of quartz grains, that were used to measure the HCs in each thin-section. The procedure of the measurement contains the following four steps: 1) take a photograph of quartz grains under a microscope, 2) a photo printed enlarged in A4 and trace the grain boundaries manually, 3) reads the traced grain boundaries by the scanner, 4) obtains the number of pixels in the grains using an image analysis software Image J (public domain), and convert the number of resulting pixels into an actual area. On the other hand, an observation area for Mitsuhashi Granodiorite, Busetsu Granite, Inagawa Granodiorite and Toki Granite was the sum of the areas of all observable quartz grains. The procedure of measurement contains following two steps: 1) trace the grain boundaries manually using the pen tool in Photoshop (Adobe), 2) obtains the number of pixels in the grains using image analysis software Image J, and convert the number of resulting pixels into an actual area.

3.4.4. Estimating the density distribution of orientation

Create a pole figure and estimate the density distribution (Fig. 3.5g) based on the weighted Gaussian model by Robin and Jowett (1986). Contour levels are 10 % to 90 % (in 10 % increments) of the maximum density.

3.5. Results of paleostress analysis

The pole figure of HCs, contour diagrams by using a weighted Gaussian model, the result of clustering as a mixed Bingham model and their parameters are shown in Figs. 3.6–3.8 and Table 3.1. For example, four paleostress sets are detected from sample Mt-2. Principal stress axes in each of four paleostress sets are denoted by the symbol of a circle, a rhombic, an inverted triangle, a square and a triangle. The symbol colors red, green and blue show σ_1, σ_2 and σ_3, respectively. The membership of the HC for the four paleostress sets is represented by the color of the pole. For example, the pole has greater membership in the cluster 1 shows red and in the case of cluster 4 shows black. Since several paleostresses were detected from each sample, the paleostress that has σ_3 axis closest to the orientation of maximum density was deal with the prominent stress in the sample at the timing of HC formation (Fig. 3.9). Since sample In-2 has two peaks of the same degree of density, dealing wo paleostresses (cluster 1 and 2) as prominent stresses. The prominent stress grouped by

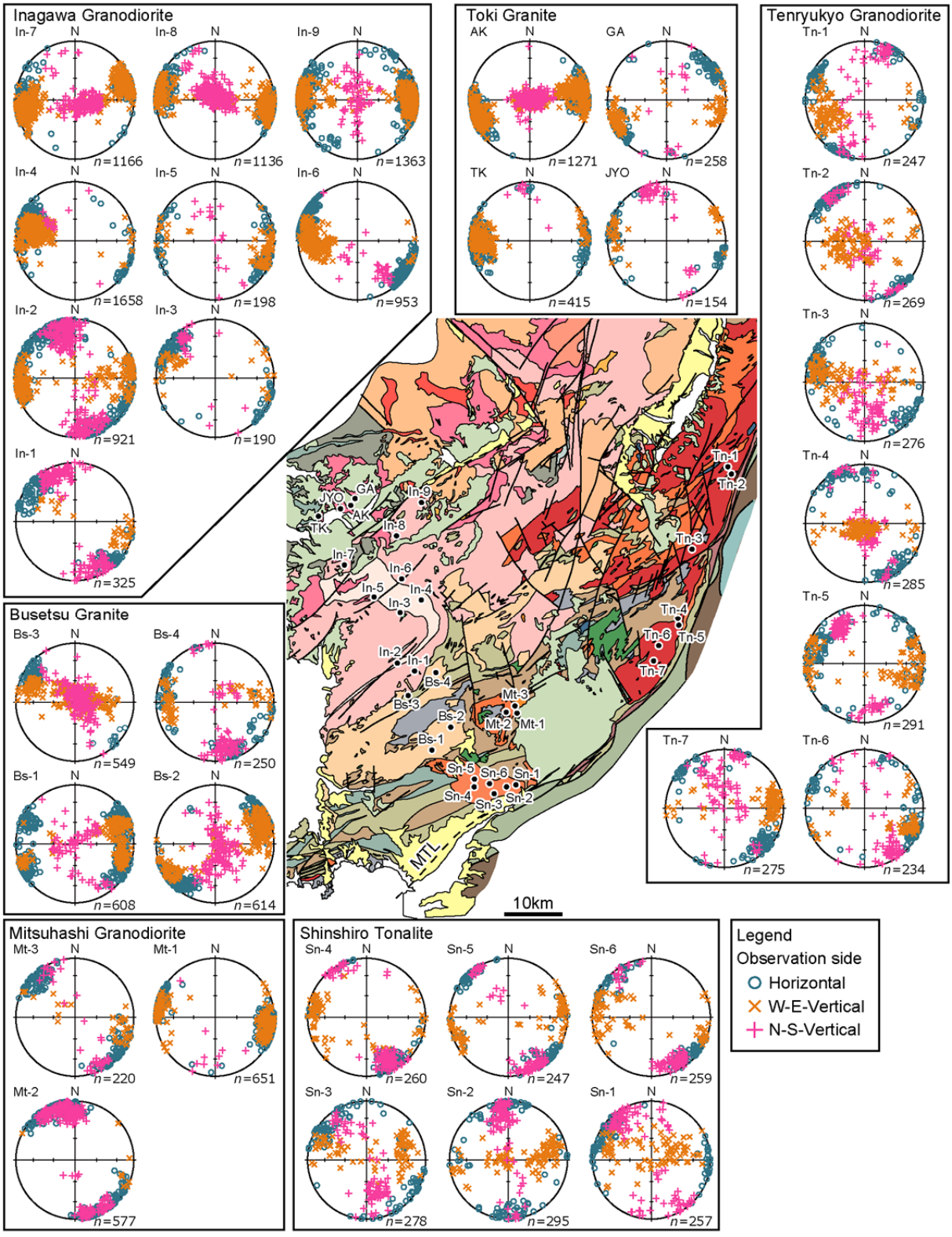

Fig. 3.6. Equal-area and lower hemisphere projections showing the pole figure. Pole symbol shows observation side wher HC was measured.

each granitoids are shown in Fig. 3.10. Prominent stresses detected from Tenryukyo Granodiorite except for the sample Tn-04 show σ_3 axis trends NW–SE and plunges at the low angle, whereas σ_2 and σ_1 axes are distributed in great circle normal to σ_3 axis. For the sample Tn-04, σ_3 axis trends 200° and plunges 80°, σ_2 axis trends 91° and plunges 3°, and σ_2 axis

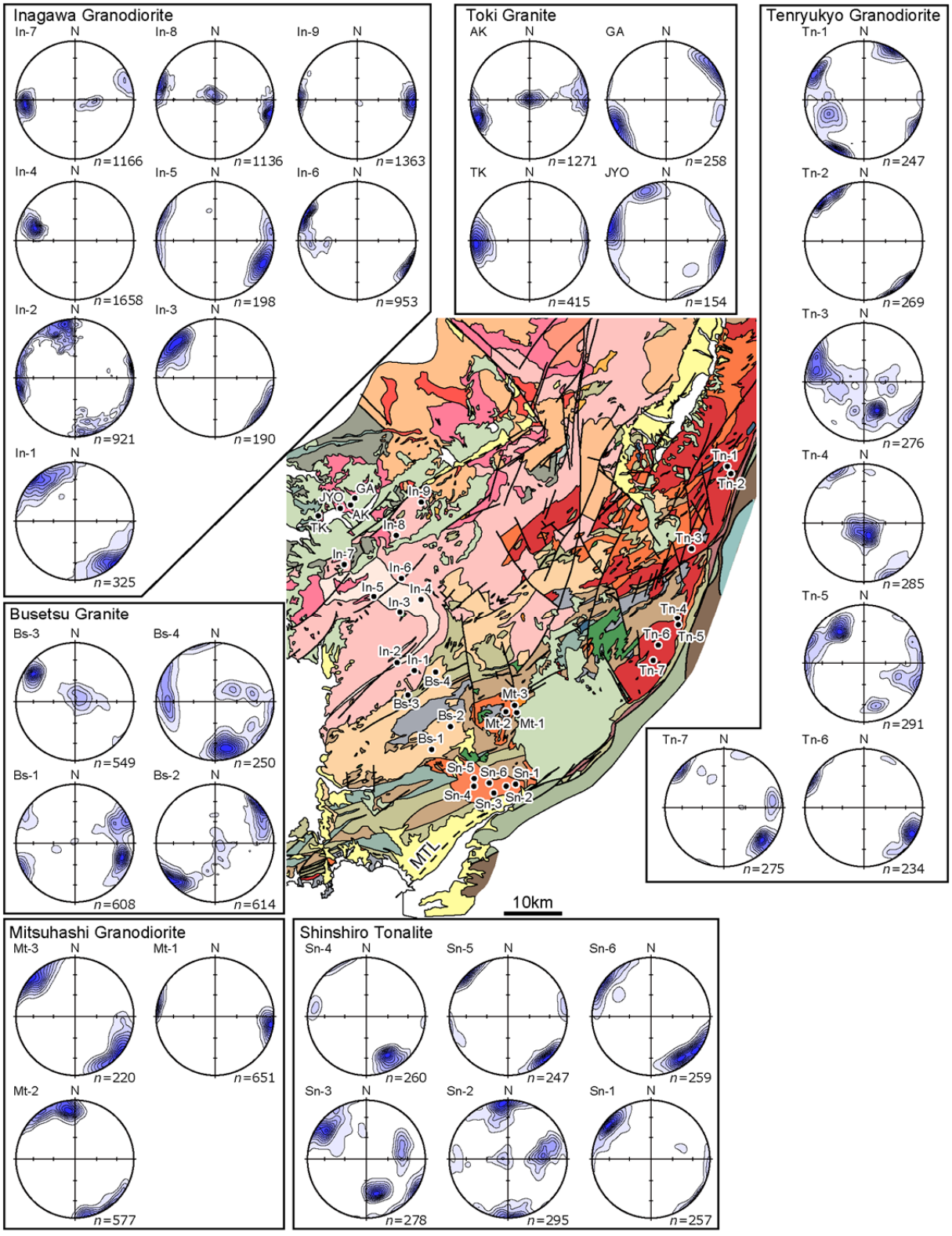

Fig. 3.7. Equal-area and lower hemisphere projections showing the Gaussian contours. The Gaussian contours with levels are 10 % to 90 % (in 10 % increments) of the maximum density.

trends 0° and plunges 9°. Samples were taken from the close location such as Tn-6 and Tn-7, and Tn-1 and Tn-2 show the same orientation of the principal stress axis of prominent stress.

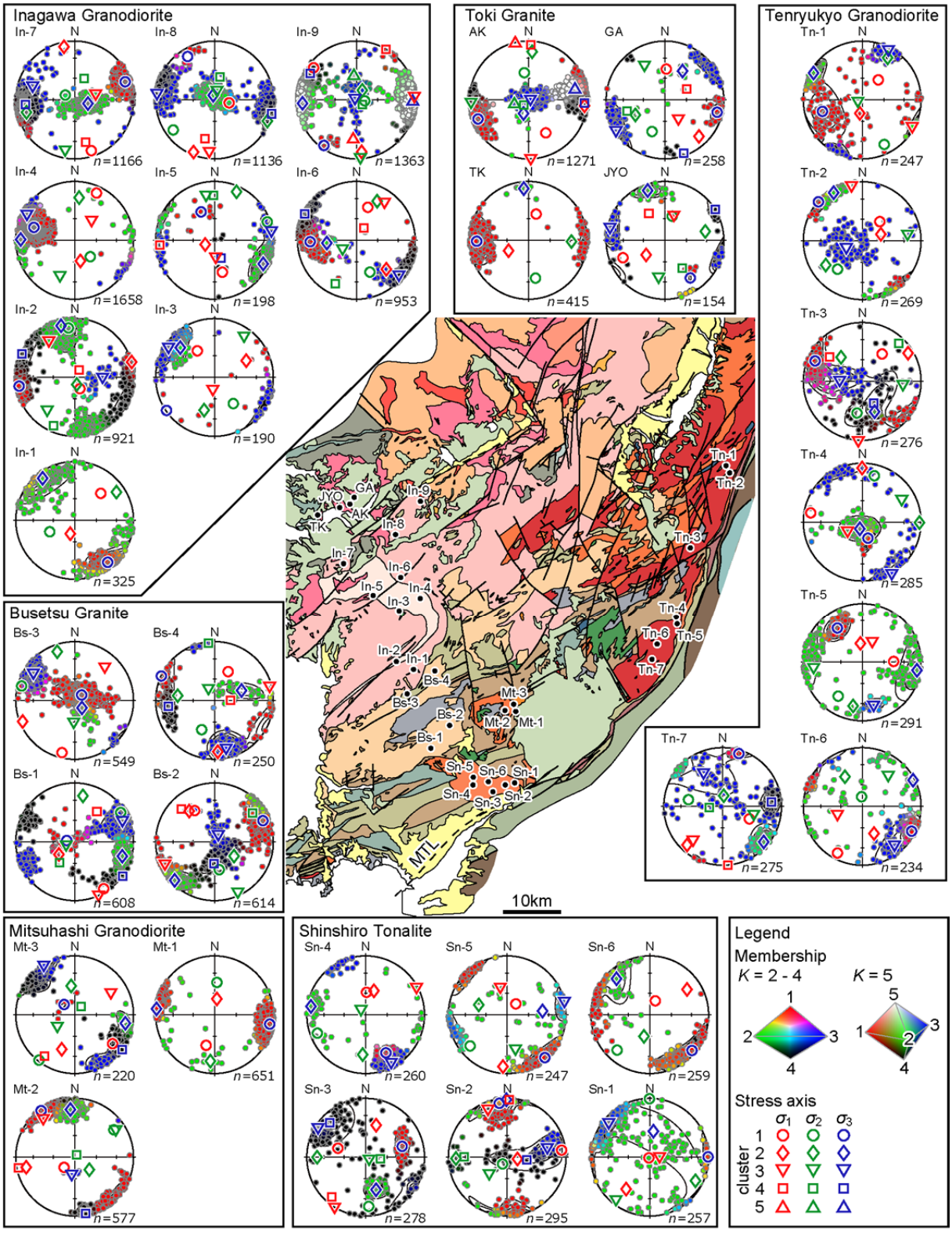

Fig. 3.8. Equal-area projections showing the optimum mixed Bingham distribution model. Contour levels are 10 % to 90 % (in 10 % increments) of the maximum density. The axes of stress are denoted by the symbol of a circle, a rhombic, an inverted triangle, a square and a triangle. The symbol colors red, green and blue show σ_1, σ_2 and σ_3, respectively. The tetrahedron with red, green, blue and black (K=2–4) or trigonal bipyramidal with red, green, blue, black and white (K=5) indicate the correspondence of the memberships with colors.

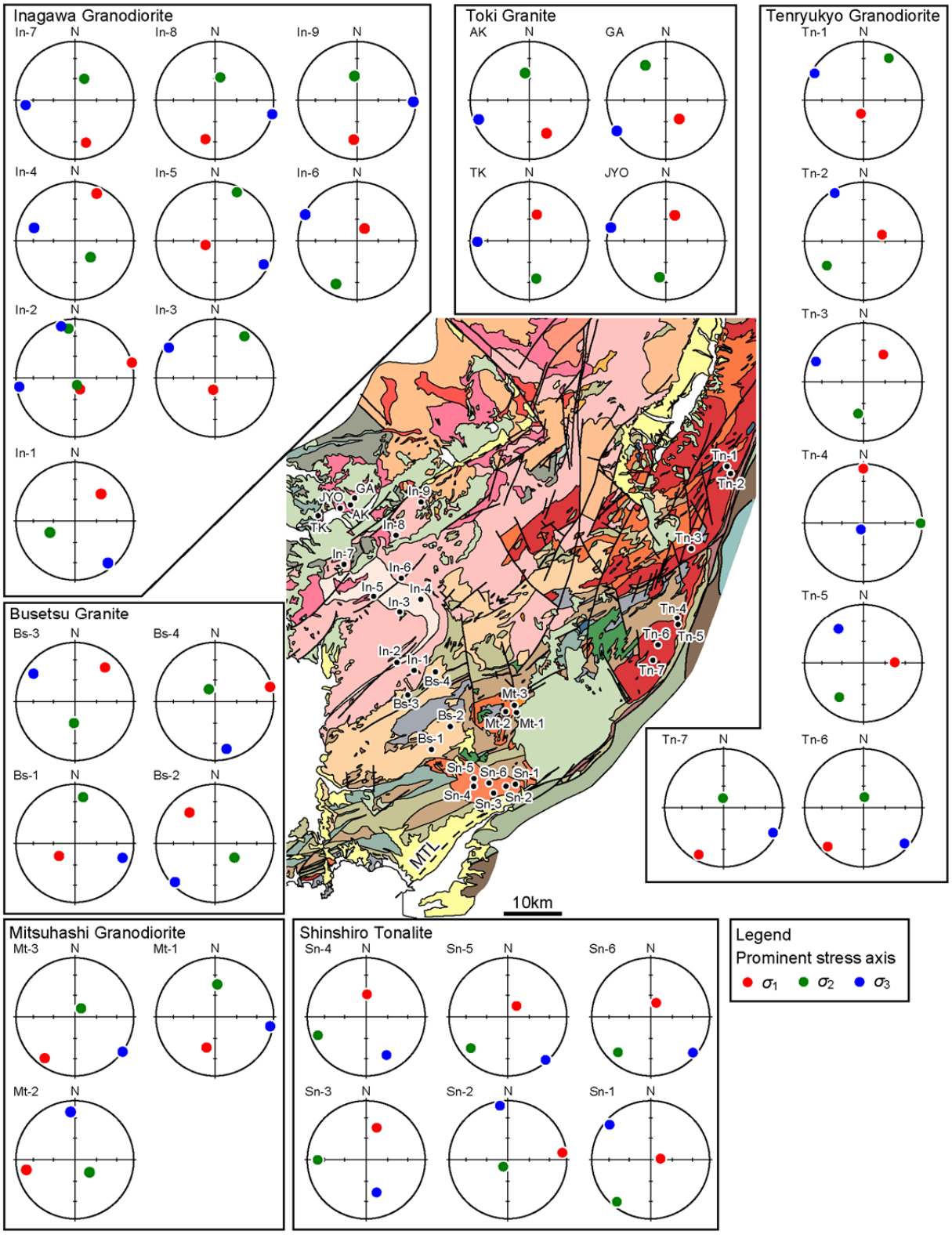

Fig. 3.9. Equal-area projections showing the prominent stress axes.

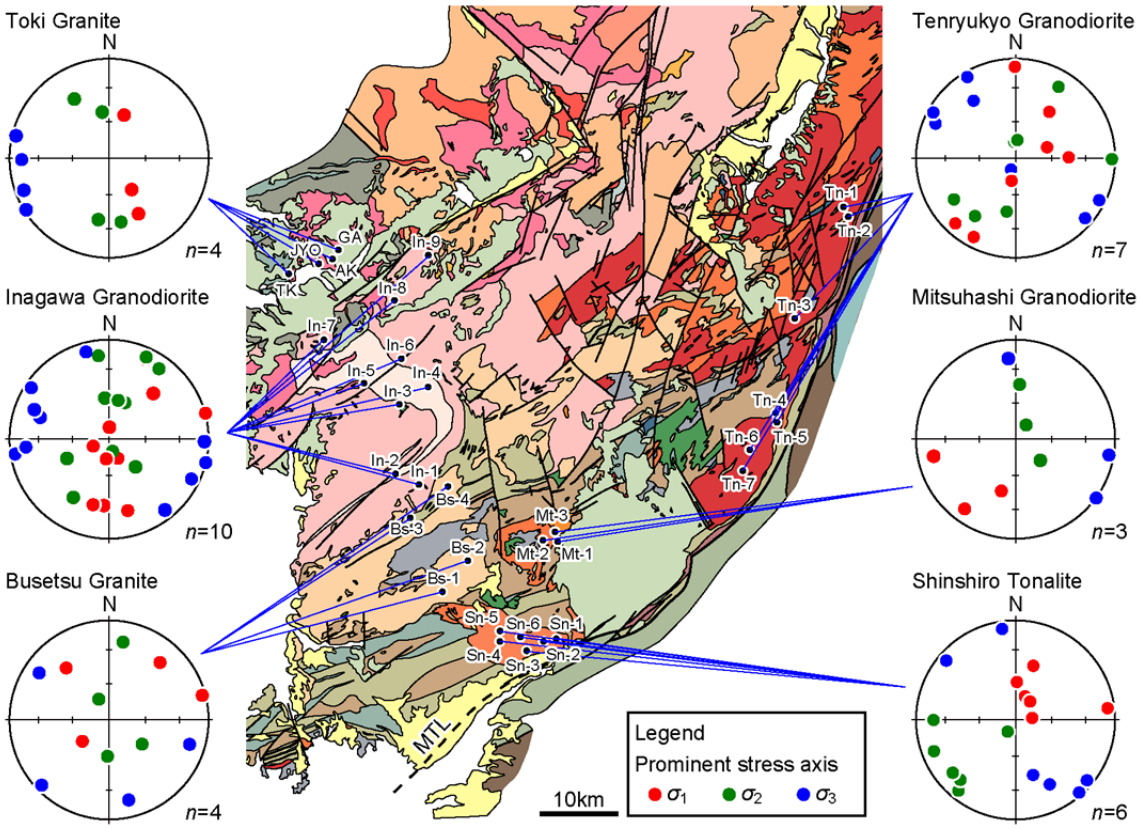

Fig. 3.10. Projections of principal stress axes of prominent stress grouped by the granitoid body (lower-hemisphere, equal-area projections).

Prominent stress detected from Shinshiro Tonalite, Busetsu Granite, Mitsuhashi Granodiorite, Inagawa Granodiorite and Toki Granite show the similar orientations of principal stress axes in the close location (c. 10 km) irrespective of the variation of the rock body. Therefore, these samples were classified into six groups A-F on the basis of their locations, and principal stress axes of each group are described below (Fig, 3.11).

Group A: σ_3 axis trends NW–SE and plunges at a low angle, σ_2 axis trends SW with low angle plunge and σ_1 axis trends N~E and plunges at a high angle.

Group B: σ_3 axis trends ESE and plunges at a low angle, σ_2 axis trends N~ESE and plunges at a high angle and σ_1 axis trends SW and plunges at a middle to low angle, hough the variation of stress axis orientation in the group is large.

Group C: σ_3 axis trends NNW–SSE and plunges at a low angle, σ_2 axis plunges approximately vertical and σ_1 axis trends NE and plunges at a low angle.

Group D: σ_3 axis trends NW–SE and plunges at a low angle, σ_2 axis trends NE–SW and plunges at a low angle and σ_1 axis plunges approximately vertical.

Group E: σ_3 axis trends E–W and plunges at a low angle, σ_2 axis trtends N with about 60° plunge and σ_1 axis trends S with about 30° plunge.

Group F: σ_3 axis trends W and plunges at a low angle, σ_2 and σ_1 axes trends N or S with

middle-angle plunges.

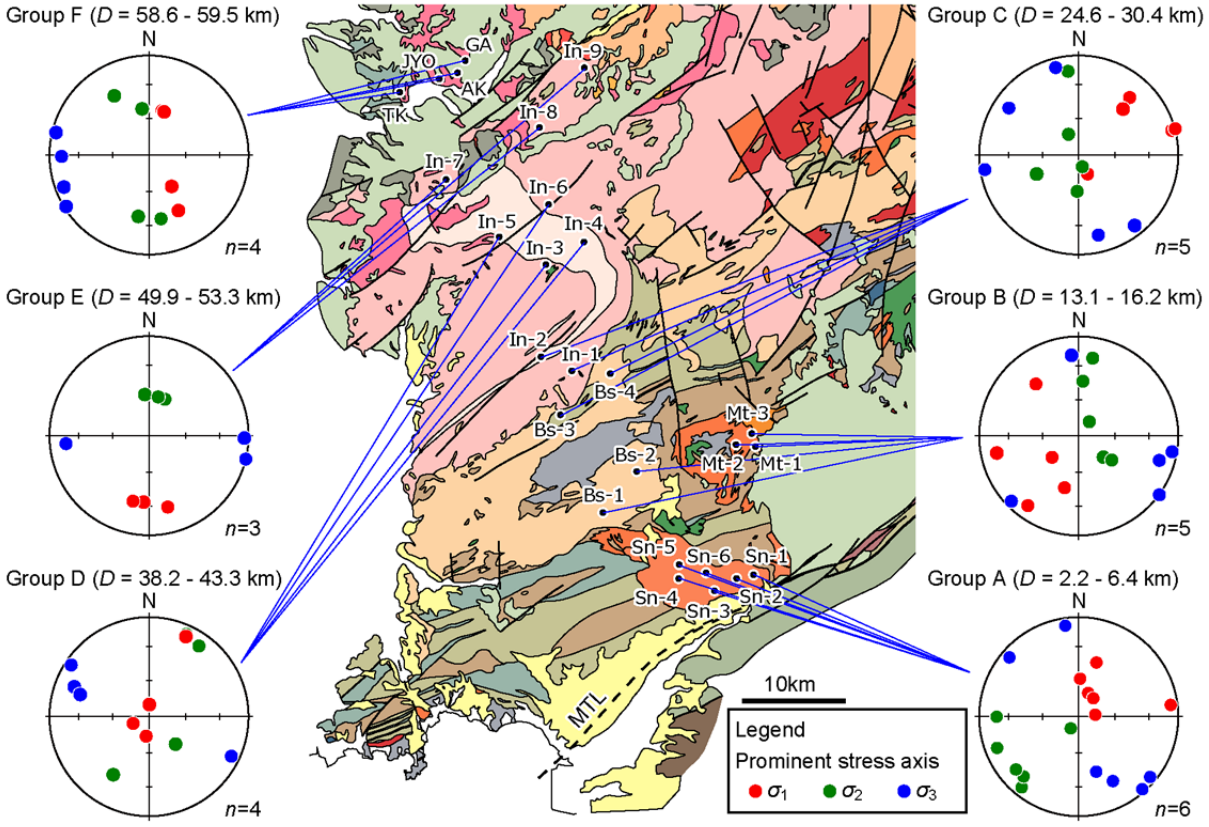

Fig. 3.11. Projections of the principal stress axis of prominent stress grouped by distance from the MTL (lower-hemisphere, equal-area projections).

3.6. Estimates of the condition and timing of HC formation

It is possible to estimate the trapping temperature of fluid inclusion constituting the HC using the homogenization temperature (Th) and freezing point temperature (Tm) of fluid inclusion (Vollbrecht et al., 1991; Takeshita and Yagi, 2001; Takagi et al., 2008, 2012). Th and Tm of 20 fluid inclusions constituting different HCs were measured in Shinshiro Tonalite, Mitsuhashi Granodiorite, Busetsu Granite, Inagawa Granodiorite and Tenryukyo Granodiorite. The doubly-polished thin sections with the thickness of 200–250 μm, the size of about 7 mm square were prepared, and L-600A/LK-600M (Linkam Scientific Instruments) was used for the stage heating and cooling. The mean value of Th and Tm of each sample is 173.5°C and −3.6°C for Sn-3, 192.5°C and −5.3°C for Mt-1, 230.0°C and −3.5°C for In-6, 216.6°C and −3.5°C for In-8, 204.2°C and −3.6°C for Bs-4, and 161.0°C and −3.0°C for Tn-6 (Fig. 3.12). The fluid isochores were estimated by the method of Bodnar and Vityk (1994), and the trapping temperature of the fluid were estimated by assuming the emplacement depth (Fig. 3.12). The emplacement depth is estimated from the contact metamorphism given to the surroundings by the intrusion of granitoids, 12 km for Inagawa Granodiorite (Miyake et al., 2016) and 8.5–9.0 km for Shinshiro Tonalite and Mitsuhashi Granodiorite (Endo and

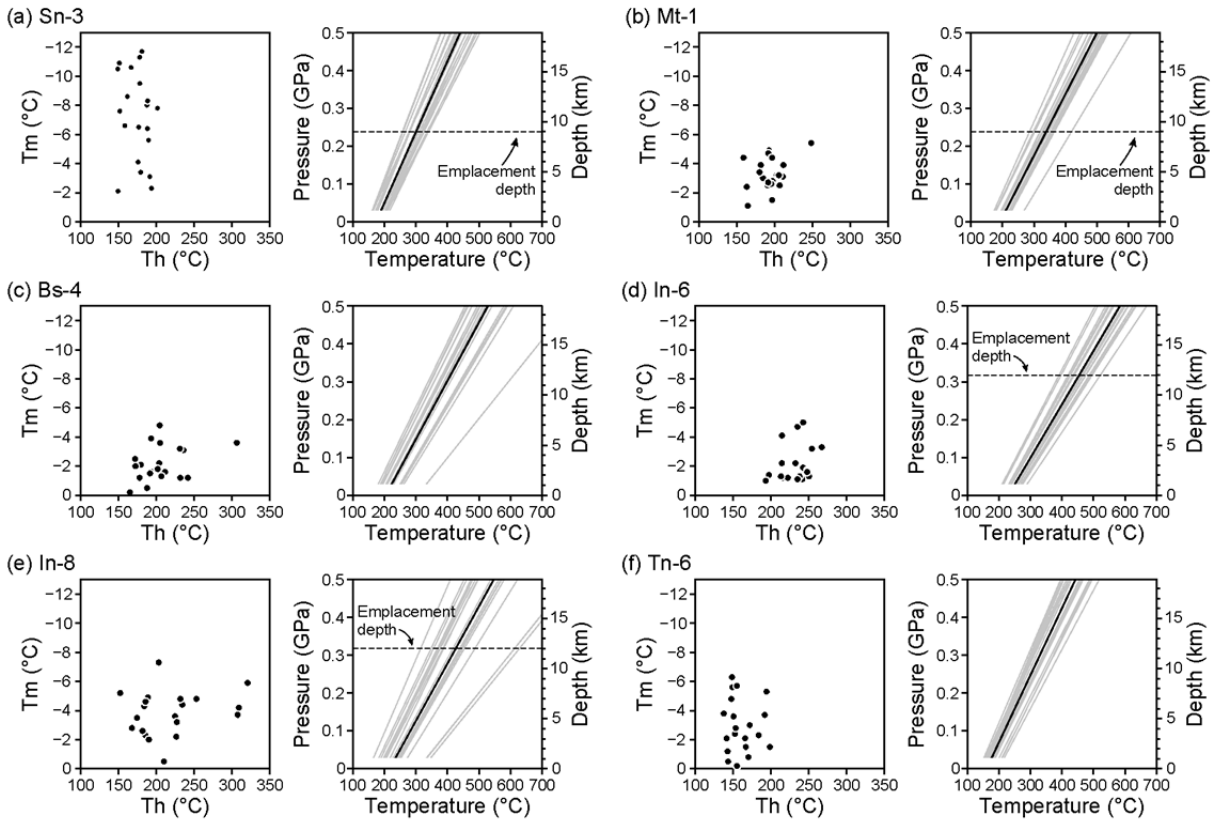

Fig. 3.12. Th (homogenization temperature) –Tm (melting temperature) diagrams (left) and pressure–temperature constraints for the trapping condition (right) of fluid inclusions consisting of HCs in quartz. Grey and black isochores indicate each data and their mean, respectively.

Yamasaki, 2013). Based on above conditions, the trapped temperatures of fluids are 260–340°C for Sn-4, 300–370°C for Mt-3, 410–500°C for In-6, 340–460°C for In-8. Assuming that the Busetsu Granite was also emplaced at the same depth (10 km) as these granitoids, the trapping temperatures of Bs-4 are estimated as 320–420°C. For the Toki Granite, the trapping temperature of 300–400°C is estimated with an intrusion depth of 3.5 km from the DH-15 core drilled by the Japan Atomic Energy Agency (Takagi et al., 2008). However, there is estimation that the intrusion depth of Toki Granite is 5–7 km from phase equilibrium diagram of Qtz–Or–Ab–H_2O system of felsic magma (Yamasaki and Umeda, 2012), the trapping temperature of fluid of Toki Granite is estimated to be 340–480°C based on this condition. The emplacement depth of the older Granitoids is considered to be 15–20 km in the Chugoku region (Takahashi, 1993) and Kii Peninsula (Nishiwaki and Okudaira, 2007) by the amount of Al in the hornblende. Assuming that emplacement depth of the Tenryukyo Granodiorite is 15–20 km, the trapped temperature of the fluid is estimated 320–520°C for Tn-6. Assuming that the host rock and fluid were in temperature equilibrium, the trapping period of the fluid can be estimated from the cooling curve of the host rock. The cooling curve of granitoids and fluid trapping period were estimated using the radiometric dating as shown in Fig. 2.4, where closure temperatures of the Pb system of monazite is 700°C (Suzuki et al., 1994a; Suzuki and

Adachi, 1998), the K–Ar system of hornblende is 500°C (Harrison, 1982) and the K–Ar system of biotite is 300°C (Dodson and McClelland-Brown, 1985). For Toki Granite, since the uplifting and cooling rates are different for each rock type (Yuguchi et al., 2011), only the radiometric age of biotite muscovite granite was used. Estimated formation age of HC is 69–67 Ma for Shinshiro Tonalite, 73–71 Ma for Mitsuhashi Granodiorite, 75–68 Ma for Inagawa Granodiorite, 73–71 Ma for Busetsu Granite, 74–69 Ma for Toki Granite, and 67–64 Ma for Tenryukyo Granodiorite.

3.7. Discussion

3.7.1. Effect of the observation bias correction

In previous studies, only universal-stage correction has been applied to correct the observation bias of HCs (e.g. Vollbrecht et al., 1991; Takeshita, 1995; Takagi et al., 2008, 2012; Sato and Takagi, 2010). In this study, the Terzaghi correction and the area correction were added to correct the observation bias. To examine the effect of these corrections, the contour diagrams with the variation of the applied correction are shown in Fig. 3.13. According to Fig. 3.13, Terzaghi correction and the universal-stage correction do not have a significant variation in the pattern of the contour diagrams. On the other hand, the area correction causes a large difference in the pattern and density of the contour diagrams. This is because the correction coefficient of the area correction is larger than the other two corrections. In the case of using a universal-stage to observe the HC, the correction value of Terzaghi correction and the universal-stage correction is limited to 1.23 and 2, respectively. On the other hand, there is no upper limit of the correction coefficient of area correction. In previous studies, the paleostress has been estimated on the basis of the maximum concentration orientation of the poles to HCs, and the maximum concentration orientation has been estimated by the observation from three orthogonal orientations with the universal-stage correction (e.g. Vollbrecht et al., 1991; Takagi et al., 2008, 2012; Sato and Takagi, 2010). However, the previous method cannot estimate the exact shape of the density distribution. Since the new dike method used in this study estimate the paleostress based on the variation of the orientation distribution of the HCs expressed in the shape of the density distribution, the area correction is indispensable to estimate an accurate orientation distribution of the HCs. In the case of Shinshiro Tonalite and Tenryukyo Granodiorite, about 100 HCs have been measured from each three orthogonal thin-sections based on the method of previous studies. However, if the performing the area correction, it is desirable to equalize the observation area of three orthogonal thin-sections in order to reduce the correction coefficient of area correction. Therefore, in the case of Busetsu Granite, Inagawa Granodiorite, Mitsuhashi

Granodiorite and Toki Granite, the method to equalize the observation area of three orthogonal thin-sections were devised by observing all of the quartz grains that can be observed in each thin-section.

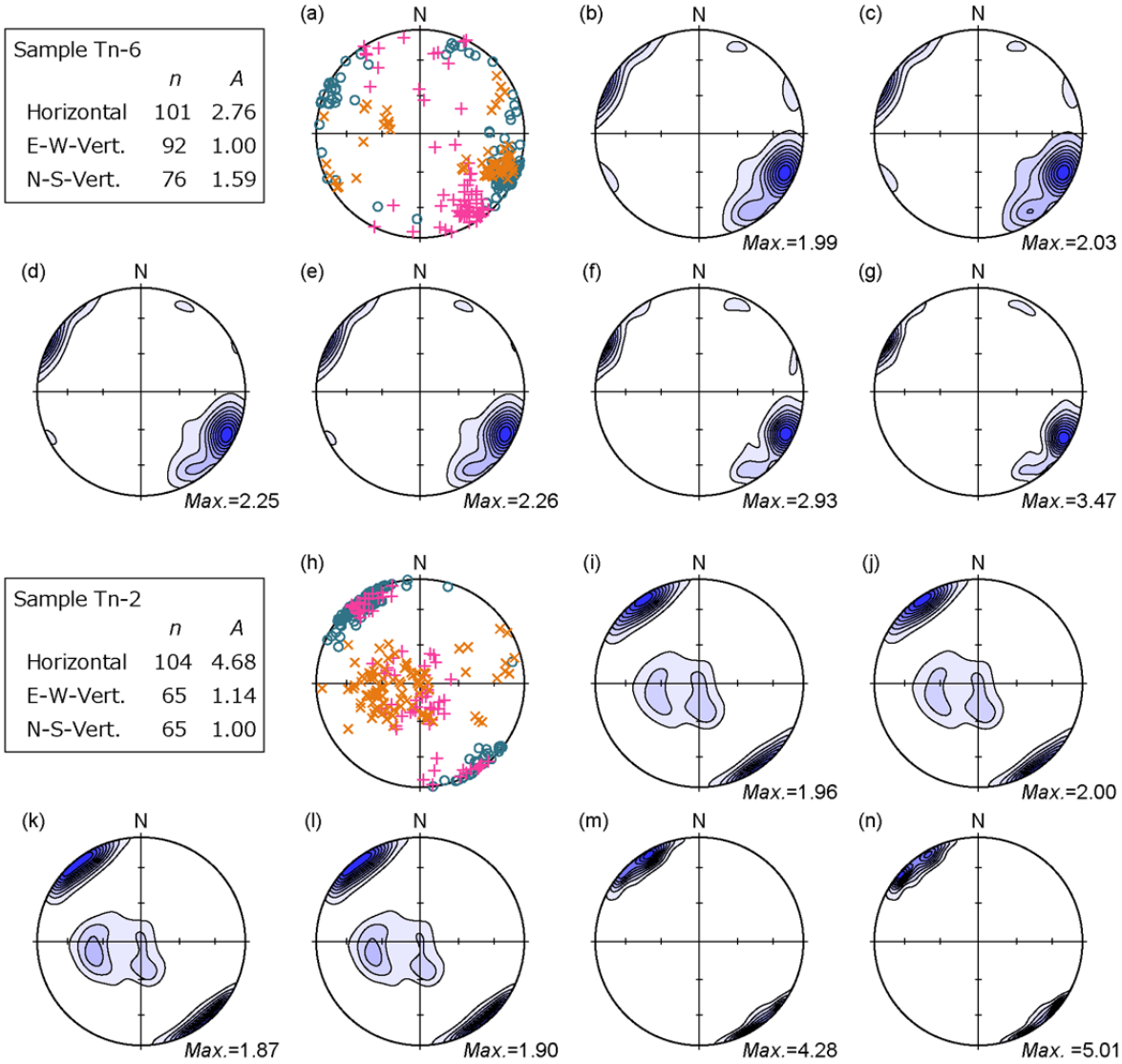

Fig. 3.13. Equal-area, lower hemisphere projections showing the poles and Gaussian contours with different corrections for samples Tn-6 and Tn-2. Gaussian contours with levels are 10 % to 90 % (in 10 % increments) of the peak maximum. *n* is number of cracks observed in each side of observation. *A* is the correction value of the area correction for each side of observation. *Max.* is the maximum density of the Gaussian contour. (a, h) Pole figure; pole symbols indicate the observation side for each HC measurement. (b, i) Uncorrected data. (c, j) Data corrected using a Terzaghi bias correction (Cor. T). (d, k) Data corrected using a universal-stage correction (Cor. U). (e, l) Data corrected using both Cor. T and Cor. U. (f, m) Data corrected using an area correction (Cor. A). (g, n) Data corrected using Cor. T, Cor. U, and Cor. A.

3.7.2. Relationship of the multiple clusters mixed in each sample

Several paleostresses sets have been detected from HCs in all samples (Fig. 3.8). The presence of such multiple stresses can be explained considering that it has experienced a plurality of different tectonic stress. On the other hand, even in a single tectonic stress, it is considered that HC can form perpendicular to σ_1 and σ_2 axes of tectonic stress by thermal

stress (Vollbrecht et al., 1991; Takeshita, 1995). On the basis of the experiments that caused the microcracks in the granite by heating and cooling under uniaxial stress conditions, forming the microcracks normal to the loading axis is suppressed (Ehara et al., 1986). These experiments show that the tectonic stresses constrain the orientation of HCs; whereas thermal stress is generated in order to heat expansion is hindered. Vollbrecht et al. (1991) considered that perpendicular clusters are formed by thermal stress orphaned by the release of elastic strain due to the occurrence of cracks. In previous studies, several perpendicular stresses have been estimated based on the orientation distribution of HCs, and these stresses are considered that formed by thermal stress described above (e.g. Takagi et al., 2008, 2012). However, this claim requires a re-examination by the following reasons. In previous studies, *k*-means method (Pecher, 1986) has been used to detect clusters from the data. Clustering of directional data by *k*-means method is estimating the membership of the data and cluster center as to minimize the sum of the angular difference between the cluster center and each datum. Although the *k*-means method is easy to calculate, there are four problems mentioned below: 1) Assume the existence of a circular shape cluster on the stereo net, not captured well the elliptical or girdle shape cluster, 2) It may not be possible to separate the cluster with a different concentration, 3) The center of the cluster is likely to show an orthogonal relationship to each other, 4) Not be able to separate the clusters that have a close orientation of maximum concentration. Moreover, although the *k*-means method is necessary to specify the number of clusters *k*, the statistical basis for estimating the *k* (e.g. Gap statistics; Tibshirani et al., 2001) is not described in previous studies. The clustering results from the mixed Bingham distribution model and the *k*-means method applying a sample Tn-4 are compared to examine the variations in the result of stress analysis based on the difference of the clustering method (Fig. 3.14). Using the mixed Bingham model, detected two of the three

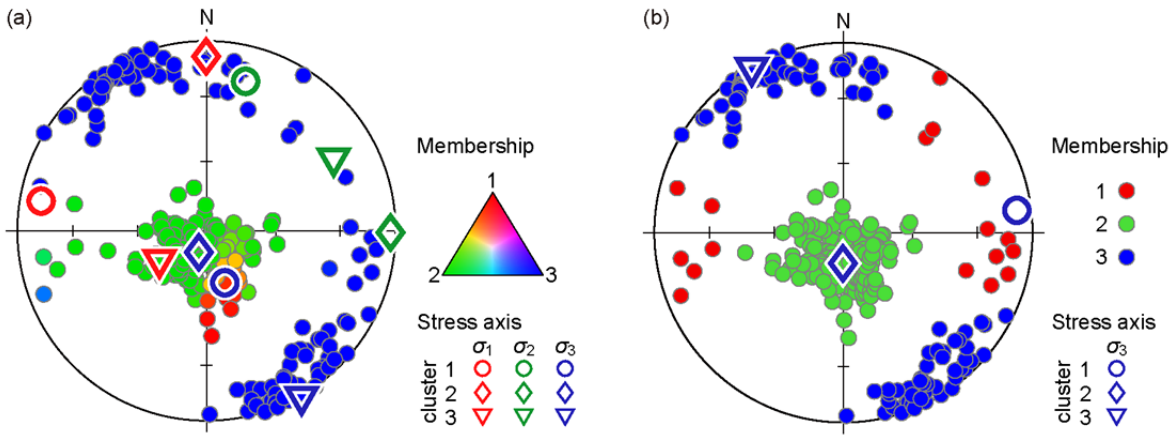

Fig. 3.14. Equal-area, lower hemisphere projections showing principal stress axes orientations estimated by clustering of the data for sample Tn-4. (a) Mixed Bingham distribution model clustering. (b) *k*-means method clustering.

σ_3 axes are close and show a high angle plunge. On the other hand, using the *k*-means method, detected three σ_3 axes have trends 331.3° and plunges 0.4°, trends 82.2° and plunges 8.0° and trends 180.0° and plunges 77.5°, respectively. Each σ_3 axes estimated by the *k*-means method is showing an orthogonal relationship, the orthogonal relationship of paleostress in previous studies might have been affected by clustering method. In this study, many detected paleostresses from each sample does not show an orthogonal relationship of σ_3 axes. Therefore, HC distribution cannot be explained only the effect of the thermal stress described above, considered granite experienced several paleostresses by temporal and spatial differences. Further studies are needed in order to refer to the relationship of multiple paleostresses in each sample.

3.7.3. Variation of paleostress in each region

Prominent stress detected from each sample show a variation in each region. In this study, 1) the variation of paleostress along the transect parallel to the MTL from Shinshiro Tonalite and Tenryukyo Granodiorite; and 2) the variation of paleostress along the transect normal to the MTL from Shinshiro Tonalite, Busetsu Granite, Mitsuhashi Granodiorite, Inagawa Granodiorite and Toki Granite are discussed.

First, the paleostress along the transect parallel to the MTL are examined. Sampling locations are distributed in the range of about 80 km parallel to the MTL. Distance from the orthogonal direction from the MTL to Shinshiro Tonalite and Tenryukyo Granodiorite are 2.2–6.4 km and 2.1–4.5 km, respectively. Prominent stress detected from Shinshiro Tonalite shows that σ_3 axis trends NNW–SSE with low angle plunges. Except for the sample Sn-2, σ_2 axis trends WSW with low angle plunges, and σ_1 axis trends N and high angle plunges. For Tenryukyo Granodiorite, except for sample Tn-4, prominent stress shows that σ_3 axis trends NW–SE with low angle plunges, and σ_2 and σ_1 axes are distributed on the great circle normal to the σ_3 axis. Since the detected prominent paleostress shows a similar orientation over the wide area of each granitic body, this paleostress is considered as a regional tectonic stress. Since the orientation of σ_3 axis trends normal to the strike of the MTL with a low angle plunge, the tensile stress field is considered to have been developed with the σ_3 axis oriented normal to strike of the MTL within 2–7 km from the MT in 75–60 Ma. However, it is difficult to explain the distributions of σ_2 and σ_1 axes in a simple tensile stress field model, more presence of the local stresses is suggested.

Second, the paleostress along the transect normal to the MTL are examined. Sampling locations are distributed in the range of 2–60 km from the MTL. From Fig. 3.11, σ_2 and σ_1 axes show unrelated variation the distance from the MTL, however, σ_3 axis shows a tendency

to rotate counterclockwise with increasing the distance from the MTL. To confirm this relationship, the correlation between the orientation of principal stress and distance from the MTL are examined. Directional data are roughly classified into vectorial data or axial data and circular data or spherical data (e.g. Mardia and Jupp, 1999): principal stress axis is classified to the spherical axial data. Since such a directional data has the feature that circulates (e.g. 0° = 360°), it is necessary to use a method developed for the directional data to estimating a correlation between linear data (no circulate data) such as distance. For the spherical data, the method to estimate the correlation between vectorial data and linear data is developed (Jupp and Mardia, 1980), however, to estimate the correlation between axial data and linear data is not known. On the other hand, for the circular data, the methods to estimate the correlation are developed for both vectorial and axial data (Mardia, 1976). Therefore, the circular–linear correction (Mardia, 1976) are used to evaluate the orientation of the principal stress axis with respect to the distances from the MTL. In order to apply this method, the dimension is reduced by the principal component analysis (Fig. 3.15a, b, Table 3.2). The circular–linear correlation is calculated by using circular data projected on the optimal great circle obtained by principal component analysis. The reference orientation of projected circular data was set to the mean orientation; however, correlations will not change by the reference orientation. The circular–linear parametric correlation,$R^2_{\theta x}[0,1]$, and non-parametric correlation, $D_{\theta x}[0,1]$, for σ_1, σ_2 and σ_3 axes were calculated 0.09, 0.12 and 0.48, and 0.06, 0.09 and 0.43, respectively (Fig. 3.15c, Table 3.2). The greatest value of a correlation coefficient indicates the stronger relationship. These correlation coefficients indicate that the orientations of σ_2 and σ_1 axes are uncorrelated and orientation of σ_3 axis is correlated between the distances from the MTL. Effect of dimension reduction by principal component analysis can be evaluated by the cumulative contribution ratio of the second principal component, as the value is close to 100 % indicating that the effect of dimension reduction is small. For σ_3 axis, projected two-dimensional data by principal component analysis may explain the 94.5 % of the data of the three-dimensional complete data. Even considering the loss of data due to dimension reduction, there is a weak correlation between the orientation of σ_3 axis and distance from the MTL. The orientation of σ_3 axis is normal to the strike of the MTL close to the MTL and almost parallel to the strike of the MTL in regions away from the MTL. Moreover, the orientation of σ_3 axis rotates counterclockwise with increasing the distance from the MTL.

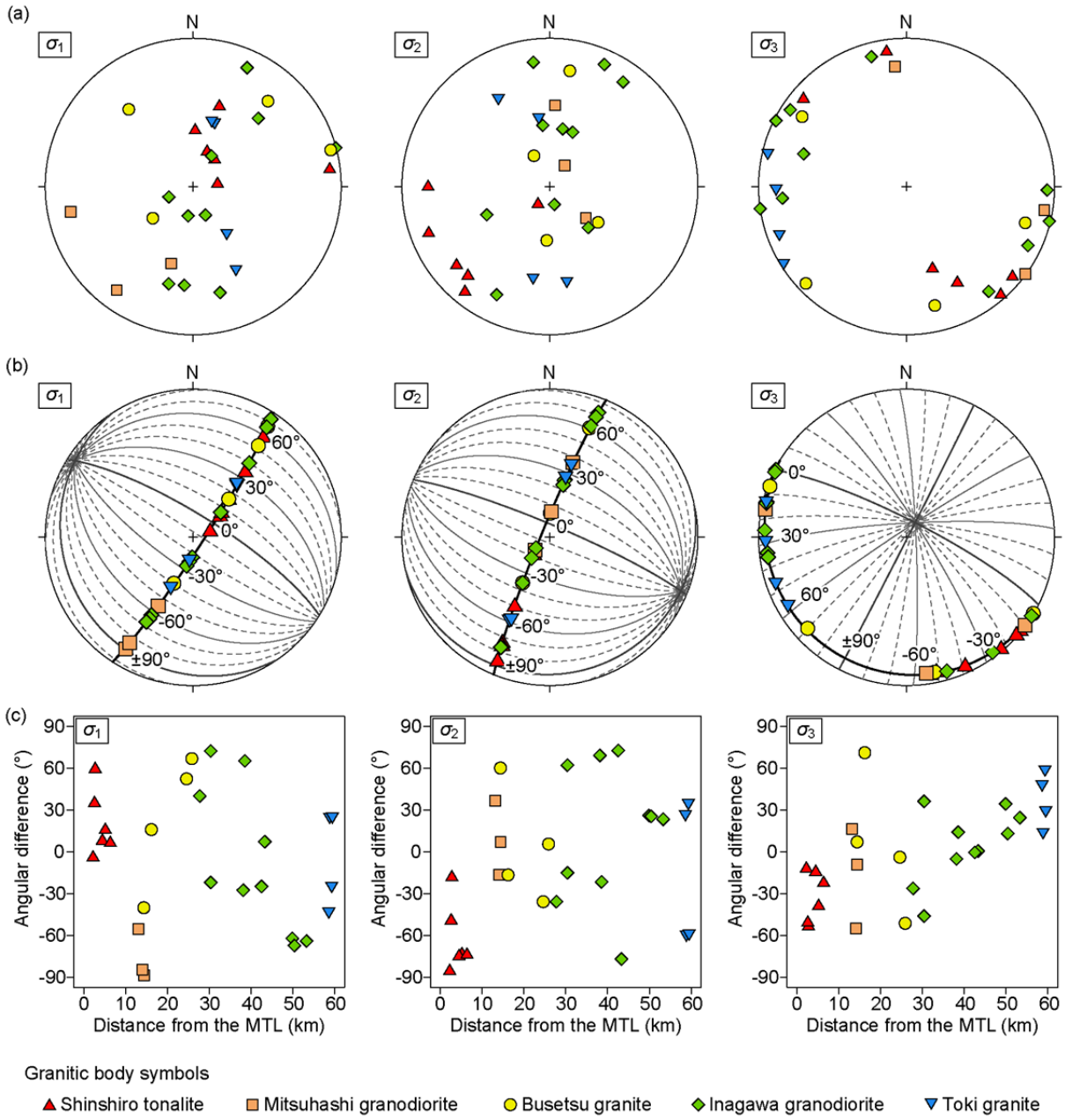

Fig. 3.15. (a) Equal-area, lower hemisphere projections showing principal stress axes from prominent stress. (b) Best-fit great circle (thick line) from principal component analysis and projections of principal stress axes from prominent stress projected onto the best-fit great circle, lower-hemisphere, equal-area projections. (c) The relationship between angular differences of stress axes projected onto the best-fit great circles and distance from the MTL.

Table 3.2. The results of principal component analysis and correlation between angular differences of stress axes projected onto the best-fit great circles and distance from the MTL.

Stress axis	Pole of best fit great circle (Trend / Plunge [°])	Eigenvalue			Accumulated proportion [%]			Correlation coefficient	
		1st	2nd	3rd	1st	2nd	3rd	$R^2_{\theta x}$	$D_{\theta x}$
σ_1	320.1 / 32.7	10.3	7.3	3.3	49.1	84.1	100.0	0.09	0.06
σ_2	231.8 / 61.6	9.7	8.4	3.0	46.1	85.9	100.0	0.12	0.09
σ_3	41.3 / 24.4	14.5	5.3	1.2	69.0	94.5	100.0	0.48	0.43

Chapter 4: Determination of the stress conditions of the Asuke Shear Zone

4.1. Introduction

The Asuke Shear Zone (ASZ) is a shear zone developed in the Inagawa Granodiorite and is considered to record the deformation conditions in the cooling process of the Inagawa Granodiorite. Sakamaki et al. (2006) considered that the deformation along the ASZ took place in the ductile-to-brittle transition regime based on the occurrence of the fault rocks, shear sense, and microscopic observations. However, more detailed deformation conditions such as differential stress and orientation of paleostress have not been clarified. In this study, new data on 1) the deformational conditions of the ductile-to-brittle transition regime, as inferred from lattice preferred orientations (LPOs) and the grain size of dynamically recrystallized quartz in the mylonitized pseudotachylytes; and 2) that, as inferred from the deformation twins (*e*-twins) of calcite in the amygdules of the pseudotachylytes are presented.

4.2. Geological settings of the Asuke shear Zone

The ASZ transects the Inagawa Granodiorite in the Ryoke Belt ~30 km NW of the Median Tectonic Line (MTL), and it extends NE–SW for ~14 km and is several tens to hundreds of meters wide (Fig. 4.1a, b). The ASZ comprises small-scale shear zones with thicknesses of several millimeters to more than ten centimeters and left-stepping *en échelon* arrangements (Sakamaki et al., 2006). Cataclasites are observed along the entire length of the ASZ, and pseudotachylytes and cataclasites coexist everywhere except in the northern segment; pseudotachylytes, cataclasites, and mylonites coexist only in the central segment from Korankei to Oshima (Fig. 4.1c). Kinematic indicators and stretching lineations in the mylonites, foliated cataclasites, and foliated pseudotachylytes indicate a sinistral–normal movement (Sakamaki et al., 2006). Pseudotachylyte fault veins were generated mainly along the P-shear surfaces, whereas cataclasites formed along the Y- and R_1-shear surfaces. Therefore, frictional fusion occurred under a relatively transpressional context (the P-shears) on the mesoscopic scale, but also in a transtensional (sinistral–normal shear) context on the macroscopic scale (Sakamaki et al., 2006). The coexistence of mylonitized pseudotachylytes and crushed mylonites suggests that the ASZ formed within the ductile-to-brittle transition regime. The reactivation of cataclasites at shallower crustal depths, if at all, did not modify the pre-existing deformational fabrics (Sakamaki et al., 2006).

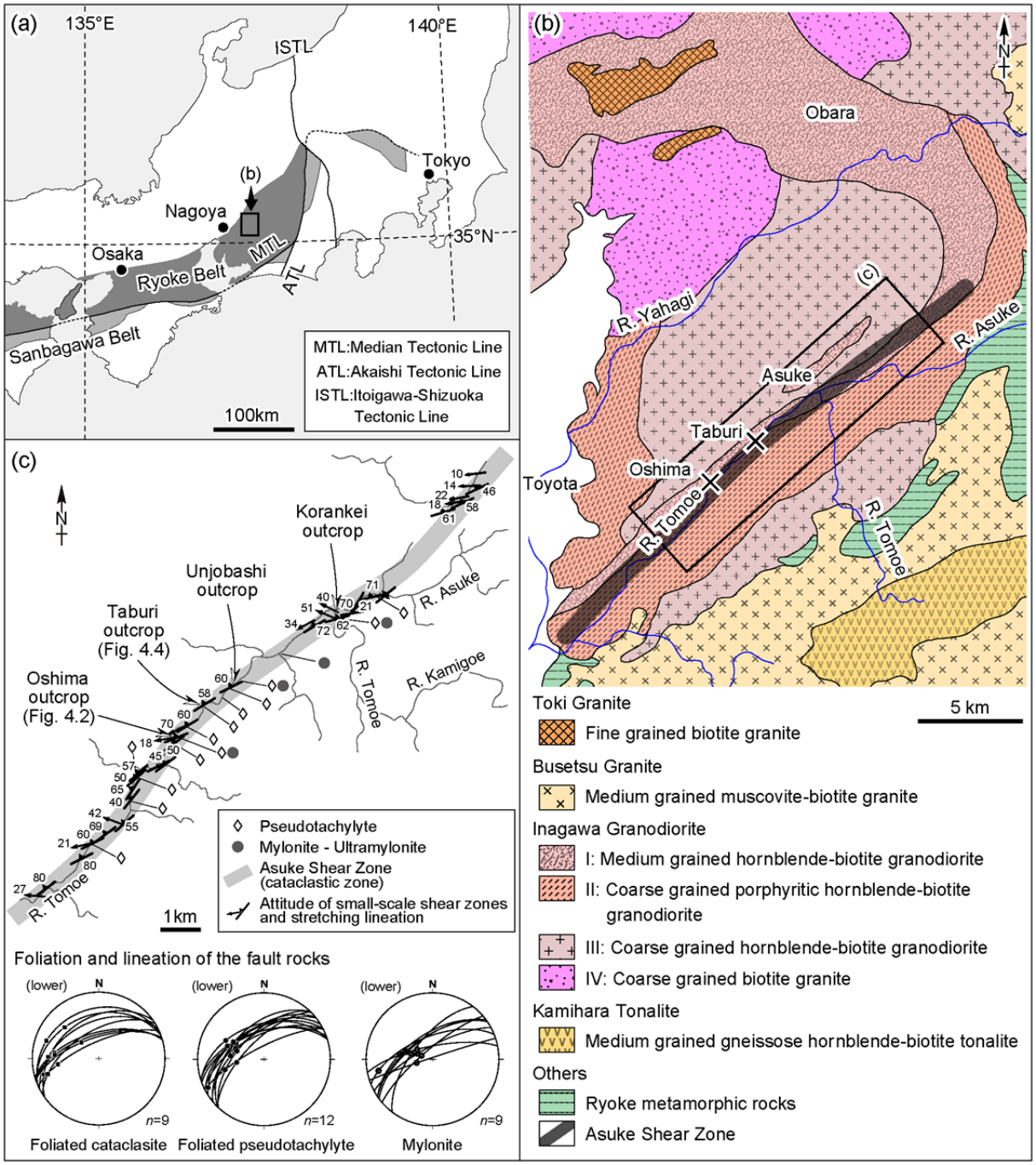

Fig. 4.1. Geological map of the Asuke Shear Zone. (a) Index map showing the location of the study area. (b) Geological map of the Asuke Shear Zone and surrounding Ryoke granitoids, modified after Nakai (1976), Ishihara and Chappell (2007) and Sakamaki et al. (2006). (c) Distribution of various fault rocks and orientations of small-scale shear zones constituting the central part of the Asuke Shear Zone (lower-hemisphere, equal-area projection.), simplified after Sakamaki et al. (2006).

4.3. Petrography of fault rocks

4.3.1. Mylonitized pseudotachylyte from the Oshima outcrop

Mylonitized pseudotachylytes with a preferred orientation of crushed fragments occur at Korankei, Unjobashi, and Oshima (Fig. 4.1c). Pseudotachylytes, cataclasites, mylonites, and mylonitized pseudotachylytes can be observed in the Oshima outcrop (Fig. 4.2). Small

shear veins with a mean thickness of several millimeters to 3 cm, and striking NE–SW to ENE–WSW and dipping 50–70° to the NW are developed in the Oshima outcrop (Sakamaki et al., 2006). A mylonitized pseudotachylyte sample is used to estimate the stress conditions of plastic deformation after brittle deformation (Fig. 4.3a). The long side of the analyzed thin section is parallel to the lineation, which approximates the principal strain axis X (elongation), and the short side is normal to the foliation, which approximates Z (shortening). A zone of relatively high strain (hereinafter, the shear-zone center) has developed around the fault vein of the foliated pseudotachylyte (Fig. 4.3b). Sinistral shear is indicated by the relative orientations of the fault and stretching lineations, which can be defined by the elongation of the deformed quartz aggregates and single quartz crystals (Fig. 4.3c, d), S–C'-type shear bands (Fig. 4.3c), and fragments with asymmetric pressure shadows. Dynamically recrystallized quartz aggregates can be observed not only in the host rock, but also in the fault vein and injection vein of the pseudotachylyte. Fig. 4.3e–j shows the recrystallized quartz aggregates in the shear-zone center (Fig. 4.3e–g), fragments in the injection vein of pseudotachylyte (Fig. 4.3h, i), and the deformed host rock located away from the shear-zone center (Fig. 4.3j). The shapes of the quartz aggregates in all domains are serrate–interlobate. The stress conditions of deformation were estimated by analyzing the LPO pattern and grain size of recrystallized quartz in six analysis domains (Fig. 4.3a, e–j).

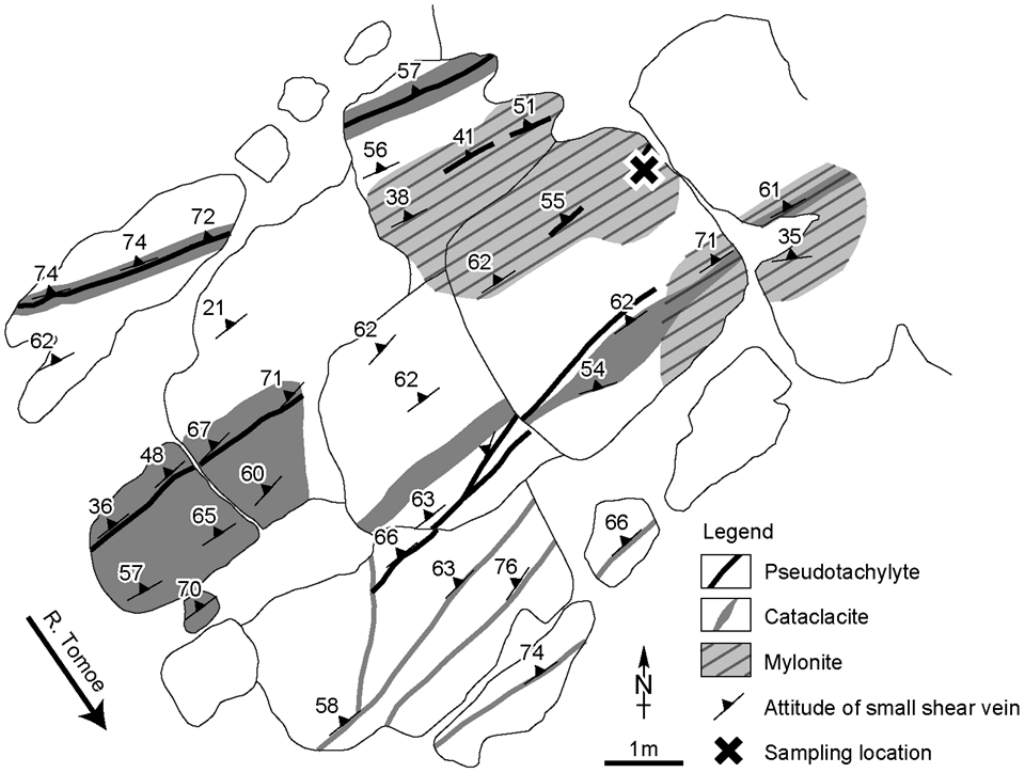

Fig. 4.2. Map showing occurrence and attitude of fault rocks in the Oshima outcrop. Original outcrop map was provided by Mr. Hideaki Sakamaki.

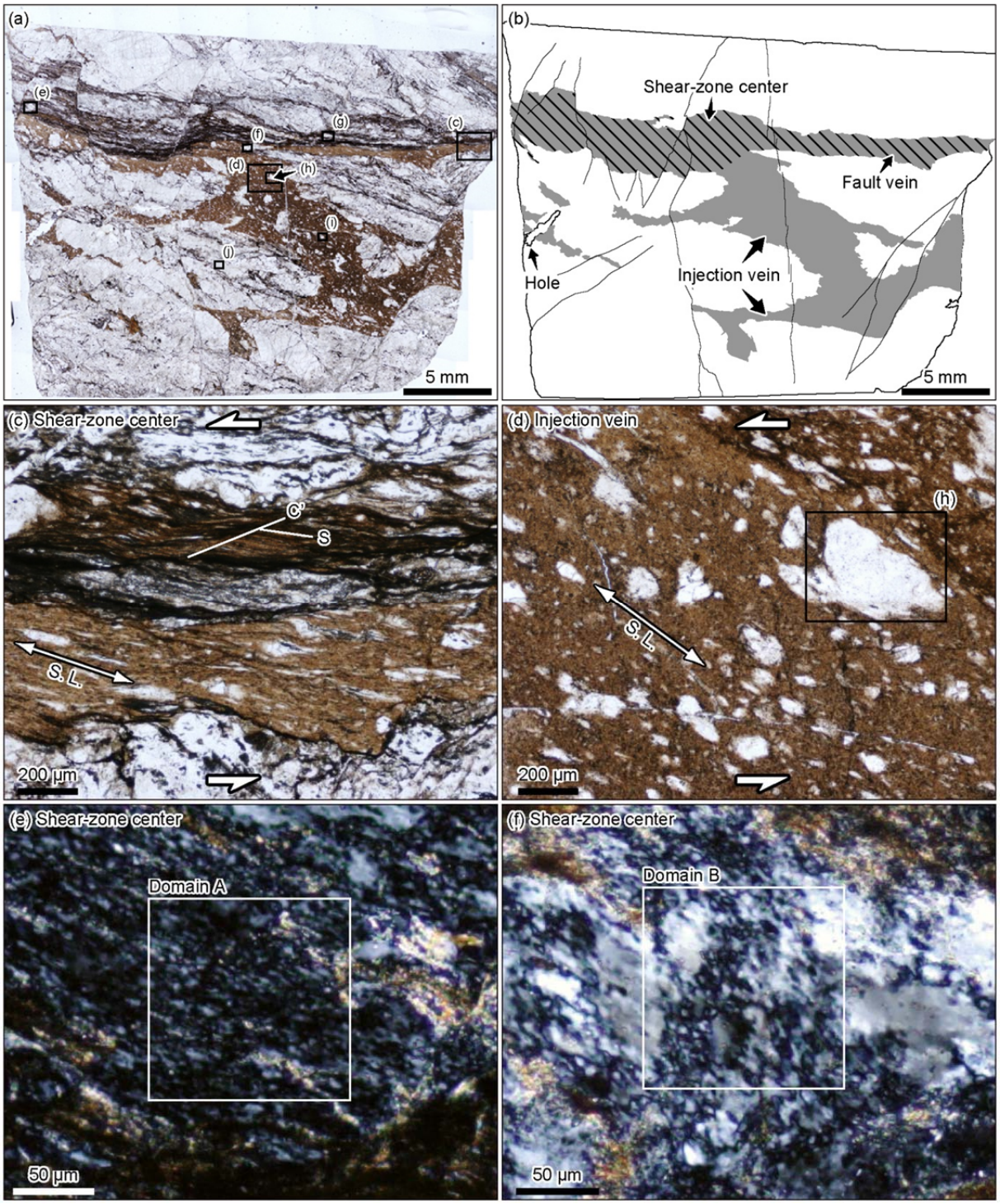

Fig. 4.3. Occurrence of mylonitized pseudotachylyte from the Oshima outcrop. (a, b) Photomicrograph (a: PPL) and sketch (b) of the mylonitized pseudotachylyte. (b, c) Close-up view of the shear-zone center (c) and injection vein (d) (PPL). Sheared and stretched fragments, and S–C'-type shear bands in (c) indicate sinistral shear. (e–j) Recrystallized quartz grains in the shear-zone center (e–g), in a fragment in the injection vein (h, i), and in the deformed host rock (j) (XPL). The squares of A–F in the pictures e–j show the areas analyzed by the SEM-EBSD. XPL, crossed polarized light; PPL, plane polarized light; S.L., stretching lineation.

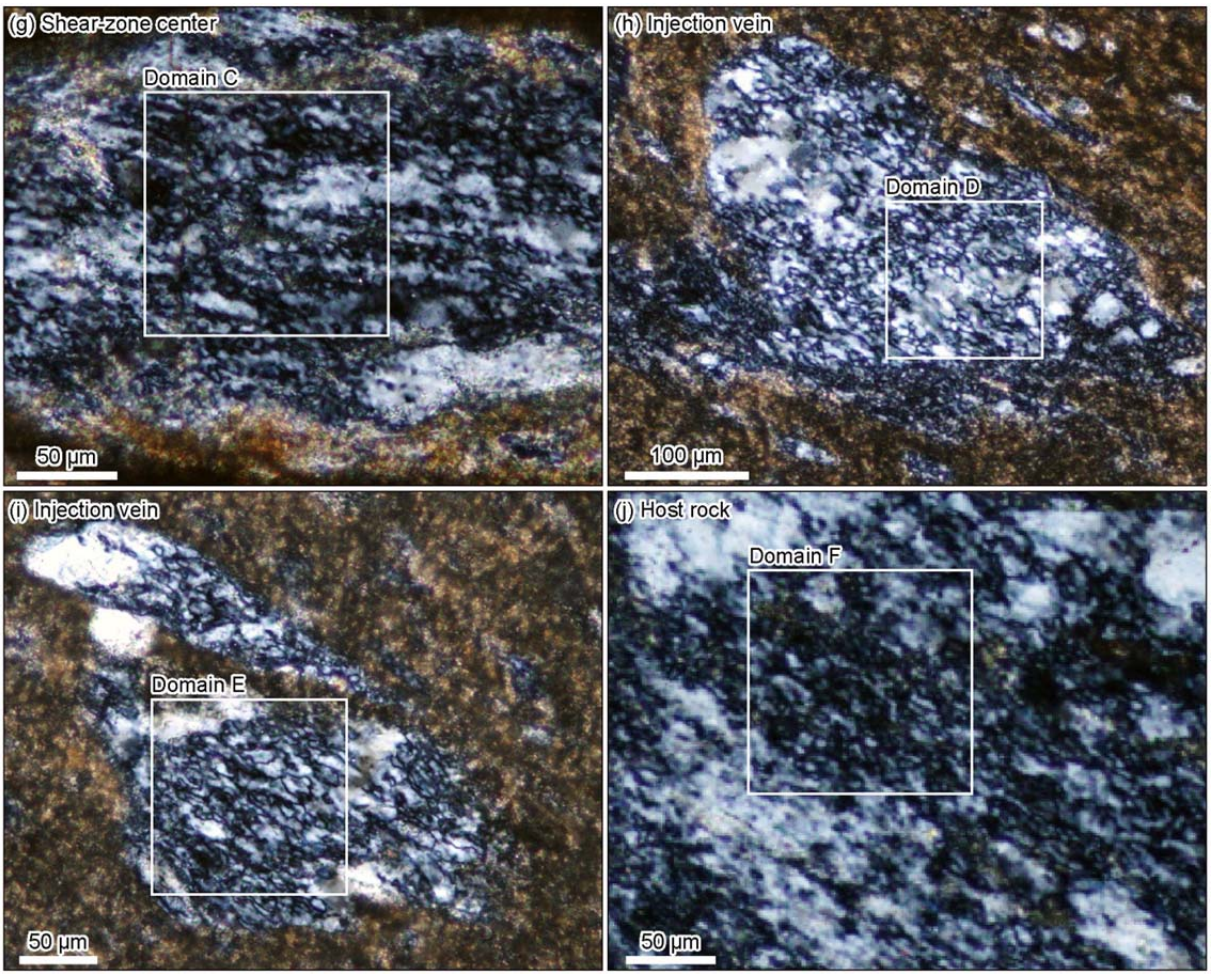

Fig. 4.3. Continued.

4.3.2. Pseudotachylyte from the Taburi outcrop

Pseudotachylytes and cataclasites can be observed in the Taburi outcrop (Fig. 4.4). In particular, an exceptionally thick pool of pseudotachylyte was observed (Fig. 4.5a). Small shear veins with a mean thickness of several millimeters to 3 cm, and striking NE–SW to ENE–WSW and dipping 40–70° to the NW are developed in the Taburi outcrop (Sakamaki et

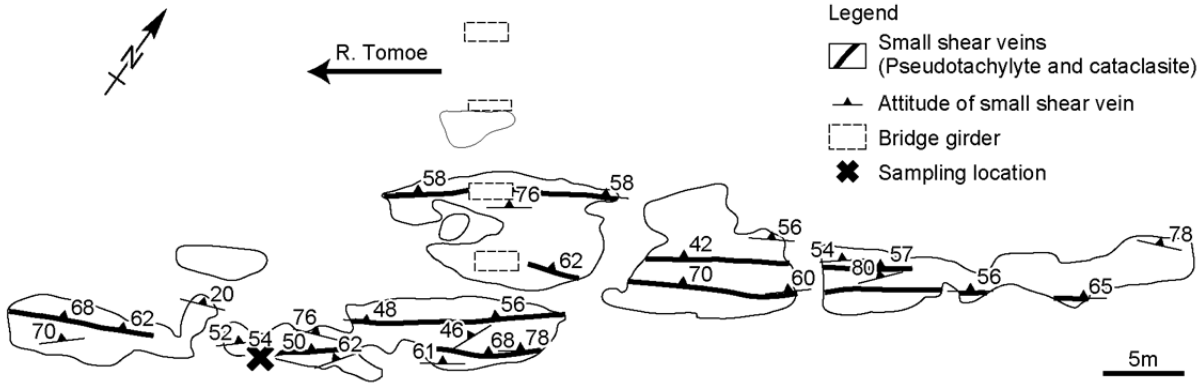

Fig. 4.4. Outcrop map showing occurrence and attitude of fault rocks in the Taburi outcrop, after Sakamaki et al. (2006).

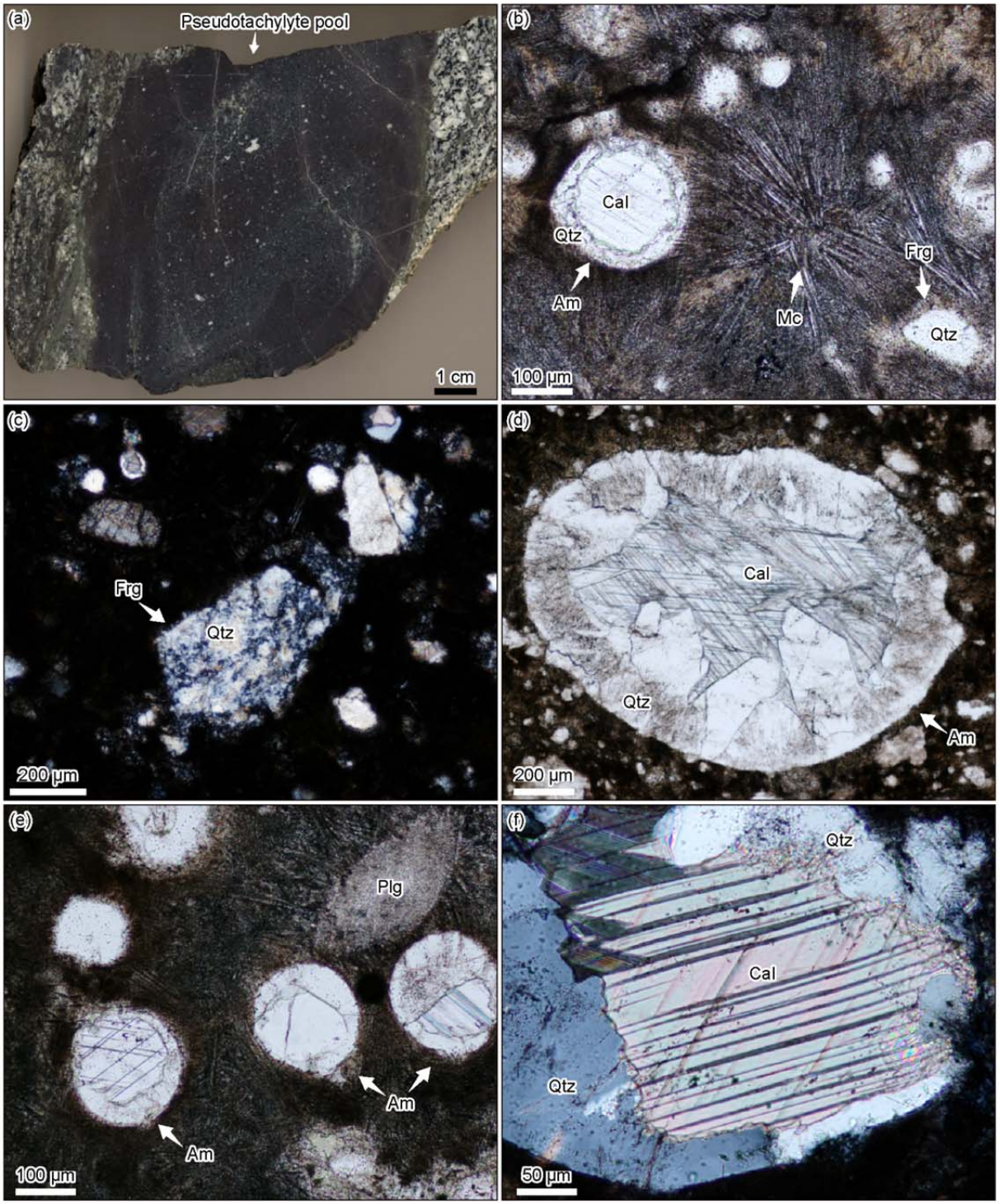

Fig. 4.5. (a) Photograph of a polished slab and (b–f) photomicrographs of the thickest (11 cm in diameter) pseudotachylyte from the Taburi outcrop. (b) Evidence of melt and quench textures in the thickest pseucotachylyte; amygdule filled with quartz mantle and calcite core, spherulitic microlites, and rounded quartz fragments (Plg) (PPL). (c) Mylonitized quartz fragment (XPL). (d) Largest amygdule (1.45 mm in diameter) (PPL). (e) Calcite cements in amygdules showing varying densities and orientations of twins and rounded altered plagioclase fragments (PPL). (f) Thick straight twins (type II) in calcite cement in an amygdule (XPL). Am, amygdule; Mc, microlite; Frg, fragment; Qtz, quartz; Cal, calcite.

al., 2006). The exceptionally thick pseudotachylyte (Fig. 4.5a) was used for the analysis because it is necessary to observe many amygdules for the stress inversion method, as mentioned later. The pool of pseudotachylyte was probably formed by melted material

flowing into a pull-apart segment during sinistral movement (Sakamaki et al., 2006). Similar phenomena have been reported by Techmer et al. (1992) and Ferré et al. (2014). This thick pseudotachylyte pool has been used for zircon fission-track dating (Murakami et al., 2006a). Melting and quenching textures such as amygdules, microlites, spherulitic microlites, and rounded quartz fragments with embayment textures can be observed, especially in this thick pseudotachylyte pool (Fig. 4.5b). Fragments of dynamically recrystallized quartz aggregates can be observed (Fig. 4.5c).

Altogether, 11,092 pieces of amygdules have been observed in specimens of this thick pseudotachylyte pool. The outlines of these amygdules were traced, and the particle diameter and aspect ratio of an ellipse fitted are calculated by the image analysis software Image J. The mean diameter and aspect ratio were 105 μm and 1.19, respectively. The maximum diameter of the major axis was 1.45 mm (Fig. 4.5d). Some amygdules have core–mantle structures with calcite at the core and quartz at the mantle. Hematite grains can also occasionally be observed in the mantles. Amygdules with such core–mantle structures amounted to 2535 (22.9%) of the 11,092 pieces; the other amygdules were filled only with quartz. In the case where, the diameter of an amygdule was several hundred microns or less, most of the mantle quartz was a single crystal, but for larger diameters, the mantle quartz was polycrystalline. Core calcite mostly comprised a single crystal, regardless of the diameter of the amygdule. The calcite commonly displayed deformation twinning with varying twin densities and twin attitudes (Fig. 4.5e). Using the classification of calcite deformation twins provided by Burkhard (1993), most calcites contained thin (<1 μm) straight twins (type I) and subsidiary numbers of thick (>1 μm) straight twins (type II; Fig. 4.5f).

4.4. Quartz LPO analysis

4.4.1. Principles

The LPOs of polycrystalline quartz are considered to reflect the deformation mechanism. Grain-size-insensitive (GSI) creep (dislocation creep) produces a distinct LPO pattern, whereas grain-size-sensitive (GSS) creep, including grain-boundary sliding (GBS) and diffusion creep, does not or else it produces very weak LPO (Boullier and Gueguen, 1975; Rutter and Brodie, 2004; Hiraga et al., 2010; Kilian et al., 2011). Furthermore, in the case of dislocation creep, LPO patterns can be used to estimate the activated slip system and the deformation temperature (Bouchez, 1977; Takeshita and Wenk, 1988; Sakakibara, 1996; Heilbronner and Tullis, 2006). The grain size of recrystallized quartz is a function of differential stress and it has been used as a paleopiezometer (Twiss, 1977; Stipp and Tullis, 2003). By obtaining the deformation temperature and differential stress, it is possible to

calculate the strain rate using the flow laws of minerals with assuming the values for other parameters such as water content (Okudaira and Shigematsu, 2012). In addition, it has been reported that the differential stress and the strain rate can be estimated from coexisting activated deformation mechanisms determined from microstructures (Okudaira and Shigematsu, 2012).

4.4.2. Analytical methods

The LPO patterns of deformed polycrystalline quartz in mylonitized pseudotachylyte from the Oshima outcrop have been measured using electron backscatter diffraction (EBSD) with a scanning electron microscope (the SEM-EBSD method). The SEM (Hitachi S-3400N at Waseda University) operating and sample conditions were as follows: accelerating voltage 20 kV, working distance 30 mm, specimen tilted by 70°, low-vacuum mode (30 Pa), and uncoated samples. The HKL Nordlys detector (Oxford Instruments) was used to detect the electron backscatter patterns (EBSP), and the HKL Channel 5 software (Oxford Instruments) was used to index the EBSP. EBSD mapping was performed lengthwise and crosswise with 250 points at 0.5 μm intervals (125 × 125 μm), and a band contrast map magnified by 2 times (500 × 500 pixels) was used to create the grain boundary map. These points with relatively low band contrast were treated as candidates for the grain boundary. The critical misorientation angle for the quartz grain boundary is generally >10° (White, 1977). Thereafter, candidates with a misorientation angle >10° were treated as a grain boundary. Tracing a grain boundary was undertaken using the 1-pixel pen tool in Adobe Photoshop. After determining the grain boundaries, the crystallographic orientation of one point in each grain was determined as a representative crystallographic orientation of the grain. Thereafter, the *c*-axis LPO pattern was determined by visual inspection, and the randomness of the LPO was evaluated by the M-index (Skemer et al., 2005). The index varies between 0 and 1, and it is calculated based on the distribution of misorientation angles from the complete set of all possible grain pairs; an M-index value close to 0 means the LPO distribution is random. The grain size and aspect ratio of the quartz grains were determined following Stipp et al. (2002), using the image analysis software Image J. The long (a) and short (b) axes of the best-fit ellipse for grain shape were determined using the Analyze tool in Image J, and the geometric mean ($d = \sqrt{a \times b}$) was used as the two-dimensional size of individual grains. The grain size distribution of dynamically recrystallized quartz grains commonly presents a lognormal distribution (Ranalli, 1984). In this study, the mean grain size in each domain was calculated as the exponential of the arithmetic mean of the log of individual grain size; i.e., the geometric mean grain size. Grains that were transected by the edge of the analysis area and

that did not have many indexed points were excluded from the indexing process.

4.4.3. Results

The Euler map, band contrast map, grain boundary map, two-dimensional grain size distribution, and pole figures for the *c*-axis [0001] and *a*-axis <11-20> of the quartz grains are shown in Fig. 4.6. The parameters of the distance from the shear-zone center, number of grains, grain sizes, aspect ratio, and values of the M-index in the analyzed domains are listed in Table 4.1. Domains A, B, and C (Fig. 4.3e–g), located in the shear-zone center, have mean grain sizes that vary from 6.40 to 6.95 μm (average: 6.61 μm), mean aspect ratios varying from 1.59 to 2.00 (average: 1.73), M-index values that range from 0.093 to 0.215, and *c*-axis LPO patterns that show Z-axis concentrations (Z-maximum). Domain D (Fig. 4.3h), located in the injection vein of the pseudotachylyte 1.52 mm from the shear-zone center, has a mean grain size of 7.69 μm, a mean aspect ratio of 1.81, M-index value of 0.054, and *c*-axis LPO pattern that shows Z-maximum. Domain E (Fig. 4.3i), located in the injection vein of the pseudotachylyte 4.56 mm from the shear-zone center, has a mean grain size of 6.95 μm, a mean aspect ratio of 1.83, M-index value of 0.031, and *c*-axis LPO pattern that is characterized by a weak XY girdle. Domain F (Fig. 4.3j), located in the host rock 6.49 mm from the shear-zone center, has a mean grain size of 7.51 μm, a mean aspect ratio of 1.80, M-index value of 0.018, and *c*-axes that are relatively randomly oriented. Thus, domains A–D, located in and close (1.5 mm) to the shear-zone center, have Z-maximum LPO patterns and relatively large M-index values, whereas domains E and F, located away (>4.5 mm) from the shear-zone center, have weak and random LPO patterns and relatively small M-index values. The mean grain size shows relatively small variations in domains located in the shear-zone center, whereas the aspect ratio does not show any clear difference between each domain. Anhedral-shaped subgrains are observed in every domain, and the shape of the quartz aggregates is serrate–interlobate. Based on these results, the six domains were classified into three domain sets according to their location: (1) domains A–C, located at the shear-zone center, show Z-maximum LPO patterns; (2) domain D, located at the injection vein of mylonitized pseudotachylyte, close to the shear-zone center (within 1.5 mm), also shows a Z-maximum LPO pattern; or (3) domains E and F, located far from the shear-zone center (>4.5 mm), show a weak XY girdle and a relatively random orientation.

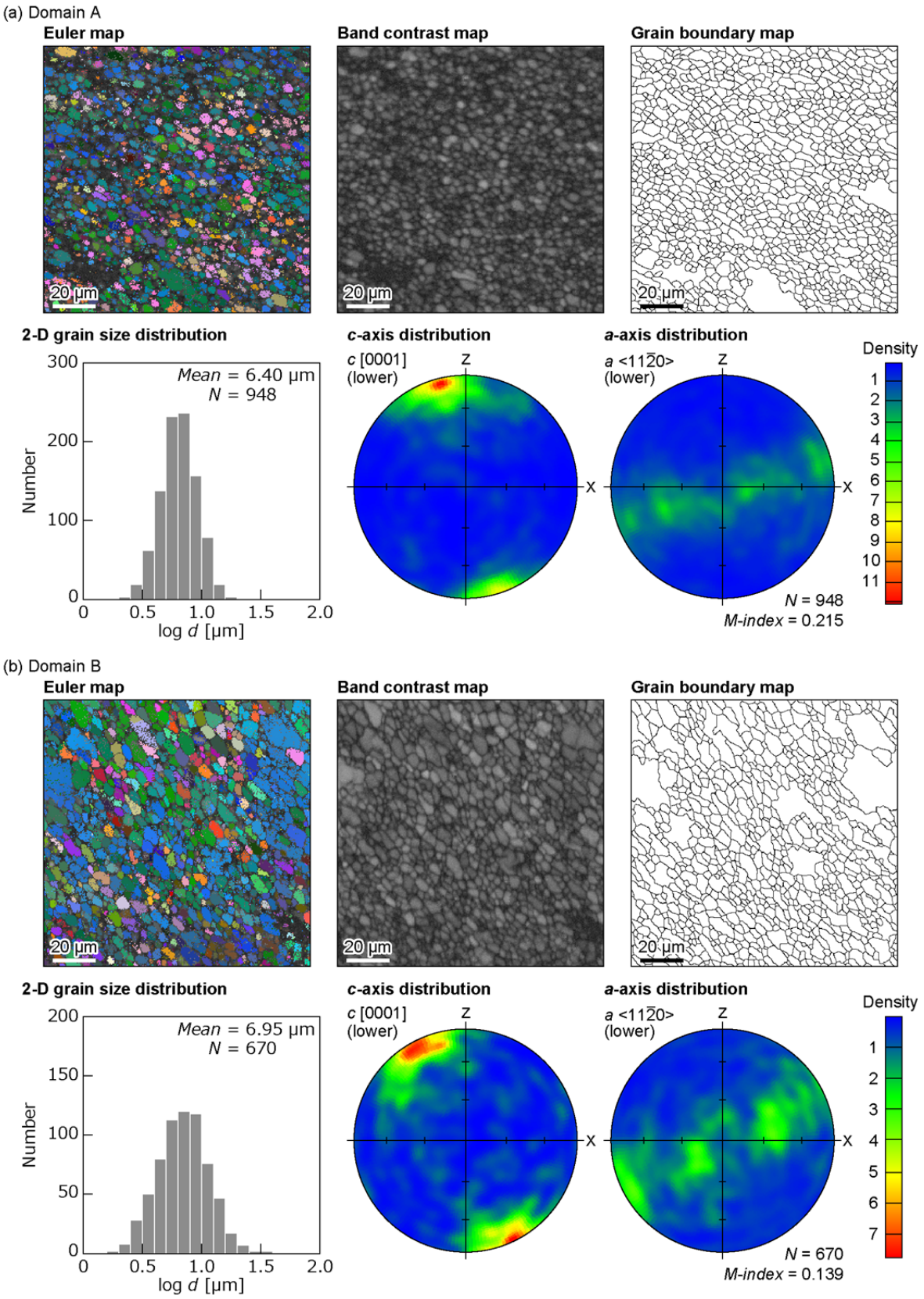

Fig. 4.6. SEM-EBSD analytical data for recrystallized quartz showing Euler maps, band contrast maps, grain boundary maps, two-dimensional grain size (d) distributions of recrystallized quartz, and pole figures (lower-hemisphere, equal-area projections) of the *c*-axis and *a*-axis of recrystallized quartz. Color of each analyzed point in the Euler map represents the Euler angle. The brightness in the band contrast map represents the band quality of each analyzed point that shown in lighter color as the contrast (quality) is high.. Analyzed domains are shown in Fig. 4.3a, d–i.

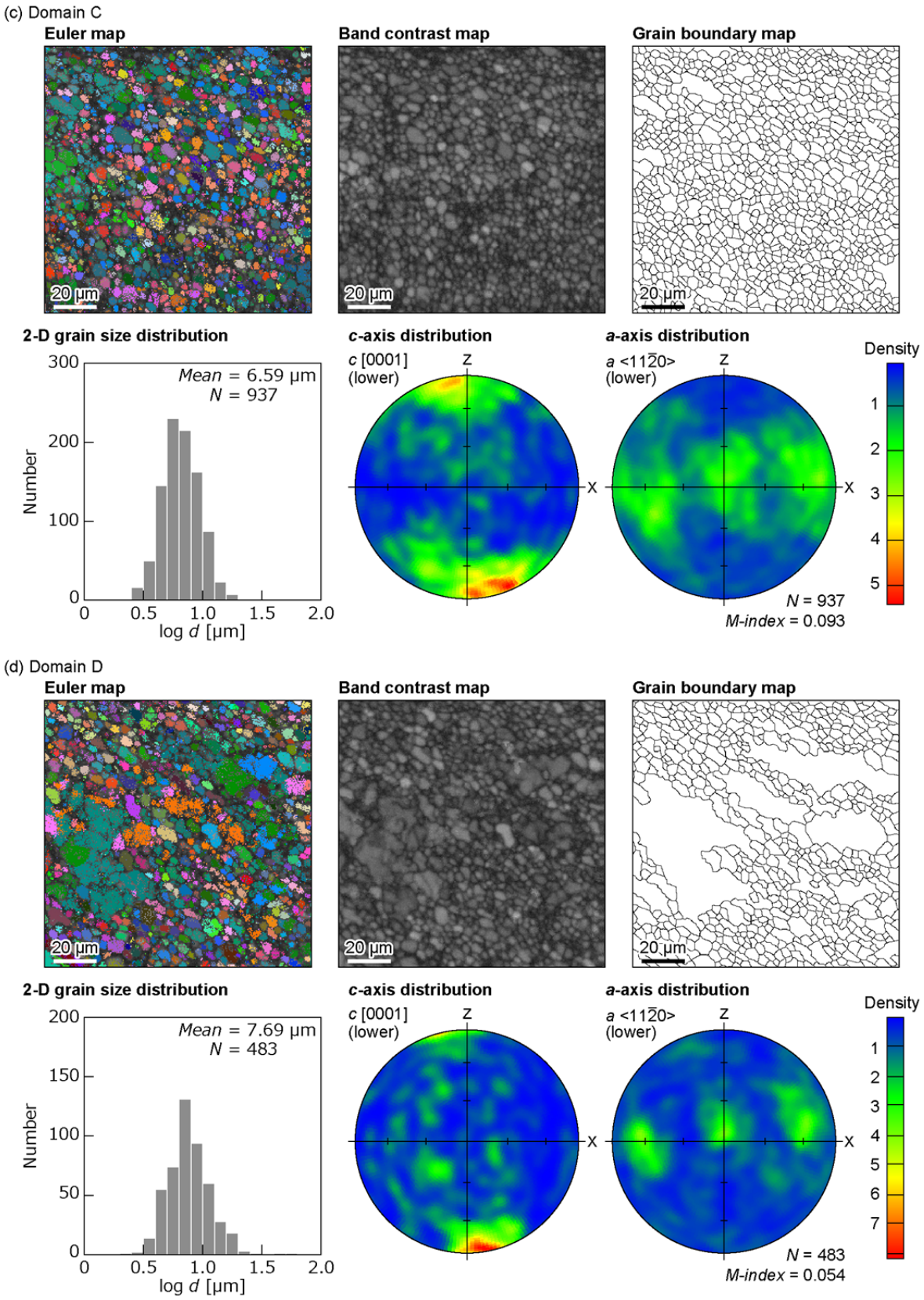

Fig. 4.6. Continued.

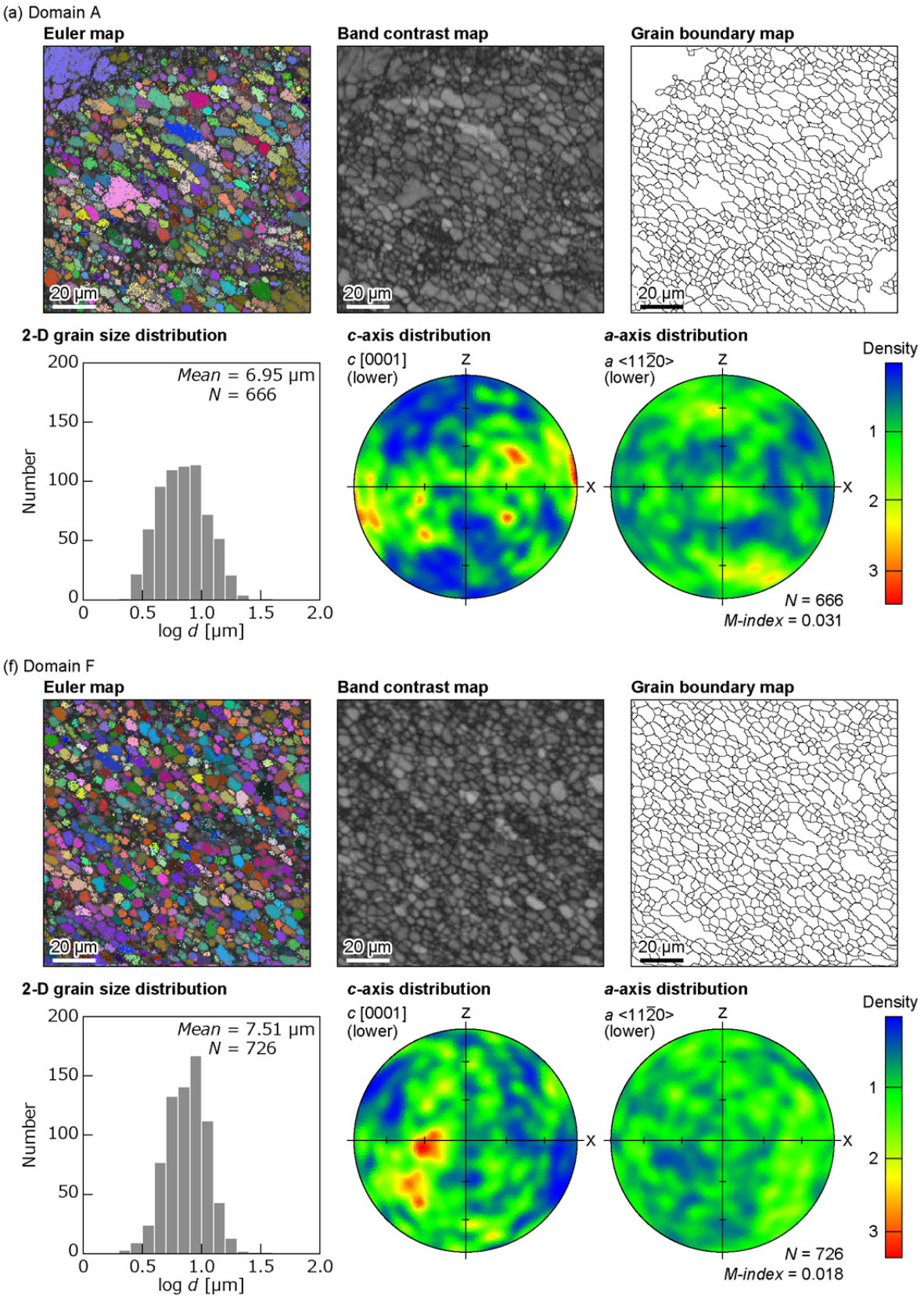

Fig. 4.6. Continued.

4.5. Calcite *e*-twin analysis

4.5.1. Principles

Deformation *e*-twin in calcite forms under a shear stress of ~10 MPa on the *e*-planes (Burkhard, 1993; Fig. 4.7a). Calcite slip data, using a combination of glide directions and the attitudes of the *e*-planes, can provide an estimate of the principal stress axis and the stress ratio, $\Phi = (\sigma_2 - \sigma_3)/(\sigma_1 - \sigma_3)$, as well as fault slip data (Weiss, 1954; Turner, 1962). This method has been applied to calcite twins in limestone (Groshong, 1975; Engelder, 1979), calcite veins (Kilsdonk and Wiltschko, 1988; Jaya and Nishikawa, 2013), marble (Craddock et al., 1991), or more rarely, to amygdules filled with calcite (Craddock and Magloughlin, 2005). Moreover, the density of *e*-twins has been used as a differential stress meter (Rowe and Rutter, 1990; Sakaguchi et al., 2011). Calcite can form *e*-twins on three planes because of the three-fold symmetry of calcite around the *c*-axis (Fig. 4.7b). The greater the differential stress acting on the calcite grain, two (doublet) or three (triplet) sets of *e*-twins on symmetry-related *e*-planes could be formed. Using the above features, Yamaji (2015) proposed a method for estimating the differential stress based on the ratio of twinned and untwinned planes (twinning ratio) and the percentages of *n*-plets (*n* = 0, 1, 2, and 3) grains.

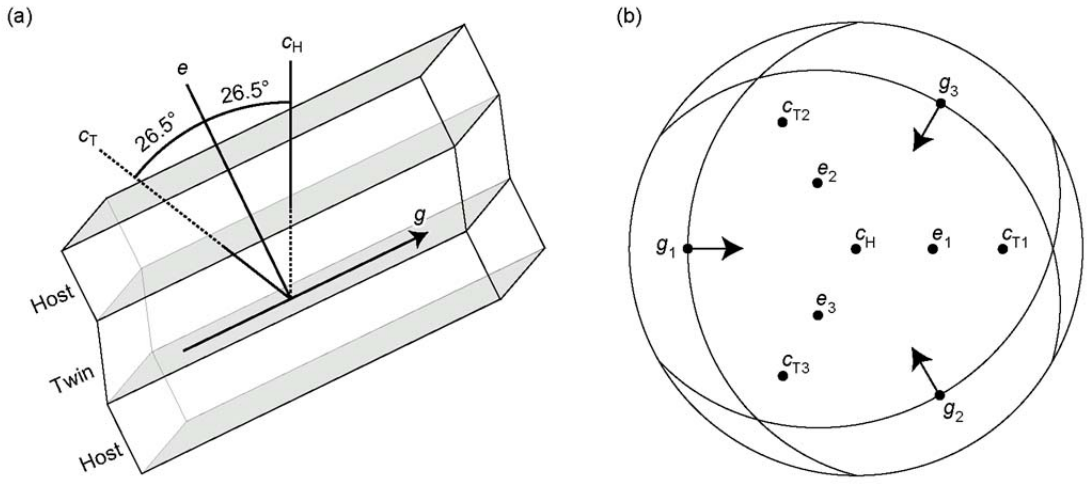

Fig. 4.7. (a) Geometry of calcite *e*-twins. Schematic diagram of the angular relationships between the *c*-axis of the host domain (c_H) and the *c*-axis of the twinned domain (c_T), the pole to the *e*-plane (e), and the glide direction (*g*). (b) Lower-hemisphere equal-area projection showing the three-fold symmetry in relation to the *e*-twins, modified after Burkhard (1993).

4.5.2. Analytical methods

The paleostress conditions have been estimated using *e*-twins of calcite that fill amygdules in the thick pseudotachylyte pool from the Taburi outcrop (Fig. 4.5d–f). The mutual relationships between the *c*-axis orientation of the host and the twinned domain, attitude of the *e*-plane, and direction of gliding are well understood and they can be expressed in terms of the geometry of calcite (Fig. 4.7). Based on these relationships, it is possible to

measure two of the four orientations noted above, and the remaining two can be calculated. In previous studies, the *c*-axis orientation of the host domain and the attitude of the *e*-plane were measured using a universal-stage (Jaya and Nishikawa, 2013). However, the universal-stage method suffers from mechanical limitations that prevent the assessment of all the twin data in three dimensions. To overcome this problem, therefore slip data was determined using the SEM-EBSD method, making it possible to measure fully the crystallographic orientations of the host and twinned domains (Fig. 4.8). The slip data were prepared by following five steps. 1) The crystallographic orientations of the host and twinned domains were measured by mapping or by line-scanning using the SEM-EBSD analysis (Fig. 4.8a, b). The analysis area was set to cover the grain. The SEM-EBSD analysis of calcite was performed under the same conditions except for the setting the analysis area as outlined above for quartz. 2) The mean orientations of the *c*-axis of the host and twinned domains were calculated (Fig. 4.8c). 3) Orientations of the poles to the *e*-twin planes was determined. These bisect the acute angles between the *c*-axis orientations of the host and twinned domains (Fig. 4.8c). 4) The glide directions were calculated. The glide direction lies 90° from the pole to the *e*-twin plane and within the plane that contains both the *e*-twin plane pole and the *c*-axis of the host domain (Fig. 4.8c). 5) The data were then converted from the sample coordinate system into a system with N–S, E–W, and top–bottom coordinates. Calcite can form *e*-twins on three different planes because of the three-fold symmetry of calcite around the *c*-axis. If two or three orientations of the twin plane occur in one calcite grain, all the differently oriented planes must be treated as different slip data. During this study, 1871 sets of slip data from 2535 calcite grains in the amygdules were prepared. In addition, the percentages of *n*-plet grains were calculated using the results of this SEM-EBSD analysis.

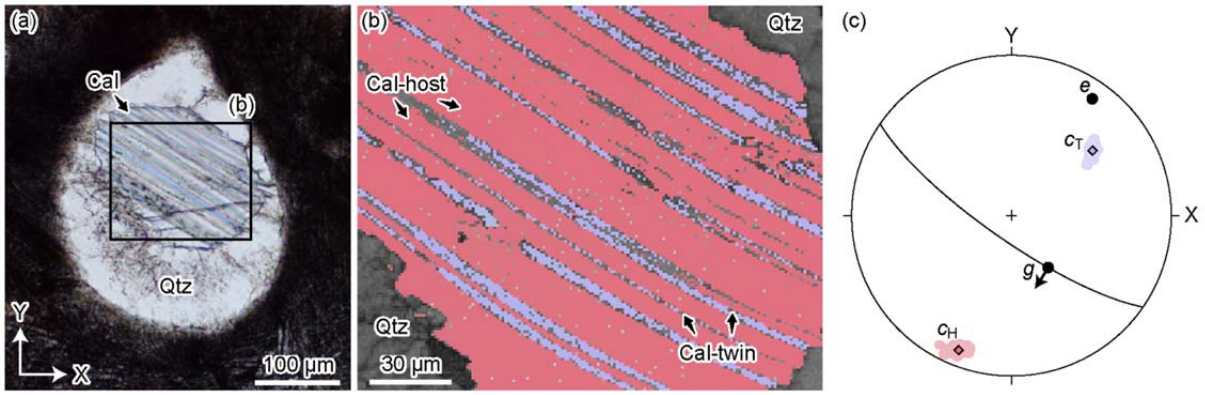

Fig. 4.8. (a) Photograph of the calcite grain in the amygdules (plane polarized light). (b) Euler map on band contrast map. Color of each analyzed point in Euler map represents the Euler angle. (c) Lower-hemisphere equal-area projection showing calculated mean orientations of the *c*-axis of the host (c_H) and twinned domains (c_T), pole of *e*-plane (*e*) and gliding direction (*g*) with analyzed *c*-axis orientations of the host and twinned domain.

Several methods for reconstructing the principal stress axis and the stress ratio from slip data have been proposed (Turner, 1953; Angelier and Mechler, 1977; Yamaji, 2000; Yamaji et al., 2006). These methods estimate the stress state based on the Wallace–Bott hypothesis that the displacement direction of the fault is parallel to the resolved shear stress (Wallace, 1951; Bott, 1959). In this study, the Hough-transform-based inversion method (Yamaji et al., 2006; Sato, 2006) was used. This method is advantageous because it can identify statistically valid multiple peaks using the generalized Hough-transform (Yamaji et al., 2006; Sato, 2006). To assist in the determination of the paleostress state, HIM (Hough-transform Inverse Method main processor) software version 1.10 (Sato, 2010a) was used to estimate the stress solution, and Peak Picker software version 1.01 (Sato, 2010b) was used to detect the peak of the stress solution.

4.5.3. Results

Fig. 4.9 shows the estimated orientations of the principal stress axes and stress ratios, and their optimum solutions, tangent-lineation diagram and distribution of misfit angles from the calcite twins in amygdules of the pseudotachylyte pool in the Taburi outcrop. The optimum estimated σ_1 axis trends 228° and plunges 55°, whereas the σ_3 axis trends 320° and plunges 1°. The stress ratio is 0.78. Only one stress solution was detected with the Peak Picker software. The percentages of *n*-plet grains are as follows: zeroplets 43.1%, singlets 40.9%, doublets 15.0%, and triplets 0.9%. The twinning ratio is 24.6%.

4.6. Discussion

4.6.1. Deformation mechanisms in recrystallized quartz

Tthree types of *c*-axis LPO patterns as Z-maximum, weak XY girdle, and relatively random were determined. Therefore, the M-index was used as an auxiliary of the *c*-axis LPO pattern estimated by visual inspection. If this classification by visual inspection is correct, the M-index values should be larger in the Z-maximum and smaller in the random *c*-axis LPO pattern. As the M-index values do show such a trend, this classification by visual inspection is generally correct. However, because the unique M-index value for the boundary between these types of *c*-axis LPO patterns has not been defined, it has not been possible to determine the LPO patterns using only the M-index.

Distinct Z-maximum *c*-axis LPO patterns for domains A–D suggest that deformation has occurred by dislocation creep. The quartz grains in the analyzed domains have low-angle boundaries in the band contrast maps, as shown in Fig. 4.10, and the recrystallized grains are of similar sizes to the subgrains. These observations suggest the deformation by dislocation

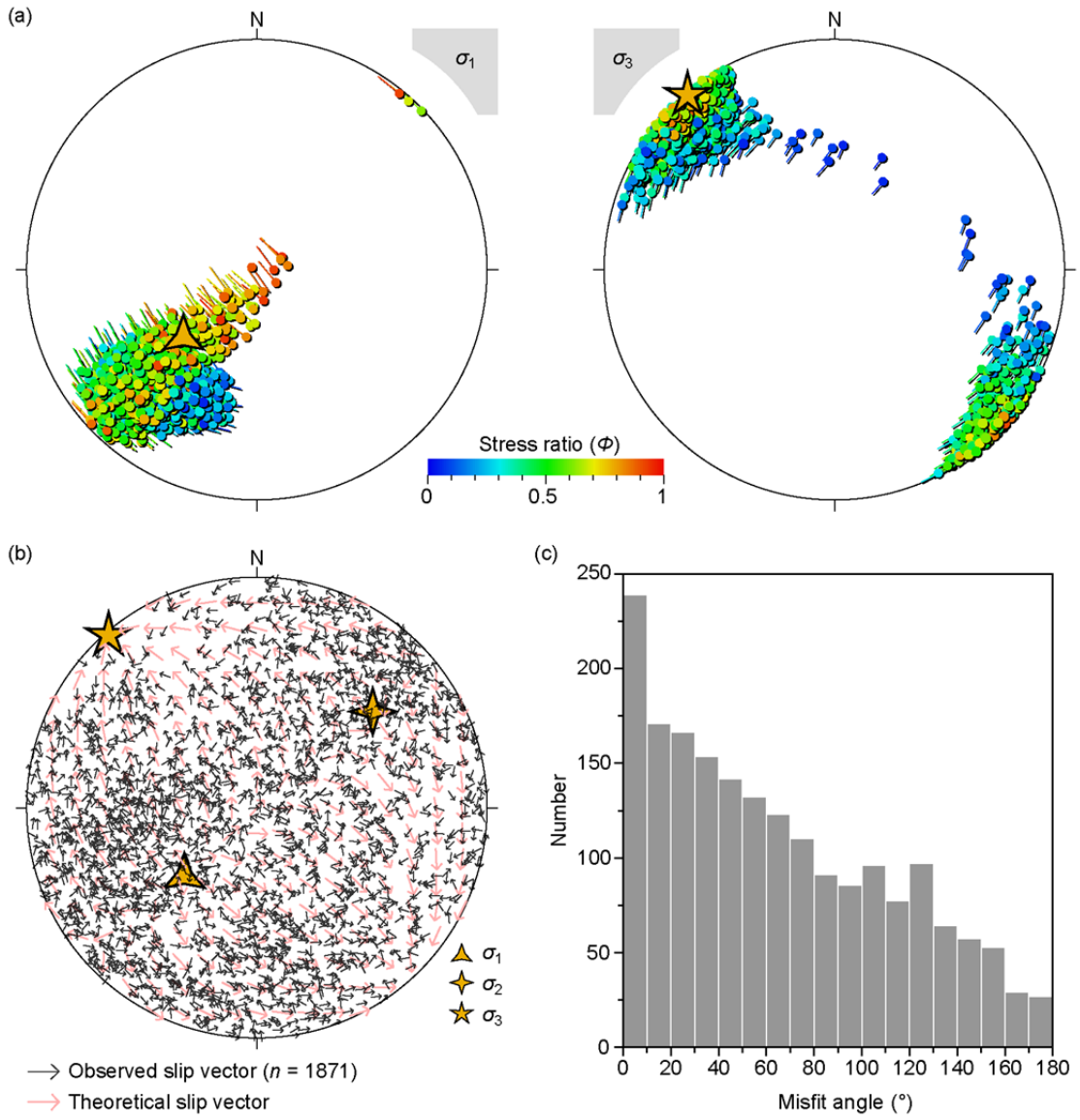

Fig. 4.9. (a) Detected stress state from calcite e-twins. Each tadpole-shaped symbol indicates a candidate for the stress solution, and the tails attached to the circles of theσ_1 and σ_3 axes show the azimuths of the corresponding σ_1 and σ_3 axes, respectively. A triangle and a star symbols show the optimum solutions. Lower-hemisphere, equal-area projection. (b) Tangent-lineation diagram of the analyzed twin planes and glide directions. Pink and Gray arrows indicate theoretical glide directions for the stresses and observed glide directions. (c) Histogram of misfit angles for the best-fitting stress tensor.

creep was accompanied by subgrain rotation recrystallization, and that grain size reduction has not occurred after the subgrain rotation recrystallization. The LPO pattern for domain E shows a weak XY girdle. The deformation under dislocation creep and the activation of the prism [c] slip system can produce an X-axis concentration (X-maximum) c-axis LPO pattern (Bouchez et al., 1984). It is considered that the activation of the prism [c] slip system acts at temperatures >550–600°C (Mainprice et al., 1986; Okudaira et al., 1995). However, activation of the prism [c] slip system was unlikely in our sample because mylonitization of the sample occurred after the pseudotachylyte formation in the brittle regime. On the other

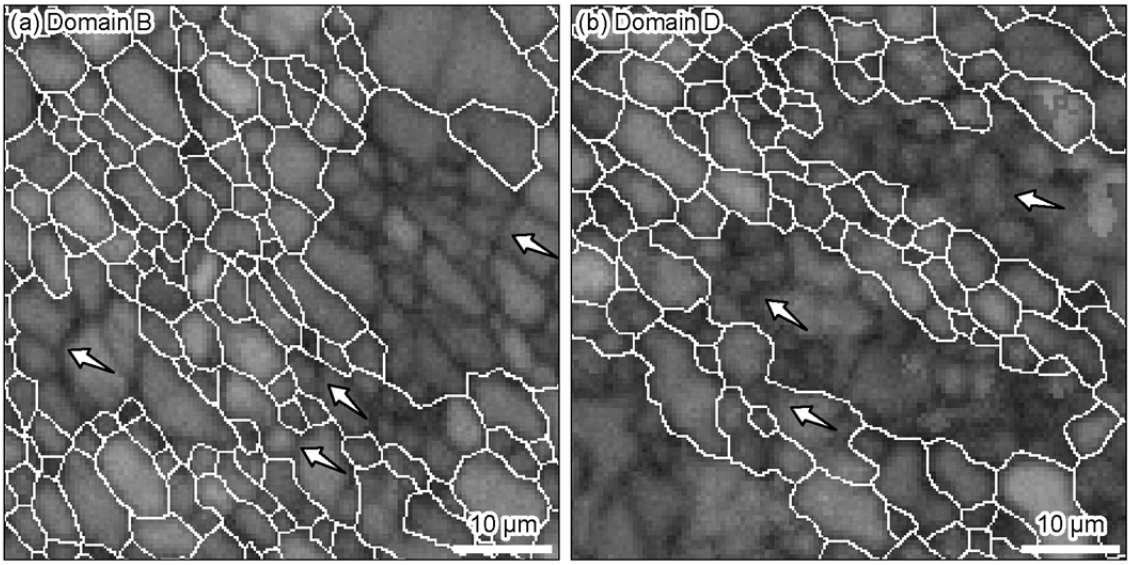

Fig. 4.10. Grain boundaries of quartz grains in the band contrast maps of (a) dmain B and (b) dmain D. White lines show high angle (>10°) boundaries. Connection of the relatively dark color band contrast points show subgrain boundaries (white arrows).

hand, quartz deformation by dissolution–precipitation creep, classified into grain boundary diffusion creep (i.e., Coble creep; Coble, 1963), could make the X-axis concentration *c*-axis LPO pattern (Takeshita and Hara, 1998; Hippertt and Hongn, 1998). This development of LPO pattern is attributed to anisotropic growth/dissolution rates on different crystallographic directions of quartz (Tullis, 1989). GBS, which is classified as a GSS creep as well as the diffusion creep, causes weakening of the former existing LPO (Casey and McGrew, 1999; Bestmann et al., 2011). Although domain E is considered to have been deformed by GSS creep, it is difficult to determine whether the deformation mechanism is diffusion creep or GBS by the *c*-axis LPO pattern. The relatively random LPO pattern for domain F suggests deformation by GSS creep, similar to domain E.

Grain size reduction (Rutter and Brodie, 1988; Bons and Urai, 1992) and stress drop (Rutter and Brodie, 1988; Wightman et al., 2006) are considered to cause a transition from GSI creep to GSS creep. Observation of the subgrains suggests grain size reduction occurred by subgrain rotation recrystallization; however, the mean grain size of each domain is within ±1 standard deviation of the grain size (Table 4.1). Static grain growth could occur in the diffusion creep field (Tullis and Yund, 1982; Wightman et al., 2006); however, it is unlikely that the grain sizes in domains E and F, away from the shear-zone center, are smaller than in the shear-zone center before static grain growth occurs. Therefore, the transition from GSI creep to GSS creep cannot be explained only by grain size reduction. As the grain size is roughly equal, diffusion creep occurs at a lower differential stress than dislocation creep (Rutter, 1976). Takeshita and Hara (1998) reported a host-controlled and X-maximum *c*-axis

LPO patterns from a quartz vein deformed under greenschist-facies conditions and they explained that the variations in *c*-axis LPO patterns indicate that the two deformation mechanisms (i.e. dissolution and dissolution-precipitation creep) were active as a result of the variations in the differential stress. Similarly, in our sample, it is inferred that the variations in differential stress resulted in a change in deformation mechanism. That is, grains in the shear-zone center are deformed in the dislocation creep field with relatively large differential stress, and the grains away from the shear-zone center are deformed in the GSS creep field with relatively small differential stress. Therefore, deformation by dislocation creep and grain size reduction occurred in each of the six domains at the beginning; thereafter, stress localization and/or stress drop caused the transition from dislocation creep to GSS creep in domains E and F. In order for GSS creep deformation to occur in domains E and F, while retaining the distinct LPO pattern in domains A–D, two mechanisms (dislocation creep and GSS creep) acted together during the deformation of the mylonitized pseudotachylyte. Therefore, the deformation must have occurred in the transition region of dislocation creep and GSS creep.

4.6.2. Estimates of temperature based on the quartz LPO patterns

The Z-maximum LPO pattern for domains A–D indicates deformation under dislocation creep and activation of the basal <*a*> slip system (Lister and Hobbs, 1980; Schmid and Casey, 1986). Activation of the basal <*a*> slip system indicates deformation under greenschist-facies conditions at temperatures of 300–400°C (Takeshita and Wenk, 1988; Bhattacharya and Weber; 2004). The estimated temperatures, together with the coexistence of mylonites and pseudotachylytes in the ASZ, suggest that shearing in this granitoids took place in the ductile-to-brittle transition regime (300–400°C; Brace and Kohlstedt, 1980; Stöckhert et al., 1999). However, such a low temperature could also have caused activation of the rhomb <*a*> slip system and the formation of the type-I crossed girdle LPO pattern (Lister and Hobbs, 1980; Schmid and Casey, 1986). Therefore, the Z-maximum LPO pattern has been reported to occur as the sole pattern (Hippertt and Hongn, 1998) or in coexistence with the type-I crossed girdle LPO pattern (Lacassin, 1987; Sakakibara et al., 1992). The condition for forming the Z-maximum LPO pattern has been considered as requiring relatively higher shear strain than for forming the type-I crossed girdle LPO pattern (Lloyd et al., 1987; Hippertt and Hongn, 1998).

4.6.3. Differential stress estimated from the grain size of recrystallized quartz

Figure 4.11 shows the two-dimensional mean grain sizes with standard deviations from

two domain sets on the grain size paleopiezometer diagram for dislocation creep (after Stipp and Tullis, 2003). Differential stress is estimated to have been 110–130 MPa. Further from the shear-zone center, the mean grain size increases and therefore, the differential stress decreases.

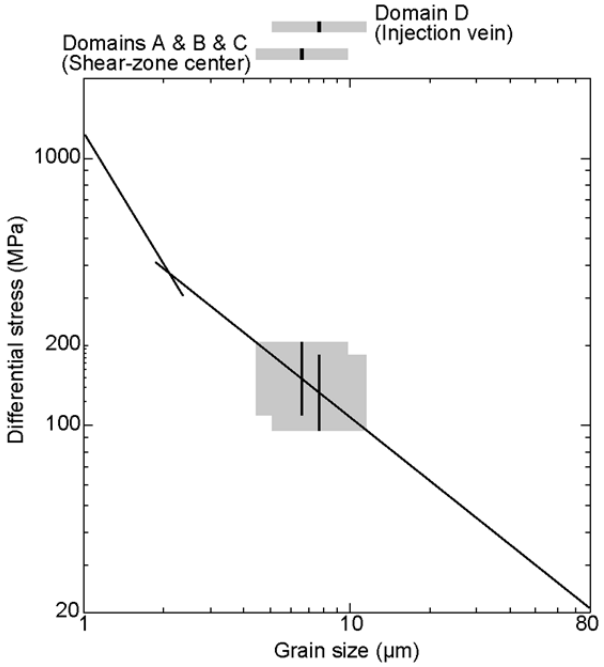

Fig. 4.11. Recrystallized grain size paleo-piezometer diagram modified after Stipp and Tullis (2003). Horizontal bars at the top of the figure represent the mean grain sizes of quartz with standard deviation in each domain sets.

4.6.4. Estimates of differential stresses and strain rates based on the boundary between dislocation creep and GSS creep fields

Two mechanisms, dislocation creep and GSS creep, acted together during the deformation of the mylonitized pseudotachylyte. For quartz grains, in order to constrain the stresses and strain rates, differential stress vs. grain size maps for dislocation creep and GSS creep was estimated following the work of Okudaira and Shigematsu (2012). The GSS creep map contained two mechanisms, GBS and diffusion creep. The dislocation creep flow law is represented by the following equation (Hirth et al., 2001):

$$\dot{\varepsilon} = A\left(f_{\mathrm{H_2O}}\right)^{p}\sigma^{4}\exp\left(\frac{-H_{\mathrm{L}}}{RT}\right) \tag{4.1}$$

where $\dot{\varepsilon}$ is the strain rate (s^{-1}), σ is the differential stress (MPa), T is the absolute temperature (K), R is a gas constant (8.314 J/mol/K), A is a material parameter ($\log A = -11.2$ MPa^{-4}/s), f_{H2O} is the water fugacity, p is the water fugacity exponent, and H_L is the molar activation enthalpy (135×10^3 J/mol). The value of f_{H2O} is obtained from pressure and temperature at depth (Tödheide, 1972; Kerrick and Jacobs, 1981; Holland and Powell, 1991). When the model is applied to low-temperature conditions, the values of f_{H2O} for a pressure of 300 MPa and temperatures of 300 and 400°C are ~25 and ~60 MPa (Tödheide, 1972), and ~24 and ~62 MPa (Holland and Powell, 1991), respectively. In this study, the model proposed

by Holland and Powell (1991) was used, following Okudaira and Shigematsu (2012).

The GBS flow law is represented by the following equation (Gifkins, 1976):

$$\dot{\varepsilon} = \frac{64 \times 10^{12} b^3 D_{\mathrm{G}}}{\mu k T d^2} \sigma^2 \exp\left(\frac{-H_{\mathrm{G}}}{RT}\right) \tag{4.2}$$

where b is the Burgers vector (4.92×10^{-10} m), μ is the shear modulus of quartz (42×10^3 MPa), k is the Boltzmann constant (1.381×10^{-23} J/mol/K), d is the three-dimensional grain size (m), and H_{G} and D_{G} are the molar activation enthalpy (137×10^3 J/mol) and a pre-exponential factor (3.7×10^{-10} m^2/s), respectively, for the bulk or effective diffusion coefficient of silicon in the presence of water (Farver and Yund, 2000). Various methods for estimating three-dimensional grain size from two-dimensional data have been proposed (Underwood, 1973; Hughes, 1978; Kong et al., 2005). In this study, the method of obtaining three-dimensional grain sizes by multiplying the two-dimensional grain sizes by $4/\pi$ (Kong et al., 2005) was adopted.

The diffusion creep flow law is represented by the following equation (Coble, 1963):

$$\dot{\varepsilon} = \frac{10^6 \times 148 \Omega D_{\mathrm{G}} W}{\pi k T d^3} \sigma \exp\left(\frac{-H_{\mathrm{G}}}{RT}\right) \tag{4.3}$$

where Ω is the atomic volume and W is the grain boundary thickness (1×10^{-9} m). Ω was approximated by kV/R (Okudaira and Shigematsu, 2012), where V is the molar volume of quartz (2.6×10^{-5} m^3/mol).

Based on Eqs. (4.1)–(4.3), the deformation mechanism maps for quartz at temperatures of 300 and 400°C were constructed, indicating a mean grain size with the standard deviation from three domain sets (Fig. 4.12). Based on the deformation mechanism maps and the mean grain sizes at which the change in the dislocation creep and GSS creep occurs, the differential stresses and strain rates are estimated to have been 110–130 MPa and 7.0×10^{-13} to 1.0×10^{-12} s^{-1} at 300°C, and 45–53 MPa and 6.0×10^{-12} to 1.0×10^{-11} s^{-1} at 400°C. As the differential stress is estimated to have been 110–130 MPa (using the grain size paleopiezometer), the temperature during deformation is inferred to have been 300°C.

4.6.5. Stress inversion using calcite twins

Figure 4.13 shows the foliation and lineation of the fault rock at Taburi, and the orientation of the optimum principal stress axis solution from the calcite *e*-twin inversion method. The optimum slip direction was calculated assuming that the detected principal stress axis operated to the observed fault foliation. The misfit angles between the optimum slip direction of the detected stress and the observed lineation were 26.3° and 14.9° in the case of the pseudotachylytes, and 7.5° and 23.2° in the case of cataclasites; the mean misfit

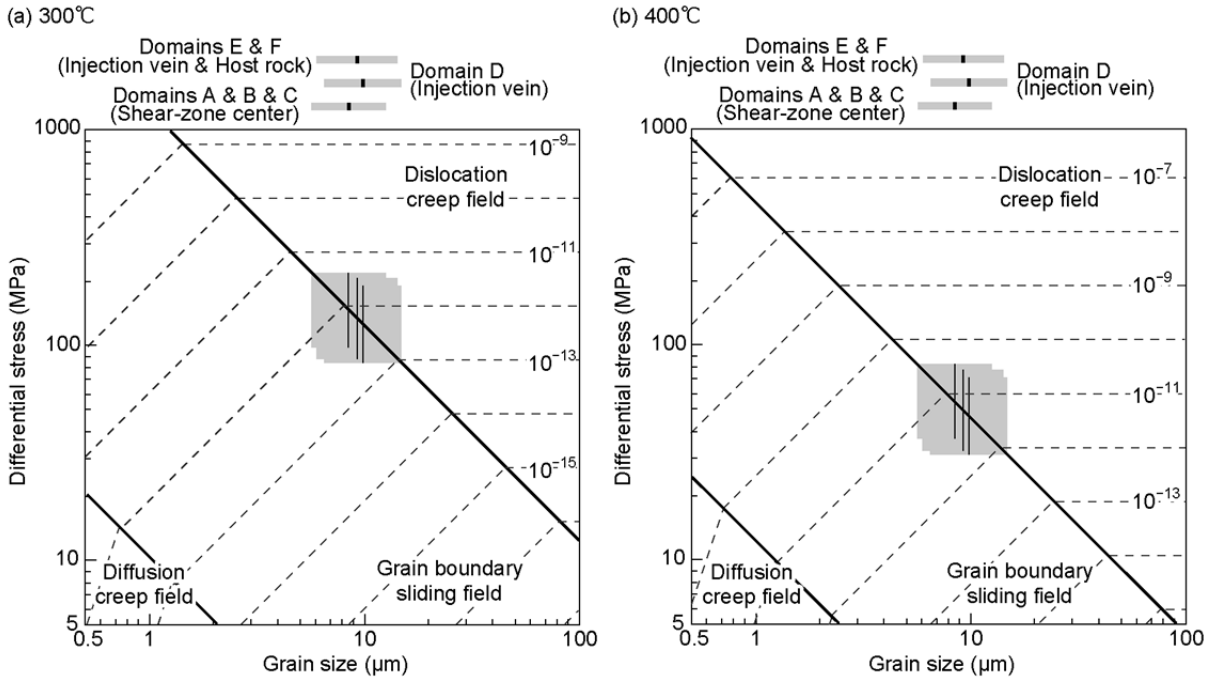

Fig. 4.12. Deformation mechanism map of differential stress versus recrystallized quartz grain size at (a) 300°C and (b) 400°C, modified after Okudaira and Shigematsu (2012). Horizontal bars at the top of each figure represent the mean grain sizes of quartz with standard deviation in each domain sets.

angle for four fault rocks was 18.0°. A value for the misfit angle of less than 30° (Saintot et al., 2011) or 25° (Navabpour et al., 2010) is acceptable, as the faults have been affected by only a single stress regime. Therefore, it can be inferred that the small shear zone at Taburi was activated under a stress state that was approximately equal to the stress state from calcite *e*-twins. It is inferred that the ASZ was activated under a stress state that caused sinistral normal movements, both before and after pseudotachylyte formation.

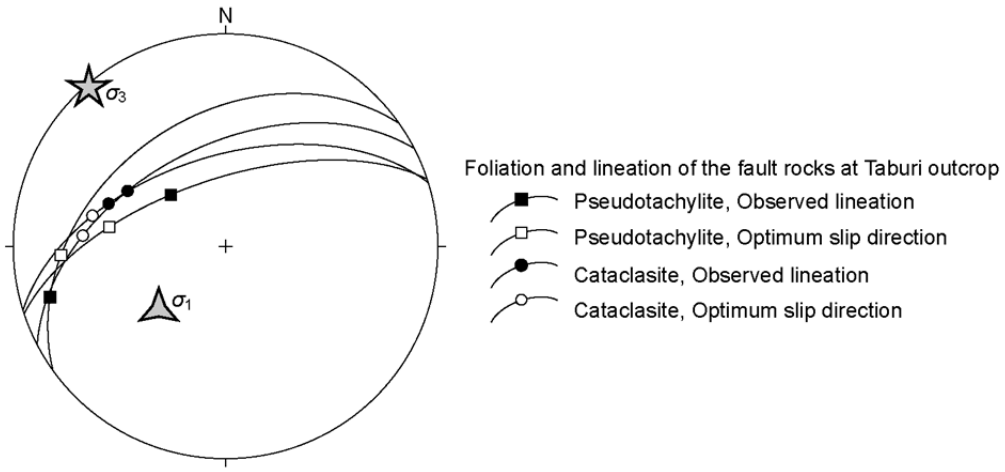

Fig. 4.13. Relationship between the observed lineation and optimum slip directions based on the optimum stress solution of the calcite *e*-twin inversion method (after Fig. 4.9). Great circles represent foliations in the fault rocks. Lower-hemisphere, equal-area projection.

4.6.6. Estimates of differential stress from calcite twins

Based on the result of the stress inversion, an only optimum solution was detected as the peak solution by the Peak Picker software. Assuming that the deformation twin is formed under certain conditions, it is possible to estimate the differential stress from the twinning ratio, the twinning incidence and the percentages of *n*-plet grains (Yamaji, 2015). Figure 4.14 shows the relationship between the twinning ratio, the twinning incidence and the percentages of *n*-plet grains with respect to the differential stress. The observational bias is related to the difficulty of observing twin planes when they make a small angle with the thin-section plane (Terzaghi, 1965; Yamaji, 2015). The observational bias is increased when there are many twins parallel to the observation plane. Considering the twin deformation as a shear deformation, the *e*-twin plane tends to develop parallel to the attitude of the shear zone (sub-parallel to the XY plane at large shear strains). As the present sample was cut in an orientation close to the XZ plane, the observation bias is considered less than in the case where the sample is cut parallel to the XY plane. Although the maximum percentage of singlets is ~28% for the biased case, the percentage of singlets is 40.9% in our sample. Since it is unlikely that large observational bias occurred, the differential stress was estimated based on the unbiased case. The estimated differential stress from the twinning ratio (24.6 %)

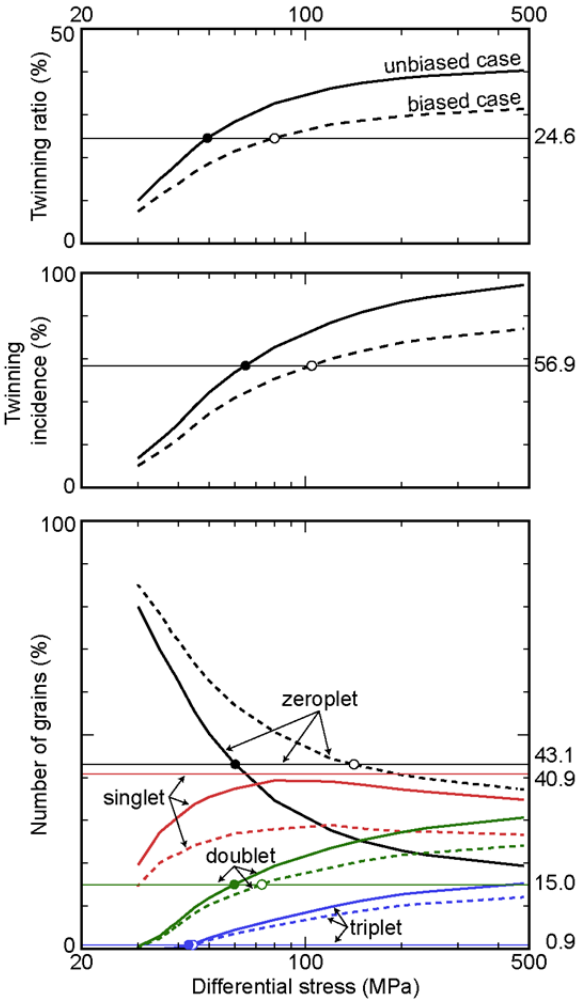

Fig. 4.14. Relationship between differential stress and (a) the twinning ratio, (b) the twinning incidence and (c) the percentages of *n*-plet grains, after Yamaji (2015). Solid and dotted lines represent the unbiased case and the biased case, respectively. Thin lines represent the estimated twinning ratio (24.6 %), twinning incidence (56.9 %) and percentages of *n*-plet grains (zeroplets 43.1 %, singlets 40.9 %, doublets 15.0 %, and triplets 0.9 %) in the present sample.

is ~50 MPa, whereas from the percentages of *n*-plet grains, it is ~60 MPa from the zeroplets and doublets and ~41 MPa from the triplets. Although the measured percentage of singlets is higher than the maximum value of theory, the closest value suggests a stress of ~80 MPa. Accordingly, the differential stress recorded by the calcite twins in the amygdules of the analyzed pseudotachylyte is estimated to have been 40–80 MPa. However, non-harmonic slip data exists for the optimal solution on the tangent-lineation diagram (Fig. 4.9c), and the estimation result of the differential stress is less reliable than the stress inversion result.

4.6.7. Timing of the formation of deformation twins

The ASZ provides evidence of repeated plastic (mylonite formation) and brittle (pseudotachylyte and cataclasite formation) deformations, as in the case of the Oshima outcrop. In the Taburi outcrop, however, little cataclastic reactivation of the fault at shallower depths or near surface has been overprinted after the formation of the pseudotachylyte veins. In addition, mylonitization has not been observed in the quartz infillings of the amygdules. A peak stress solution for the calcite twin was detected only once with the Peak Picker software. Hence, it is inferred that most calcite twins in the amygdules formed during a single stage of deformation or during several stages of deformation with similar stress states that cannot be distinguished by statistical methods. The morphology of the *e*-twins in the amygdules is one of predominantly thin straight twins (<200°C; Burkhard, 1993; Passchier and Trouw, 2005) or thick (>1 μm) straight twins (150–300°C; Burkhard, 1993; Passchier and Trouw, 2005), suggesting the twins in the amygdules formed at 150–200°C. The stage of *e*-twinning that followed the formation of the pseudotachylyte can be placed on the cooling curve for the Inagawa Granodiorite (Fig. 4.15). Zircon U–Pb and fission-track (FT) ages have been reported for a thick pseudotachylyte vein in the Taburi outcrop and for the surrounding host granitoids (Murakami et al., 2006a). At a distance of 70 cm from the thick pseudotachylyte vein, the host granodiorite yielded a zircon U–Pb age of 73 ± 3 Ma and an FT age of 73 ±7 Ma. The thick pseudotachylyte vein and the cataclasite in contact with the thick pseudotachylyte pool yielded U–Pb ages of 76–67 Ma, within the error of the U–Pb age of the host granodiorite, whereas the FT ages are 62–56 Ma for the cataclasite and 53 ± 9 Ma for the pseudotachylyte (Murakami et al., 2006a). Track length measurements indicate that the FT system of zircon was completely reset, and that the age of 53 Ma is therefore considered the age of formation of the pseudotachylyte (Murakami et al., 2006a). The annealing of zircon FTs is completed within a few seconds at ~1000°C (Murakami et al., 2006b), and the melting point of quartz is ~1100°C at a pressure of >200 MPa in the system SiO_2–H_2O (Kennedy et al.,

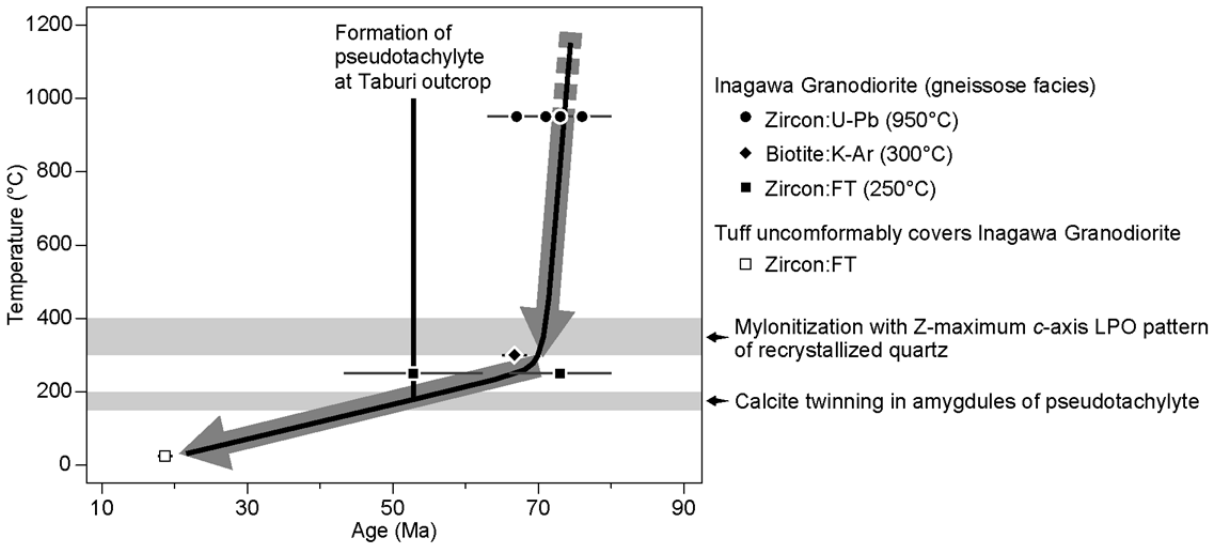

Fig. 4.15. Cooling and deformation history of the Inagawa granodiorite. The radiometric ages are zircon U–Pb ages (76–67 Ma; Murakami et al., 2006a), a biotite K–Ar age (66.7 Ma; Yamasaki and Ozaki, 2012), and a zircon FT age (73 Ma; Murakami et al., 2006a). Closure temperatures for the U–Pb and FT systems of zircon are 950°C (Hodges, 2005) and 250°C (Hurford, 1986; Tagami et al., 1998), respectively, and for the K–Ar system of biotite the closure temperature is 300°C (Dodson and McClelland–Brown, 1985).

1962); therefore, the temperature of frictional melting can be considered to have been >1000°C. Based on the cooling curve, the host rock around the pseudotachylyte must have cooled to ~200°C at around 53 Ma, when the pseudotachylyte was made. The deformation twins of calcite in the amygdules were formed, therefore, at around 50 Ma following the formation of the pseudotachylyte. The timing of exhumation of the Inagawa Granodiorite to the surface has been estimated at 18.7 ± 1.0 Ma using FT dating (Sasao et al., 2011) of the tuff beds in the Miocene Iwamura Group that unconformably overlies the Inagawa Granodiorite 30 km NNE of the ASZ. Based on the cooling history and the estimated stress state mentioned above, it is inferred that the ASZ was activated under a stress state that caused sinistral–normal movements during the period 70–50 Ma.

Chapter 5: Discussion and conclusions

5.1. Comparison of paleostress estimated from HC and shear zones

The formation temperature of HC of each sample is 300–450°C on average. Assuming that the ASZ deformed in the brittle-to-plastic transition regime of quartz, its deformation temperature is considered to be 300–400°C (Brace and Kohlstedt, 1980; Stöckhert et al., 1999). Therefore, there is a possibility that the formation of HC and the activity of the ASZ may indicate the same period of paleostress in the time range when the deformation temperature overlaps. Beside the ASZ, the shear zone considered to overlap the deformation temperature has been reported from the Busetsu Granite (Ito and Miyake, 2011; Yamasaki and Ozaki, 2012). This shear zone extends NE-SW to ENE–WSW, and it is considered that it was deformed under the stress with the σ_3 axis trending NW-SE (Ito and Miyake, 2011). The *c*-axis LPO pattern of dynamically recrystallized quartz shows type-I crossed girdle and type-II crossed girdle, and each LPO pattern suggesting that the deformation has occurred at 300–450°C and 450–600°C (Schmid and Casey, 1986; Takeshita and Wenk, 1988; Takeshita, 1996; Passchier and Trouw, 2005). Therefore, the deformation temperature of this shear zone and the formation temperature of HC developing in the Busetsu Granite (320–420°C) are nearly overlapped. The orientation of σ_3 axis expected from the shear sense of the above two shear zones is NW–SE to WNW–ESE from the ASZ located on the north side, and NNW–SSE to NW–SE from the shear zone in the Busetsu Granite located on the south side. The orientations of σ_3 axis expected from the shear sense of the above two shear zones suggest counterclockwise rotation farther from the MTL similar to the orientation of the σ_3 axis estimated from HC. Moreover, the orientation of σ_3 axis expected from above two shear zones and detected from the HC of Group C is roughly coincides with NW−SE trend and low angle plunge. It is considered that these shear zones of the scales of tens of kilometers were formed reflecting the regional stress field. Since the orientation of σ_3 axis estimated from the shear zone and HC are harmonious, the paleostress recorded in HC reflects the regional stress field rather than the local stress as the sample scale. Therefore, the orientation of the σ_3 axis estimated from HC records the regional stress field at 75–64 Ma.

5.2. Paleostressfield developed in the Ryoke belt at the Late Cretaceous

HCs used to paleostress analysis are considered to have been formed in 75–64 Ma. Activities of Kashio phase-II (70–65 Ma; Takagi, 1997) and Ichinokawa phase (63–58 Ma; Takagi and Shibata, 1992) of the MTL are close to the formation age of HCs. The activity of

the MTL at Kashio phase-II caused the mylonitization of Ryoke granitoid distributed in approximately 800 m from the MTL (Takagi, 1986). No evidence of mylonitization such as grain size reduction was detected in the closest sample of the Shinshiro Tonalite and the Tenryukyo Granodiorite at 2.1–2.2 km away from the MTL. Therefore, prominent paleostresses detected from the HCs are not caused by the activity of the MTL at Kashio phase-II. The activity of the MTL at Ichinokawa phase is normal fault movement caused juxtaposition against the Sanbagawa metamorphic rocks (Kubota and Takeshita, 2008). Ichinokawa phase is considered to be consistent with the deformation timing of the D_2 deformation phases of the Sanbagawa metamorphic rocks (Kubota and Takeshita, 2008), and the deformation of the D_2 phase is considered to have developed a normal fault in the upper domain of the Sanbagawa belt (Osozawa and Pavlis, 2007; El-Fakharani and Takeshita, 2008). Since the MTL commonly dips to the north, and therefore Ryoke rocks overlie the Sanbagawa schists the tensile stress field that has been detected from the HCs of the Shinshiro Tonalite and the Tenryukyo Granodiorite distributed along the MTL is harmonic with the formation of the normal faulting. Accordingly, the formation timing of the HCs is probably older than the activity of the MTL in the Ichinokawa phase if the K-Ar age (63–58Ma) of fault gouges is adopted. However, the K-Ar age for fault gouges and the timing of the major activity of the MTL may not acculately coincide each other, therefore, it is considerd that the tensile stress field with the orientation of σ_3 axis normal to the MTL has been developed along the MTL as a preparatory stage of the activity of the MTL in the Ichinokawa phase just after the sinistral mylonitization of the Kashio phase II at about 70Ma. The correlation between the orientation of σ_3 axis and the distance from the MTL can be explained by the effect of tensile stress field become weekend with increasing the distance from the MTL.

The detected stress field away from the MTL is interpreted that the plate driving forces give constraints on the stress field (Zoback, 1992). Strike of the MTL and magmatic arc before the opening of the Japan Sea is considered to be about N30°E in the Late Cretaceous at the eastern margin of East Asia (Maruyama et al., 1997; Yamakita and Otoh, 2000; Ishida et al., 2003; Kojima et al., 2008). A number of studies reconstructed a plate movement subducted to the Eurasian plate in the Late Cretaceous; Pacific plate was moved in the velocity of 10.4 cm/year to N50°W at 74–53 Ma (Engebretson et al., 1985; Maruyama and Seno, 1986) and Izanagi plate was moved in the velocity of about 24 cm/year to N40°W or 17 cm/year to N30°W at 80 Ma and 60 Ma, respectively (Müller et al, 2016). Applying the relationship between the strike of the paleo MTL (N30°E) and plate motion subducted to the Eurasian plate at the timing of HC formation to the strike of the current MTL (N60°E), there is a possibility that the effect of compressive plate boundary forces has been recorded in the

orientation of the current N–S to N20°W. The orientation of σ_1 and σ_2 axes of prominent stress detected from Group F are distributed on the great circle normal to the poles trends 260° and plunges 7° (Fig. 3.13). Since the strike of this great circle (N10°W) and the orientation of compressive plate boundary forces (N–S to N20°W) are consistent, the orientation of σ_1 and σ_2 axes of prominent stress from Group F is considered to have been limited by the movement of the plate.

I arrive at the conclusion that the Cretaceous granitoids are affected by the compression by the plate convergence as a whole, and the influence of the paleostress related to the normal fault movement of the MTL at the Ichinokawa phase more strongly in the vicinity of the MTL. The study about the normal fault movement of the MTL at the Ichinokawa phase was mainly based on the deformation analysis of the Sanbagawa Belt, however, this study clarified the orientation of the paleostress that causes the normal fault movement from the Cretaceous granitoid along the MTL.

References

Adachi, Y. and Wallis, S., 2008, Ductile deformation and development of andalusite microstructures in the Hongusan area: constraints on the metamorphism and tectonics of the Ryoke Belt. *Island Arc,* **17**, 41–56.

Aizawa, S. and Takagi, H., 2008, Paleostress analysis and estimation of bending of the Median Tectonic Line using healed microcracks from the Ryoke Granites. *115th Ann. Meet. Geol. Soc. Japan, Abstr.*, 221.**

Anderson, E.M., 1951, *The Dynamics of Faulting and Dike Formation with Applications to Britain, 2nd ed.* Oliver and Boyd, Edinburgh, 206p.

Angelier, J. and Mechler, P., 1977, Sur une méthode graphique de recherche des contraintes principales également utilisable en tectonique et en sésmologie: la méthode des diédres droits. *Bulletin de la Société Géologique de Francei*, **7**, 1309–1318.

Baer, G., Beyth, M. and Reches, Z., 1994, Dikes emplaced into fractured basement, Timna Igneous complex, Israel. *Jour. Geophys. Res.*, **99**, 24039–24051.

Bestmann, M., Pennacchioni, G., Frank, G., Göken, M. and de Wall, H., 2011, Pseudotachylyte in muscovite-bearing quartzite: Coseismic friction-induced melting and plastic deformation of quartz. *Jour. Struct. Geol.*, **33**, 169–186.

Bhattacharya, A.R. and Weber, K., 2004, Fabric development during shear deformation in the Main Central Thrust Zone, NW-Himalaya, India. *Tectonophysics*, **387**, 23–46.

Bingham, C., 1974. An antipodally symmetric distribution on the sphere. *Ann. Statist.*, **2**, 1201–1225.

Bishop, C.M., 2006, Pattern Recognition and Machine Learning. Springer, New York. 738p.

Bodnar, R.J. and Vityk, M.O., 1994, Interpretation of microthermometric data for H_2O-NaCl fluid inclusions. *In*: Vivo, B.D. and Frezzotti, M.L. (Eds.), *Fluid Inclusions in Minerals, Methods and Applications*. Virginia Tech, Blacksburg, VA, 117–130.

Bons, P.D. and Urai, J.L., 1992, Syndeformational grain growth: microstructures and kinetics. *Jour. Struct. Geol.*, **14**, 1101–1109.

Bott, M.H.P., 1959, The mechanics of oblique slip faulting. *Geol. Mag.*, **96**, 109–117.

Bouchez, J.L. 1977, Plastic deformation of quartzites at low temperature in an area of natural strain gradient. *Tectonophysics*, **39**, 25–50.

Bouchez, J.L., Mainprice, D.H., Trepied, L. and Doukhan, J.C., 1984, Secondary lineation in a high-T quartzite (Galicia, Spain): an explanation for an abnormal fabric. *Jour. Struct. Geol.*, **6**, 159–165.

Boullier, A.M. and Gueguen, Y., 1975, SP-mylonites: Origin of some mylonites by superplastic flow. *Contrib. Mineral. Petrol.*, **50**, 93–104.

Brace, W.F. and Kohlstedt, D.L., 1980, Limits on lithospheric stress imposed by laboratory experiments. *Jour. Geophys. Res.*, **85**, 6428–6252.

Brantley, S. L., Evans, B., Hickman, S. H. and Crerar, D. A., 1990, Healing of microcracks in quartz :

implications for fluid flow. *Geology*, **18**, 136–139.

Burkhard, M., 1993, Calcite twins, their geometry, appearance, and significance as stress-strain markers and indicators of tectonic regime: a review. *Jour. Struct. Geol*., **15**, 351–368.

Casey, M. and McGrew, A.J., 1999, One-dimensional model of preferred orientation development. *Tectonophysicsi*, **303**, 131–140.

Coble, R. L., 1963, A model for boundary diffusion controlled creep in polycrystalline materials, *Jour. Appl. Phys*., **34**, 1679–1682.

Craddock, J.P. and Magloughlin, J.F., 2005, Calcite strains, kinematic indicators, and magnetic flow fabric of a Proterozoic pseudotachylyte swarm, Minnesota River valley, USA. *Tectonophysics*, **402**, 153–168.

Craddock, J.P., Moshoian, A. and Pearson, A. M., 1991, Kinematic analysis from twinned calcite strains in the marble mylonites of the central Grenville province, Canada. *Geol. Soc. Am. Abst. Programs*, **23**, 236.

Delaney, P.T., Pollard, D.D., Ziony, J.I. and McKee, E.H., 1986, Field relations between dikes and joints: Emplacement processes and paleostress analysis. *Jour. Geophys. Res*., **91**, 4920–4938.

Dezayes, C.T., Villemin, T. and Pêcher, A., 2000. Microfracture pattern compared to corescale fractures in the borehole of the Soultz–sous–Forêts granite, Rhine graben, France. *Jour. Struct. Geol*., **22**, 723–733.

Dodson, M. H. and McClelland–Brown, E., 1985, Isotopic and paleomagnetic evidence for rates of cooling, uplift and erosion. *Geol. Soc. Mem.*, **10**, 315–325.

El-Fakharani, A.H. and Takeshita, T., 2008, Brittle normal faulting in the highest-grade Sambagawa metamorphic rocks of central Shikoku, southwest Japan: Indication of the exhumation into the upper crustal level. *Jour. Struct. Geol.*, **33**, 303–322.

Ehara, S., Yanagidani, T. and Terada, M., 1986, AE and thermal expansion of Oshima Granite during slow cycle temperature change between 210 K and 370 K. *Jour. Soc. Mater. Sci. Japan*, **392**, 490–495.

Endo, S. and Yamazaki, T., 2013, Geology of the Ryoke plutono–metamorphic complex in the Tsukude area, central Japan. *Bull. Geol. Surv. Japan*, **64**, 59–84.*

Engebretson, D.C., Cox, A. and Gordon, R.G., 1985, Relative motions between oceanic and continental plates in the Pacific basin. *Geol. Soc. Amer., Spec. Pap.*, 59 p.

Engelder, T., 1979, Mechanisms for strain within the Upper Devonian clastic sequence of the Appalachian Plateau western New York. *Amer. Jour. Sci.*, **279**, 527–542.

Evans, M.A., 1995. Fluid inclusions in veins from the Middle Devonian shales: a record of deformation conditions and fluid evolution in the Appalachian Plateau. *Geol. Soc. Amer. Bull.* **107**, 327–339.

Farver, J. and Yund, R., 2000, Silicon diffusion in a natural quartz aggregate: Constraints on solution-transfer diffusion creep. *Tectonophysics*, **325**, 193–205.

Ferré, E.C., Geissman, J.W., Demory, F., Gattacceca, J., Zechmeister, M.S. and Hill, M.J., 2014, Coseismic magnetization of fault pseudotachylytes: 1. Thermal demagnetization experiments. *Jour. Geophys. Res.*, **119**, B6113–6135.

Fischer, M.P., Higuera–Diaz, I.C., Evans, M.A., Perry, E.C. and Lefticariu, L., 2009. Fracture–controlled paleohydrology in a map–scale detachment fold: insights from the analysis of fluid inclusions in calcite and quartz veins. *Jour. Struct. Geol.*, **31**, 1940–1510.

Gifkins, R.C., 1976, Grain boundary sliding and its accommodation during creep and superplasticity. *Metall. Trans.*, **7A**, 1225–1232.

Groshong, R.H., Jr. 1975, Strain, fractures, and pressure solution in natural single-layer folds. Geol. *Soc. Amer. Bull*,. **86**, 1363–1376.

Hara, I., Sakurai, Y., Okudaira, T., Hayasaka, Y., Ohtomo, Y. and Sakakibara, N., 1991, Tectonics of the Ryoke belt. *98th Ann. Meet. Geol. Soc. Japan, Excursion Guidebook*, 1–20.**

Hara, I., Yamada, T., Yokoyama, S., Arita, M. and Hiraga, Y., 1977, Study on the southern marginal shear belt of the Ryoke metamorphic terrain: Initial movement picture of the Median Tectonic Line. *Earth Sci. (Chikyu Kagaku)*, **31**, 204–217.*

Harayama, S., Koido, Y., Ishizawa, K., Nakai, Y. and Kutsukake, T., 1985, Cretaceous to Paleogene magmatism in the Chubu district, Japan. *Earth Sci. (Chikyu Kagaku)*, **39**, 345–357.*

Harrison, T.M., 1982, Diffusion of ^{40}Ar in hornblende. *Contrib. Mineral. Petrol.*, **78**, 324-331.

Hay, S.J., Hall, J., Simmons, G. and Russell, M.J., 1988. Sealed microcracks in the Lewisian of NW Scotland: a record of 2 billion years of fluid circulation. *Jour. Geol. Soc. Lond.,* **145**, 819–830.

Hayashi, M. and Takagi, H., 1987, Shape fabric of recrystallized quartz in the mylonites along the Median Tectonic Line, southern Nagano Prefecture. *Jour. Geol. Soc. Japan*, **93**, 349–359.*

Heilbronner, R. and Tullis, J., 2006, Evolution of *c* axis pole figures and grain size during dynamic recrystallization: Results from experimentally sheared quartzite. *Jour. Geophys. Res.*, **111**, B10202.

Hickman, S. H. and Evans, B., 1987, Influence of geometry upon crack healing rate in calcite. *Phys. Chem. Mineral.*, **15**, 91–102.

Hippertt, J.F. and Hongn, F.D., 1998, Deformation mechanisms in the mylonite/ultramylonite transition. *Jour. Struct. Geol.*, **20**, 1435–1448.

Hiraga, T., Miyazaki, T., Tasaka, M. and Yoshida, H., 2010, Mantle superplasticity and its self-made demise. *Nature*, **468**, 1901–1094.

Hirth, G., Teyssier, C. and Dunlap, W.J., 2001, An evaluation of quartz flow laws based on comparisons between experimentally and naturally deformed rocks. *Int. Jour. Earth Sci.*, **90**, 77–87.

Hodges, K.V., 2005, Geochronology and thermochronology in orogenic systems. *In*: Rudnick, R.L. (Ed.), *The Crust, Treatise on Geochemistry, Vol. 3, The Crust*. Elsevier-Pergamon, Oxford, 263–292.

Holland, T. and Powell, R., 1991, A Compensated-Redlich-Kwong (CORK) equation for volumes and fugacities of CO_2 and H_2O in the range 1 bar to 50 kbar and 100-1600°C, *Contrib. Mineral. Petrol.*, **109**, 265–273.

Hoshi, H., Kato, D., Ando, Y and Nakashima, K., 2015, Timing of clockwise rortation of Southwest Japan: constraints fro new middle Miocene paleomagnetic results. *Earth Planet Space*, **67**, 92.

Hughes, D.W., 1978, A disaggregation and thin section analysis of the size and mass distribution of the chondrules in the Bjurböle and Chainpur meteorites. *Earth Planet. Sci. Lett.*, **38**, 391–400.

Hurford, A.J., 1986, Cooling and uplift patterns in the Lepontine Alps South Central Switzerland and an age of vertical movement on the Insbric fault line. *Contrib. Mineral. Petrol.*, **93**, 413–427.

Ichikawa, K., 1980, Geohistory of the Median Tectonic Line of Souwthwest Japan. *In*: Ichikawa, K. (Ed.), Median Tectonic Line of Southwest Japan. *Mem. Geol. Soc. Japan*, **18**, 5–24.

Ikeda, T., 1998, Progressive sequence of reactions of the Ryoke metamorphism in the Yanai district, southwest Japan: the formation of cordierite. *Jour. Metamorphic Geol.*, **16**, 39–52.

Ikeda, T., 2002, Regional occurrence of orthopyroxene-bearing basic rocks in the Yanai district, southwest Japan: Evidence for granulite-facies Ryoke metamorphism. *Island Arc*, **11**, 185-192.

Ikeda, T., 2004, Pressure-temperature conditions of the Ryoke metamorphic rocks in Yanai district, SW Japan. *Contrib. Mineral. Petrol.*, **146**, 577-589.

Ishida, K., Kozai, T., Park, S.O. and Mitsugi, T., 2003, Gravel bearing radiolarian as tracers for erosional events: a review of the status of recent research in SW Japan and Korea. *Jour. Asian Earth Sci.*, **21**, 909–920.

Ishihara, S., 1977, The magnetite-series and ilmenite-series granitic rocks. *Mining Geol.*, **27**, 293–305.

Ishihara, S. and Chappell, B.W., 2007, Chemical compositions of the late Cretaceous Ryoke granitoids of the Chubu District, central Japan - Revisited. *Bull. Geol. Surv. Japan*, **58**, 323–350.

Ishise, Y., Kano, S., Sekine, K. and Tsuchiya, N., 2006, Structure of macroscopic fracture and implication for *P*-wave velocity of the Ryoke granitic rocks, Chubu Ryoke belt, Japan. *Min. Mat. Proc. Inst. Japan*, **122**, 56–64.*

Isozaki, Y. Aoki, K, Nakama, T and Yanai, S., 2010, New insight into a subduction-related orogen: A reappraisal of the geo tectonic framework and evolution of the Japanese Islands. *Gondwana Res.*, **18**, 82–105.

Ito, Y. and Miyake, A., 2011, Deformation of Busetsu granites in the Shimoyama area, Toyota city, central Japan. *Nagoya Jour. Space Earth Sci.*, **73**, 19–26.**

Itoh, Y., 1988, Differential rotation of the eastern part of Southwest Japan inferred from paleomagnetism of Cretaceous and Neogene rocks. *Jour. Geophys. Res.*, **93**, 3401–3411.

Jang, B.A. and Kang, S.S., 2011, Mesozoic paleostress from healed microcracks and fluid inclusions in some granites of South Korea. *Geosci. Jour.*, **15**, 161–175.

Jaya, A. and Nishikawa, O., 2013, Paleostress reconstruction from calcite twin and fault-slip data using the multiple inverse method in the East Walanae fault zone: Implications for the Neogene contraction in South Sulawesi, Indonesia. *Jour. Struct. Geol.*, **55**, 34–49.

Jefferies, S.P., Holdsworth, R.E., Shimamoto, T., Takagi, H., Lloyd, G.E. and Spiers, C.J., 2006, Origin and mechanical significance of foliated cataclastic rocks in the cores of crustal-scale faults: Examples from the Median Tectonic Line, Japan. *Jour. Geophys. Res.*, **111**, B12303, 1–17.

Jolly, R.J.H. and Sanderson, D.J., 1995, Variation in the form and distribution of dykes in the Mull swarm, Scotland. *Jour. Struct. Geol.*, **17**, 1543–1557.

Jupp, P.E. and Mardia, K.V., 1980, A general correlation coefficient for directional data and related regression problems. *Biometrika*, **67**, 163–173.

Kashima, N. and Takechi, K., 1996, Fission-track age of tuffs from the Kuma Group, Shikoku, Japan. *Jour. Mineral. Petrol. Sci.*, **91**, 196–200.*

Kawakami, T. and Suzuki, K., 2011, CHIME monazite dating as a tool to detect polymetamorphism in high-temperature metamorphic terrane: Example from the Aoyama area, Ryoke metamorphic belt, Southwest Japan. *Island Arc*, **20**, 439–453.

Kennedy, G.C., Wasserburg, G.J., Heard, H.C. and Newton, R.C., 1962, The upper three-phase region in the system SiO_2 – H_2O. *Amer. Jour. Sci.*, **260**, 501–521.

Kerrick, D.M. and Jacobs, G.K., 1981, A modified Redlich-Kwong equation for H_2O, CO_2 and H_2O-CO_2 mixtures at elevated pressures and temperatures. *Amer. Jour. Sci.*, **281**, 735–767.

Kilian, R., Heilbronner, R. and Stünitz, H., 2011, Quartz grain size reduction in a granitoid rock and the transition from dislocation to diffusion creep. *Jour. Struct. Geol.* **33**, 1265–1284.

Kilsdonk, W. and Wiltschko, D.V., 1988, Deformation mechanisms in the southeastern ramp region of the Pine Mountain block, Tennessee. *Geol. Soc. Amer. Bull.*, **100**, 644–653.

Kinoshita, O., 1995, Migration of igneous activities related to ridge subduction in Southwest Japan and the East Asian continental margin from the Mesozoic to the Paleogene. *Tectonophysics*, **245**, 25–35.

Kobayashi, T., 1941, The Sakawa orogenic cycle and its bearing on the origin of the Japanese Islands. *Jour. Fac. Sci.*, Univ. Tokyo, Series 2, **5**, 219–578.

Kojima, S., Tsukada, K., Otoh, S., Yamakita, S., Ehiro, M., Dia, C., Kirillova, G.L., Dymovich, V.A. and Eichwald, L.P., 2008, Geological relationship between Anyui Metamorphic Complex and Samarka terrane, Far, East Russia. *Island Arci*, **17**, 502–516.

Kong, M., Bhattacharya, R.N, James, C. and Basu, A., 2005, A statistical approach to estimate the 3D size distribution of spheres from 2D size distributions. *Geol. Soc. Amer. Bull.*, **117**, 244–249.

Kowallis, B.J., Wang, H.F. and Jang, B.A., 1987, Healed microcrack orientations in granite from Illinois borehole UPH-3 and their relationship to the rock's stress history. *Tectonophysics*, **26**, Suppul., 345–356.

Kranz, R.L., 1983, Microcracks in roks: A review. *Tectonophysics,* **100**, 449–480.

Kubota, Y., 2015, Kinematic history of the Tobe and Ishizuchi Phases along the MTL, inferred from deformation structure of the Tobe Thrust, Ehime Prefecture, Japan. *Eng. Geol. Japan*, **5**, 61–66.**

Kubota, Y. and Takeshita, T., 2008, Paleocene large-scale normal faulting along the Median Tectonic Line, western Shikoku, Japan. *Island Arc*, **17**, 129–151.

Lacassin, R., 1987, Kinematics of ductile shearing from outcrop to crustal scale in the Monte Rosa Nappe, Western Alps. *Tectonics*, **6**, 69–88.

Lander, R.H. and Laubach, S.E., 2014, Insights into rates of fracture growth and sealing from a model for quartz cementation in fractured sandstones. *Geol. Soc. Amer. Bull.*, **127**, 516–538.

Laubach, S.E., 2003, Practical approaches to identifying sealed and open fractures. *AAPG Bull.*, **87**, 561–579.

Laubach, S.E. and Diaz-Tushman, K., 2009, Laurentian palaeostress trajectories and ephemeral fracture permeability, Cambrian Eriboll Formation sandstones west of the Moine Thrust Zone. *Jour. Geol. Soc. Lond.*, **166**, 349–362.

Laubach, S.E., Reed, R.M., Olson, J.E., Lander, R.H. and Bonnell, L.M., 2004, Coevolution of crack-seal texture and fracture porosity in sedimentary rocks: Cathodoluminescence observations of regional fractures. *Jour. Struct. Geol.*, **26**, 967–982.

Lespinasse, M., 1999, Are fluid inclusion planes useful in structural geology? *Jour Struct. Geol.* **21**, 1237–1243.

Lespinasse, M. and Pecher, A., 1986, Microfracturing and regional stress field: a study of the preferred orientations of fluid–inclusion planes in a granite from the Massif Central, France. *Jour. Struct. Geol.*, **8**, 169–180.

Lister, G.S. and Hobbs, B.E., 1980, The simulation of fabric development during plastic deformation and its application to quartzite: the influence of deformation history. *Jour. Struct. Geol.*, **2**, 355–370.

Lloyd, G.E., Law, R.D. and Schmid, S.M., 1987, A spherical electron channelling pattern map for use in quartz petrofabric analysis: correction and verification. *Jour. Struct. Geol.*, **9**, 251–253.

Mainprice, D., Bouchez, J.L., Blumenfeld., Blumenfeld, P. and Tabia, J.M., 1986, Dominant *c* slip in naturally deformed quartz: Implications for dramatic plastic softening at high temperature. *Geology*, **14**, 819–822.

Mardia, K.V., 1976, Linear–circular correlation coefficients and rhythmometry. *Biometrika*, **63**, 403–405.

Mardia, K.V. and Jupp, P.E., 1999, Directional Statistics. Academic Press Inc., London, 429p.

Marinoni, L.B., 2001, Crustal extension from exposed sheet intrusions: Review and method proposal. *Jour. Volcanol. Geoth. Res.*, **107**, 27–46.

Maruyama, S., Isozaki, Y., Kimura, G. and Terabayashi, M., 1997, Paleogeographic maps of the Japanese Islands: plate tectonic synthesis from 750 Ma to the present. *Island Arc*, **6**, 121–142.

Maruyama, S. and Seno, T., 1986, Orogeny and relative plate motions: example of the Japanese Islands. *Tectonophysics*, **127**, 305–329.

Michibayashi, K., Makino, T. and Yoshida, S., 1997, “Xenolith windows”: intensely deformed mylonites entrained in the Tenryukyo granite, the Ryoke belt, central Honshu, Japan. *Jour. Geol. Soc. Japan*, **103**, 1053–1064.

Michibayashi, K. and Masuda, T., 1993, Shearing during progressive retrogression in granitoids: abrupt grain size reduction of quartz at the plastic-brittle transition for feldspar. *Jour. Struct. Geol.*, **15**, 1421–1432.

Miyake, A., Hirukawa, T., Sato, M., Taguchi, T., Suzuki, K. and Nakai, Y., 2016, Large thermal aureole around the Inagawa Granodiorite in the southeastern area of Asuke, Aichi Prefecture. *Jour. Geol. Soc. Japan*, **122**, 173–191.*

Miyata, T., Hirota, Ui. and Ichikawa, K., 1980, Paleogene left-lateral wrenching on the Median Tectonic Line in Southwest Japan, *Mem. Geol. Soc. Japan.,* **18**, 51–68.

Miyazaki, K., 2010, Development of migmatites and the role of viscous segregation in high-*T* metamorphic complexes: example from the Ryoke Metamorphic Complex, Mikawa Plateau, Central Japan. *Lithos*, **116**, 287–299.

Morishita, T. and Suzuki, K., 1995, CHIME ages of monazite from the Shinshiro Tonalite of the Ryoke belt in the Mikawa area, Aichi Prefecture. *Jour. Earth Planet. Sci. Nagoya Univ.*, **42**, 45–53.

Müller, R.D., Seton, M., Zahirovic, S., Williams, S.E., Matthews, K.J., Wright, N.M., Shephard, G.E., Maloney, K.T., Barnett-Moore, N., Hosseinpour, M., Bower, D.J. and Cannon, J., 2016, Ocean basin evolution and global-scale plate reorganization events since Pangea breakup. A*nnu. Rev. Earth Planet. Sci.,* **44**, 107–138.

Murakami, M., Košler, J., Takagi, H. and Tagami, T., 2006a, Dating pseudotachylyte of the Asuke Shear Zone using zircon fission-track and U-Pb methods. *Tectonophysics*, **424**, 99–107.

Murakami, M., Yamada, R. and Tagami, T., 2006b, Short-term annealing characteristics of spontaneous fission track in zircon: A qualitative description. *Chem. Geol.*, **227**, 214-222.

Nadan, B.J. and Engelder, T., 2009. Microcracks in New England granitoids: a record of thermoelastic relaxation during exhumation of intracontinental crust. *Geol. Soc. Amer. Bull.*, **121**, 80–99.

Nakai, Y., 1976, Petrographical and petrochemical studies of the Ryoke granites in the Mikawa - Tono district, central Japan. *Bull. Aichi Univ. Educ.* (*Nat. Sci.*), **25**, 97–112.

Nakai, Y. and Suzuki, K., 1996, CHIME monazite ages of the Kamihara Tonalite and the Tenryukyo Granodiorite in the eastern Ryoke belt of central Japan. *Jour. Geol. Soc. Japan*, **102**, 431–439.

Nakai, Y. and Suzuki, K., 2003, Post-tectonics two-mica granite in the Okazaki area, central Japan. *Hutton Symp. V, Field guidebook, Geol. Surv. Japan*, *Interim-Rep*. **28**, 115–124.

Nakajima, T., 1994, The Ryoke plutonometamorphic belt: crustal section of the Cretaceous Eurasian continental margin. *Lithos*, **33**, 51–66.

Nakajima, T., 1996, Cretaceous granitoids in SW Japan and their bearing on the crust-forming process in the eastern Eurasian margin. *Trans. Roy. Soc. Edinburgh: Earth Sci.*, **87**, 183–191.

Nakajima, T., Takahashi, M., Imaoka, T. and Shimura, T., 2016, Granitic rocks. *In:* Moreno, T., Wallis, S.R., Kojima, T. and Gibbons, W. (Eds.) *The Geology of Japan*. Geol. Soc., Lond., 251–272.

Nakamura, K., 1977, Volcanoes as possible indicators of tectonic stress orientation - principle and proposal. *Jour. Volcanol. Geoth. Res.*, **2**, 1–16

Nara, Y. and Kaneko, K., 2006, Dependence of the propagation of microcracks in rock on the environmental conditions, *Proc. 35th Symp. Rock Mech.*, **35**, 307–312.*

Narita, K., Yamaji, A., Tagami, T., Kurita, H., Obuse, A. and Matsuoka, K., 1999, Depositional age of the Tertiary Kuma Group, Shikoku, and its significance. *Jour. Geol. Soc. Japan*, **105**, 305–308.*

Navabpour, P., Angelier, J. and Barrier, E., 2010, Mesozoic extensional brittle tectonics of the Arabian passive

margin, inverted in the Zagros collision (Iran, Interior Fars). *In*: Leturmy, P. and Robin, C. (Eds), *Tectonic and Stratigraphic Evolution of Zagros and Makran during the Mesozoic–Cenozoic*. Geol. Soc. Lond. Spec. Publ., **330**, 65–96.

Nishiwaki, H. and Okudaira, T., 2007, Emplacement process of the Hatsuse plutonic complex, central Kinki Province, SW Japan. *Jour. Geol. Soc. Japan*, **113**, 223–239.*

Okada, A., 1973, Quaternary faulting along the Median Tectonic Line in the central part of Shikoku. *Geogr. Rev. Japan*, **46**, 295–322.*

Okada, A., 2012, Research on Quaternary faulting history and long-term seismic evaluation of the Median Tectonic Line (MTL) fault zone in southwest Japan. *Quatern. Res.*, **51**, 131–150.*

Okudaira, T., Beppu, Y., Yano, R., Tsuyama, M. and Ishii, K., 2009, Mid-crustal horizontal shear zone in the forearc region of the mid-Cretaceous SW Japan arc, inferred from strain analysis of rocks within the Ryoke metamorphic belt. *Jour. Asian Earth Sci.*, **35**, 34–44.

Okudaira, T., Hara, I., Sakurai, Y. and Hayasaka, Y., 1993, Tectono-metamorphic processes of the Ryoke belt in the Iwakuni-Yanai district, southwest Japan. *Mem. Geol. Soc. Japan*, **42**, 91–120.

Okudaira, T., Hayasaka, Y., Himeno, O., Watanabe, K., Sakurai, Y. and Ohtomo, Y., 2001, Cooling and inferred exhumation history of the Ryoke metamorphic belt in the Yanai district, south-west Japan: Constraints from Rb–Sr and fission-track ages of gneissose granitoid and numerical modeling. *The Island Arc*, **10**, 98–115.

Okudaira, T. and Shigematsu, N., 2012, Estimates of stress and strain rate in mylonites based on the boundary between the fields of grain-size sensitive and insensitive creep. *Jour. Geophys. Res.*, **117**, B03210.

Okudaira, T. and Suda, Y., 2011, Cretaceous events at the eastern margin of East Asia recorded in rocks of the Ryoke Belt, SW Japan. *Jour. Tokyo Geogr. Soc.*, **120**, 452–465.*

Okudaira, T., Takeshita, T., Hara, I. and Ando, J., 1995, A new estimate of the conditions for transition from basal <*a*> to prism [*c*] slip in naturally deformed quartz. *Tectonophysics*, **250**, 31–46.

Onstott, T.C., 1980, Application of the Bingham distribution function in paleomagnetic studies. *Jour. Geophys. Res.*, **85**, 1500–1510.

Osozawa, S. and Pavlis, T., 2007, The high P/T Sambagawa extrusional wedge, Japan. *Jour. Struct. Geol.*, **29**, 1131–1147.

Otofuji, Y., Enami, R., Yokoyama, M., Kamiya, K., Kuma, S. and Saito, H., 1999, Miocene clockwise rotation of southwest Japan and formation of curvature of the Median Tectonic Line: Paleomagnetic implications. *Jour. Geophys. Res.*, **104**, 12895–12907.

Otofuji, Y., Matsuda, T. and Nohda, S., 1985, Opening mode of the Japan Sea inferred from the palaeomagnetism of the Japan Arc. *Nature*, **317**, 603–604.

Padovani, E.R., Shirey, S.B. and Simmons, G., 1982, Characteristics of microcracks in amphibolite and granulite facies grade rocks from southeastern Pennsylvania. *Jour. Geophys. Res.*, **87**, 8605–8630.

Passchier, C.W. and Trouw, R.A.J., 2005, *Microtectonics*. Springer, Berlin, 366p.

Pecher, A., 1989, SCHMIDTMAC: A program to display and analyze directional data. *Comput. Geosci.*, **15**, 1315–1326.

Plumb, R., Engelder, T. and Yale, D., 1984, Near surface in situ stress: 3. Correlation with microcrack fabric within the New Hampshire Granite. *Jour. Geophys. Res*., **89**, 9350–9364.

Ranalli, G., 1984, Grain size distribution and flow stress in tectonites. *Jour. Struct. Geol.*, **6**, 443–447.

Randive, K., Hari, K.R., Dora, M.L. and Maple, D.B., 2014, Study of fluid inclusions: methods, techniques and applications. *Gond. Geol. Mag.*, **29**, 19–28.

Robin, P.Y.F. and Jowett, E.C., 1986, Computerized density contouring and statistical evaluation of orientation data using counting circles and continuous weighting functions. *Tectonophysics*. **121**, 207–223.

Roedder, E., 1962, Ancientfluids in crystals. *Sci. Amer*., **207**, 38–47.

Roedder, E., 1983, Geobarmetry of ultramafic xenoliths from Loihi Seamount, Hawaii, on the basis of CO_2 inclusions in olivine. *Earth Planet. Sci. Lett.*, **66**, 369–379.

Roedder, E., 1984, *Fluid Inclusions*. Reviews in Mineralogy, **12**, *Min. Soc. Amer, Washington D.C.,* pp. 646.

Rowe, K.J. and Rutter, E.H., 1990, Paleostress estimation using calcite twinning: experimental calibration and application to nature. *Jour. Struct. Geol.*, **12**, 1–17.

Rutter, E.H., 1976, The kinetics of rock deformation by pressure solution. *Phil. Trans. R. Soc. Lond.*, **140**, 725–740.

Rutter, E.H. and Brodie, K.H., 1988, The role of tectonic grain size reduction in the rheological stratification of the lithosphere. *Jour. Geol. Rundsch*, **77**, 295–308.

Rutter, E.H. and Brodie, K.H., 2004, Experimental grain size-sensitive flow of hot-pressed Brazilian quartz aggregates. *Jour. Struct. Geol.*, **26**, 2011–2023.

Ryoke Research Group, 1972, The mutual relations of the granitic rocks of the Ryoke metamorphic belt in central Japan. *Earth Sci. (Chikyu Kagaku)*, **26**, 205–216.*

Saintot, A., Stephens, M.B., Viola, G. and Nordgulen, Ø., 2011, Brittle tectonic evolution and paleostress field reconstruction in the southwestern part of the Fennoscandian Shield, Forsmark, Sweden. *Tectonics*, **30**, TC4002.

Sakaguchi, A., Sakaguchi, H., Nishimura, D., Nakatani, M. and Yoshida, S., 2011, Elastic stress indicaton in elastically rebounded rock. *Geophys. Res. Lett.*, **38**, L09316.

Sakakibara, N., 1996, Qualitative estimation of deformation temperature and strain from microstructure and lattice preferred orientation in plastically deformed quartz aggregates. *Jour. Geol. Soc. Japan*, **102**, 199–210.*

Sakakibara, N., Hara, I., Kanai, K., Kaikiri, K., Shiota, T., Hide, K. and Paulitsch, P., 1992, Quartz microtextures of the Sambagawa schists and their implications in convergent margin processes. *Island Arc*, **1**, 186–197.

Sakamaki, H, Shimada, K. and Takagi, H., 2006, Selective generation surface of pseudotachylyte − example

from the Asuke Shear Zone, SW Japan − . *Jour. Geol. Soc. Japan*, **112**, 519–530.*

Sakashima, T., Terada, K., Takeshita, T. and Sano, Y., 2003, Large-scale displacement along the Median Tectonic Line, Japan: evidence from SHRIMP zircon U–Pb dating of granites and gneisses from the South Kitakami and paleo-Ryoke belts. *Jour. Asian Earth Sci*., **21**, 1019–1039.

Sander, M.V. and Black, J.E., 1988, Crystallization and recrystallization of growth-zoned vein quartz crystals from epithermal systems: Implications for fluid inclusion studies. *Econ. Geol.,* **83**, 1052–1060.

Sangawa, A., 1977, Geomorphic development and crustal movement of the middle course basin of the Kinokawa River. *Geogr. Rev. Japan*, **46**, 578–595.*

Sasao, E., Danhara, T., Iwano, H. and Hayashi, J., 2011, Fission track ages of the Miocene Mizunami and Iwamura Group in southeastern Gifu Prefecture, Central Japan. *Jour. Geol. Soc. Japan*, **117**, 476–481.*

Sato, K., 2006, Incorporation of incomplete fault-slip data into stress tensor inversion. *Tectonophysics*, **421**, 319–330.

Sato, K., 2010a, Hough Transform Inverse Method Main Processor, Version 1.10. Division of Earth and Planetary Sciences, Kyoto University, Kyoto.

Sato, K., 2010b, Peak Picker, Version 1.01. Division of Earth and Planetary Sciences, Kyoto University, Kyoto.

Sato, T. and Takagi, H., 2010, Paleostress history estimated from preferred orientation of microcracks in the Tanzawa tonalite body, central Japan and its relationship to the Honsyu arc – Izu arc collision. *Jour. Geol. Soc. Japan*, **116**, 309–320.*

Sawaki, T., 2003, Fluid inclusions - Basics and recent studies -. *Japan. Mag. Mineral. Petrol. Sci.*, **32**, 23–41.*

Schmid, S.M. and Casey, M., 1986, Complete fabric analysis of some commonly observed quartz c-axis patterns, *In*: Hobbs, B.E. and Heard, H.C (Eds.), *Mineral and Rock Deformation: Laboratory Studies*. Geophys. Monogr. Ser., **36**, AGU, Washington, D.C., 263–286.

Schwarz, G., 1978, Estiating the dimension of a model. *Ann. stat.*, **6**, 461–464.

Shibata, K., Nakajima, T., Sangawa, A., Uchiumi, S. and Aoyama, H., 1989, K-Ar ages of fault gouges from the Median Tectonic Line in Shikoku. *Bull. Geol. Surve. Japan*, **40**, 661–671.

Shibata, K. and Nozawa, T., 1968, K-Ar age of Ominesan acid rocks, Kishu, Japan. *Bull. Geol. Surv. Japan*, **19**, 219–222.

Shibata, K., Sugiyama, Y., Takagi, H. and Uchiumi, S., 1988, Isotopic ages of rocks along the Median Tectonic Line in the Yoshino area, Nara Prefecture. *Bull. Geol. Surv. Japan*, **39**, 759–781.*

Shibata, K. and Takagi, H., 1988, Isotopic ages of rocks and intrafault materials along the Median Tectonic Line: An example in the Bungui-toge area, Nagano Prefecture. *Jour. Geol. Soc. Japan*, **94**, 35–50.*

Shibata, K. and Uchiumi, S., 1992, K-Ar age results-4: New data from the Geological Survey of Japan. *Bull. Geol. Surv. Japan*, **43**, 359–367.*

Shibata, K., Uchiumi, S. and Nakagawa, T., 1979, K-Ar age results – 1. *Bull. Geol. Surv. Japan*, **30**, 675–686.*

Shimada, K., Takagi, H. and Osawa, H., 1998, Geotectonic evolution in transpressional regime: time and space

relationship between mylonitization and folding in the southern Ryoke belt, eastern Kii Peninsula, southwest Japan. *Jour. Geol. Soc. Japan*, **104**, 825–844.*

Simmons, G. and Richter, D., 1976, Microcracks in rock. *In*: Strens, R.G.J. (Ed.), *The Physics and Chemistry of Minerals and Rocks*. Wiley, New York, 105–137.

Skemer, P., Katayama, I., Jiang, Z. and Karato, S., 2005, The misorientation index: Development of a new method for calculating the strength of lattice-preferred orientation. *Tectonophysics*, **411**, 157–167.

Smith, D. L. and Evans, B., 1984, Diffusional crack healing in quartz. *Jour. Geophys. Res.*, **89**, 4125–4135.

Sprunt, E.S. and Nur, A., 1979, Microcracking and healing in granites: New evidence from cathodoluminescence. *Science*, **205**, 495–497.

Stipp, M., Stünitz, H., Heilbronner, R. and Schmid, S.M., 2002, Dynamic recrystallization of quartz: correlation between natural and experimental conditions. *In*: De Meer, S., Drury, M.R., De Bresser, J.H.P. and Pennock, G.M. (Eds.), *Deformation Mechanisms, Rheology and Tectonics: Current Status and Future Perspectives*. Geological Society, London, Special Publications, **200**, 171–190.

Stipp, M. and Tullis, J., 2003, The recrystallized grain size piezometer for quartz. *Geophys. Res. Lett.*, **30**, 2088.

Stöckhert, B., Brix, M.R., Kleinschrodt, R., Hurford, A.J. and Wirth, R., 1999, Thermochronometry and microstructures of quartz: A comparison with experimental flow laws and predictions on the temperature of the brittle-plastic transition. *Jour. Struct. Geol.*, **21**, 351–369.

Suyari, K. and Akojima, I., 1974, On some problems of the Median Line in Shikoku. *Jour. Sci. Coll. Gen. Educ. Univ. Tokushima*, **7**, 25–42.

Suzuki, K. and Adachi, M., 1998, Denudation history of the high T/P Ryoke metamorphic belt, southwest Japan: constrains from CHIME monazite ages of gneisses and granitoids. *Jour. Metamorphic. Geol.*, 16, 23–37.

Suzuki, K., Adachi, M. and Kajizuka, I., 1994a, Electron microprobe observations of Pb diffusion in metamorphosed detrital monazites. *Earth Planet. Sci. Lett.*, **128**, 391-405.

Suzuki, K., Adachi, M. and Nureki, T., 1996, CHIME age dating of monazites from metamorphic rocks and granitic rocks of the Ryoke belt in the Iwakuni area, Southwest Japan. *Island Arc*, **5**, 43–55.

Suzuki, K., Morishita, T., Kajizuka, I., Nakai, Y., Adachi, M. and Shibata, K., 1994b, CHIME ages of monazites from the Ryoke metamorphic rocks and some granitoids in the Mikawa-Tono area, central Japan. Bull. Nagoya Univ. Furukawa Museum, 10, 17–38.*

Suzuki, K., Nasu, T. and Shibata, K., 1995, CHIME monazite ages of the Otagiri and Ichida Granites in the Komagane area, Nagano Prefecture. *Jour. Earth Planet. Sci, Nagoya Univ.*, **42**, 17–30.

Tagami, T., Galbraith, R.F., Yamada, R. and Laslett, G.M., 1998, Revised annealing kinetics of fission tracks in zircon and geological implications. *In*: Van den Haute, P., De Corte, F. (Eds.), *Advances in Fission-Track Geochronology*. Kluwer Academic Publishers, Dordrecht, The Netherlands, 99–112.

Taira, A., Ohara, Y., Wallis, S.R., Ishiwatari, A. and Iryu, Y., 2016, Geological evolution of Japan: an overview. *In:* Moreno, T., Wallis, S.R., Kojima, T. and Gibbons, W. (Eds.) *The Geology of Japan*. Geol. Soc., Lond.,

1–24.

Takagi, H., 1984, Mylonitic rocks along the Median Tectonic Line in Takato-Ichinose area, Nagano Prefecture. *Jour. Geol. Soc. Japan*, **90**, 81–100.*

Takagi, H., 1985, Mylonitic rocks of the Ryoke belt in the Kayumi area, eastern part of the Kii Peninsula. *Jour. Geol. Soc. Japan*, **91**, 637–651.*

Takagi, H., 1986, Implications of mylonitic microstructures for the geotectonic evolution of the Median Tectonic Line, central Japan. *Jour. Struct. Geol.*, **8**, 3–14.

Takagi, H., 1997, Timing of mylonitization in Ryoke belt, Chubu region., *Chikyu Monthly*, **19**, 111–116.**

Takagi, H., Miwa, S., Yamada, T., Nishijima, K., Yamazaki, S. and Enjoji, M., 2012, Estimation of paleostress field from 3-D orientation distribution of microcracks and their geothermal conditions in the Cretaceous granitic rocks in the northern Awaji Island, central Japan. *Jour. Geol. Soc. Japan*, **118**, 571–581.*

Takagi, H., Miwa, S., Yokomizo, Y., Nishijima, K., Enjoji, M., Mizuno, T. and Amano, K., 2008, Estimation of the paleostress field from 3-D orientation distribution of microcracks and their geothermal conditions in the Toki Granite, central Japan. *Jour. Geol. Soc. Japan*, **114**, 321–335.*

Takagi, H. and Shibata, K., 1992, K-Ar dating of fault gouge: Examples along the Median Tectonic Line. *Mem. Geol. Surv. Japan*, **40**, 31–38.*

Takagi, H., Shibata, K., Sugiyama, Y., Uchiumi, S. and Matsumoto, A., 1989, Isotopic ages of rocks along the Median Tectonic Line in theKayumi area, Mie Prefecture. *Jour. Mineral. Petrol. Sci.*, **84**, 75–88.*

Takagi, H., Shibata, K. and Uchiumi, S., 1991, K-Ar ages of fault gouges and felsite dykes from the Median Tectonic Line in Chubu Region, central Japan. *Jour. Geol. Soc. Japan*, **5**, 377–384.*

Takagi, H., Shimada, K., Iwano, H. and Danhara, T., 2010, Oldest record of brittle deformation along the Median Tectonic Line: fission-track age for pseudotachylyte in the Taki area, Mie Prefecture. *Jour. Geol. Soc. Japan*, **116**, 45–50.

Takagi, H., Takeshita, T., Shibata, K., Uchiumi, S. and Inoue, M., 1992, Middle Miocene normal faulting along the Tobe Thrust in western Shikoku. *Jour. Geol. Soc. Japan*, **98**, 1069–1072.**

Takahashi, J., 1992, Faulting history of the Median Tectonic Line in Ehime Prefecture. *Mem. Geol. Soc. Japan*, **40**, 99–112.*

Takahashi, M. and Saito, K., 1997, Miocene intra-arc bending at an arc–arc collision zone, central Japan. *Island Arc*, **6**, 168–182,

Takahashi, Y., 1993, Al in hornblende as a potential geobarometer for granitoids: a review. *Bull. Geol. Surv. Japan*, **44**, 597–608.*

Takemura, T. and Oda, M., 2002, Three-dimensional fabric analysis of microcracks associated with brittle failure of granitic rocks. *Jour. Geol. Soc. Japan*, **108**, 453–464.*

Takenouchi, S., 1975, Basic knowledge on studies of fluid inclusions in minerals – 1. *Jour. Gemmol. Soc. Japan*, **2**, 25–33.*

Takeshita, T., 1995, Dynamic analysis of deformed quartz grains from the folded Middle Miocene Momonoki Subgroup of central Japan: origin of healed microcracks. *Tectonophysics*, **245**, 277–297.

Takeshita, T., 1996, Estimate of the physical conditions for deformation based on *c*-axis abric transitions in naturally deformed quartzite. *Jour. Geol. Soc. Japan*, **102**, 211–222.*

Takeshita, T., 2010, Tectonics in the forearc region of central and SW Japan during the Japan Sea opening. *Jour. Tokyo Geogr. Soc*., **119**, 347–361.*

Takeshita, T. and Hara, I., 1998, *c*-Axis fabrics and microstructures in a recrystallized quartz vein deformed under fluid-rich greenschist conditions. *Jour. Struct. Geol.*, **20**, 417–431.

Takeshita, T., Tanaka, H. and Itaya, T., 2000, K-Ar ages of the 'Ishizuchiyama Tertiary System' in western Shikoku, Japan, and their implications. *Jour. Geol. Soc. Japan*, **106**, 308–311.*

Takeshita, T. and Wenk, H.R., 1988, Plastic anisotropy and geometrical hardening in quartzites. *Tectonophysics*, **149**, 345–361.

Takeshita, T. and Yagi, K., 2001, Paleostress orientation from 3–D orientation distribution of microcracks in quartz from the Cretaceous granodiorite core samples drilled through the Nojima Fault, south–west Japan. *Island Arc*, **10**, 495–505.

Takeuchi, S., Saegusa, H., Amano, K. and Takeuchi, R., 2013, Hydrogeological characterization of deep subsurface structures at the Mizunami Underground Research Laboratory. *Jour. Geol. Soc. Japan*, **119**, 75–90.*

Tanaka, H., Saka, Y., Abe, T., Kohama, S. and Itaya, T., 1992, Fault gouges and their K-Ar ages from the Akaishi Tectonic Line, central Japan. *Jour. Geol. Soc. Japan*, **98**, 39–48.*

Tanaka, H., Takagi, H. and Inoue, M, 1996, Mode of cataclastic deformation and hydrothermal alteration of the fault rocks and history of fault activity along the Median Tectonic Line, central Japan. *Jour. Tectonic Res. Group Japan*, **41**, 31–44.*

Tatsumi, Y., Tani, K., Sato, K., Danhara, T., Hyodo, H., Kawabata, H., Hanyu, T. and Dunkly D.J., 2010, Multi-chronology of volcanic rocks leading to reliable age estimates of volcanic activity: An example from the Setouchi volcanic rocks on Shodo-Shima Island, SW Japan. *Jour. Geol. Soc. Japan*, **116**, 661–679.*

Tazaki, K., Takahashi, J., Itaya, T., Grapes, R.H. and Kashima, N., 1990, K-Ar ages of the andesites in truding along the Median Tectonic Line in northwestern Shikoku, Japan. *Jour. Mineral. Petrol. Sci.*, **85**, 155–160.*

Techmer, K.S., Ahrendt, H. and Weber, K., 1992, The development of pseudotachylyte in the Ivrea-Verbano Zone of the Italian Alps. *Tectonophysics*, 204, 307–322.

Terzaghi, R.D., 1965, Source of error in joint surveys. *Geotéchnique*, **15**, 287–304.

Tibshirani, R., Walther, G. and Hastile, T., 2001, Estimating the number of clusters in a data set via the gap statistic. *Jour. R. Stat. Soc. B*, **62**, 411–423.

Tödheide, K., 1972, Water at high temperature and pressure. *In*: Franks, F. (Ed), *Water: a comprehensive treatise*, Plenum Press, New York, 463-514.

Tullis, J. and Yund, R.A., 1982, Grain-growth kinetics of quartz and calcite aggregates. *Jour. Geol.*, **90**, 301–318.

Tullis T.E., 1989, Development of preferred orientation due to anisotropic dissolution/growth rates during solution transfer creep. *Eos, Trans. Amer Geophys. Un.*, **70**, 457.

Turner, F.J., 1953, Nature and dynamic interpretation of deformation lamellae in calcite of three marbles. *Amer. Jour. Sci.*, **251**, 276–298.

Turner, F.J., 1962, “Compression” and “tension” axes deducted from {0112} twinning in calcite. *Jour. Geophys. Res.*, **67**, 1660.

Tuttle, O.F., 1949, Structural petrology of planes of liquid inclusions. *Jour. Geol.*, **57**, 331–356.

Twiss, R. J., 1977, Theory and applicability of a recrystallized grain size paleopiezometer. *Pageoph.*, **115**, 227–244.

Uchiumi, S., Uto, K. and Shibata, K., 1990, K-Ar age results – 3: New data from the Geological Survey of Japan. *Bull. Geol. Surv. Japan*, **42**, 567–575.*

Underwood, E., 1973, Quantitative stereology for microstructural analysis. *In*: McCall, J. and Mueller, W.M. (Eds), *Microstructural Analysis - Tools and Techniques*. Springer US, 35–66.

Uyeda, S. and Miyashiro, A., 1974, Plate tectonics and the Japanese Islands: a synthesis. *Geol. Soc. Amer. Bull.*, **85**, 1159–1170.

Vollbrecht, A., Susanne, R. and Weber, K., 1991, Development of microcracks in granites during cooling and uplift: examples from the Variscan basement in NE Bavaria, Germany. *Jour. Struct. Geol.*, **13**, 787–799.

Wakita, K., 2013, Geology and tectonics of Japanese islands: A review - The key to understanding the geology of Asia. *Jour. Asian Earth Sci.*, **72**, 75–87.

Wallace, R.E., 1951, Geometry of shearing stress and relation to faulting. *Jour. Geol.*, **59**, 118–130.

Wallis, S.R. and Okudaira, T., 2016, Paired metamorphic belts of SW Japan: the geology of the Sanbagawa and Ryoke metamorphic belts and the Median Tectonic Line. *In:* Moreno, T., Wallis, S.R., Kojima, T. and Gibbons, W. (Eds.) *The Geology of Japan*. Geol. Soc., Lond., 101–124.

Weiss, L.E., 1954, A study of tectonic style: structural investigation of a marble quartzite complex in southern California. *Univ. Calif. Publ. Geol. Sci.*, **30**, 1–102.

White, S., 1977, Geological significance of recovery and recrystallization processes in quartz. *Tectonophysics*, **39**, 143–170.

Wightman, R.H., Prior, D.J. and Little, T.A., 2006, Quartz veins deformed by diffusion creep-accommocated grain boundary sliding a transient, high strain-rate event in the Southern Alps, New Zealand. *Jour. Struct. Geol.*, **28**, 902–918.

Yamada, N., Katada, M., Hayama, Y., Yamada, T., Nakai, Y., Kutsukake, T., Suwa, K. and Miyakawa, K., 1974, Geological map of the Ryoke Belt, central Japan, 1:200,000, Miscellaneous Map Series, 18, Geol. Surv. Japan.

Yamada, N., Shibata, K., Tsukuda, E., Uchiumi, S., Matsumoto, A., Takagi, H. and Akahane, H., 1992, Radiometric ages of igneous rocks around the Atera Fault, central Japan, with special reference to the age of activity of the Atera Fault. *Bull. Geol. Surv. Japan*, **43**, 759–779.*

Yamaji, A., 2000, The multiple inverse method: a new technique to separate stress from heterogeneous fault-slip data. *Jour. Struct. Geol.*, **22**, 441–452.

Yamaji, A., 2012, A historical review of the methods for inferring paleostresses from dike orientations. *Jour. Geol. Soc. Japan*, **118**, 335-350.*

Yamaji, A., 2015, How tightly does calcite *e*-twin constrain stress. *Jour. Struct. Geol.*, **72**, 83–95.

Yamaji, A., 2016, Genetic algorithm for fitting a mixed Bingham distribution to 3D orientations: a tool for the statistical and paleostress analyses of fracture orientations. *Island Arc*, **25**, 72–83.

Yamaji, A., Otsubo, M. and Sato, K., 2006, Paleostress analysis using the Hough transform for separating stresses from heterogeneous fault-slip data. *Jour. Struct. Geol.*, **28**, 980–990.

Yamaji, A. and Sato, K., 2011, Clustering of fracture orientations using a mixed Bingham distribution and its application to paleostress analysis from dike or vein orientations. *Jour. Struct. Geol.*, **33**, 1148–1157.

Yamaji, A., Sato, K. and Tonai, S., 2010, Stochastic modeling for the stress inversion of vein orientations: Paleostress analysis of Pliocene epithermal veins in southwestern Kyushu Japan. *Jour. Struct. Geol.*, **32**, 1137–1146.

Yamakita, S. and Otoh, S., 2000, Cretaceous rearrangement processes of pre-Cretaceous geologic units of the Japanese Islands by MTL-Kurosegawa left-lateral strike-slip fault system. *Mem. Geol. Soc. Japan*, **56**, 23–38.*

Yamasaki, S. and Umeda, K., 2012, Cooling history of the Cretaceous Toki granite in the eastern Sanyo Belt, Central Japan. *Japan. Mag. Mineral. Petrol. Sci.*, **41**, 39–46.*

Yamasaki, T., 2013, K-Ar ages of the Ryoke plutonic rocks in the Asuke area, Aichi prefecture, central Japan. *Jour. Geol. Soc. Japan*, **119**, 421–431.*

Yamasaki, T. and Ozaki, M., 2012, Geology of the Asuke District. *Quadrangle Series, 1:50,000, Geological Survey of Japan, AIST*, 76p.**

Yehara, S., 1936, On the echelon structures of Shikoku and the origin of Japanese arcs. *Japan. Jour. Geol. Geograph.*, **13**, 1–24.

Yoshida, H., Ohsawa, H., Yanagizawa, K. and Yamakawa, M., 1989, Analysis of fracture system in granitic rock: Case study for the granitic rock, Gifu Prefecture, Japan. *Jour. Japan Soc. Eng. Geol.*, **30**, 11–22.*

Yuguchi, T., Amano, K., Tsuruta, T., Danhara, T. and Nishiyama, T., 2011, Thermochronology and the three-dimensional cooling pattern of a granitic pluton: An example from the Toki granite, Central Japan., *Contrib. Mineral Petrol.*, **162**, 1063–1077.

Yuhara, M., 2011, Trace and rare earth elements compositions of the Takato Granite in the Ina district of the Ryoke Metamorphic Belt, Southwest Japan Arc. *Fukuoka Univ. Sci. Rep.*, **41**, 207–215.*

Zoback, M.L., 1992, First- and second-order patterns of stress in the lithosphere: the world stress map project. *Jour. Geophys. Res.*, **97**, 11703–11728.

*in Japanese with English abstract

**in Japanese

Publications

Kanai, T., Yamaji, A. and Takagi, H., 2014, Paleostress analyses by means of mixed Bingham distributions of healed microcracks in the Ryoke granites, Central Japan. *Jour. Geol. Soc. Japan*, **120**, 23–35.*

Kanai, T., Moriyama, K., Mukoyoshi, H. and Takagi, H., 2015, Preparation condition of rock thin section for electron backscatter diffraction analysis: Examples of quartz and calcite. *Jour. Geol. Soc. Japan*, **121**, 421–427.*

Kanai, T. and Takagi, H., 2016, Determination of the stress conditions of the ductile-to-brittle regime along the Asuke Shear Zone, SW Japan. *Jour. Stuct. Geol.*, **85**, 154–167.

Kanai, T. and Takagi, H., 2017, Paleostress directions estimated from healed microcracks in the Cretaceous granitoids: their variation along a transect normal to the Median Tectonic Line, central Japan. *Jour. Geol. Soc. Japan*, in press.*

Watanuki, S. Kanai, T., Saka, H. and Takagi, H., 2017, Deformation microstructures developed in the Iragawa mylonite zone in the western part of the Shirakami Mountains, Northeast Japan. *Jour. Geol. Soc. Japan*, in press.*

*in Japanese with English abstract

Presentations

Kanai, T., Aizawa, S. and Hideo, T., 2012, Paleostress analysis using healed microcracks in the Ryoke granites, southern Chubu District. *Japan Geoscience Union Meeting 2012*, SCG68-P07.

Kanai, T., Takagi, H. and Yamaji, A., 2013, Paleostress analysis of healed microcracks in the Ryoke granites by means of mixed Bingham distributions. *The 120th Ann. Meet. Geol. Soc. Japan*, R15-P-12.

Takagi, H., Sato, T., Harada, N., Kanai, T. and Hoshi, H., 2013, Reconstruction of paleostressfield estimated from microcracks of quartz in Tanzawa Tonalite and Fujikawa plutonic rocks. *Proceedings of the geological research summit organized by the Kanto Branch, Geological Society of Japan ! Izu Collision Zone*, 50–51.

Takada, A., Kanai, T. and Takagi, H., 2014, Paleostress analyses using the orientation distribution of veins and calcite twins. *The 121th Ann. Meet. Geol. Soc. Japan*, R15-P-3.

Kanai, T. and Takagi, H., 2014, Paleostress analysis using calcite twin in amygdales of the pseudotachylyte of the Asuke Shear Zone. *The 121th Ann. Meet. Geol. Soc. Japan*,

R15-P-4.

Kanai, T., Mukoyoshi, H. and Takagi, H., 2015, Sample preparation condition for SEM-EBSD: An example of quartz minerals in granite. *Japan Geoscience Union Meeting 2015*, SSS29-P04.

Kanai, T. and Takagi, H., 2015, Estimation of deformation environment of Asuke Shear Zone using pseudotachylyte and mylonite. *Japan Geoscience Union Meeting 2015*, SCG57-24.

Ikeya, M., Kanai, T. and Takagi, H., 2015, Estimation of size and distribution of quartz particles in brittle fault rocks using image analyses. *The 122th Ann. Meet. Geol. Soc. Japan*, R12-P-19.

Tano, K., and Kanai, T. and Takagi, H., 2015, Cathodoluminescence spectra properties of quartz in fault roks. *The 122th Ann. Meet. Geol. Soc. Japan*, R12-P-3.

Watanuki, S., Saka, H., Kanai, T. and Takagi, H., 2016, Deformation environment of the mylonite zone to the west of Shirakami Mountains, Northeast Japan. *Japan Geoscience Union Meeting 2016*, S-MP43-P12.

Tano, K., Kanai, T., Watanuki, S. and Takagi, H., 2016, Cathodoluminescence spectra properties of recrystallized quartz in mylonites. *The 123th Ann. Meet. Geol. Soc. Japan*, R12-P-4.

Kanai, T. and Takagi, H., 2016, Paleostress analysis of healed microcracks in the Ryoke granites: the change in the perpendicular direction to the strike of the Median Tectonic Line. *The 123th Ann. Meet. Geol. Soc. Japan*, R14-O-7.